STRUCTURAL CHARACTERIZATION OF GEMINI-BASED NANOPARTICLES FOR DELIVERY OF DNA

A Thesis Submitted to the College of

Graduate Studies and Research

in Partial Fulfillment of the Requirements

for the Degree of Master of Science

in the Pharmacy Graduate Program

University of Saskatchewan

Saskatoon, Saskatchewan

Canada

Osama Alaidi

PERMISSION TO USE

In presenting this thesis in partial fulfillment of the requirements for a Postgraduate degree from the University of Saskatchewan, I agree that the Libraries of this University may make it freely available for inspection. I further agree that permission for copying of this thesis in any manner, in whole or in part, for scholarly purposes may be granted by the professor or professors who supervised my thesis work or, in their absence, by the Head of the Department or the Dean of the College in which my thesis work was done. It is also understood that any copying or publication or use of this thesis or parts thereof for financial gain shall not be allowed without my written permission. It is also understood that due recognition shall be given to me and to the University of Saskatchewan in any scholarly use which may be made of any material in my thesis. Requests for permission to copy or to make other use of material in this thesis in whole or part should be addressed to:

Chair of Pharmacy Graduate Program,
College of Pharmacy and Nutrition
University of Saskatchewan
110 Science Place
116 Thorvaldson Building
Saskatoon, SK Canada, S7N 5C9

ABSTRACT

Cationic gemini surfactants have been used for delivery of DNA into cells. These cationic surfactants are known to strongly bind to DNA to form a complex. In the dilute regimen, when the gemini-DNA complexes are mixed with helper neutral lipids, they undergo spontaneous assembly to form particles that are able to transfect DNA into the cells. In this study, the structure of several gemini surfactants, gemini-DNA complexes and gemini-DNA-neutral lipids complexes were systematically examined by small angle x-ray scattering (SAXS). The gemini surfactants were found to form micelles of varying shapes and arrangements modulated by the nature of spacer region and tail lengths. This includes ellipsoidal and worm-like micelles (as in the case of the 12-s-12 series) and disk-shaped hexagonally packed micelles (as in the case of 16-3-16). In addition to the study of the gemini surfactants, the effect of varying the DNA: gemini charge ratio on the DNA-gemini assembly was studied. The scattering pattern has shown that in the presence of excess gemini surfactants, free unbound surfactants exist in the solution.

Upon the addition of neutral lipids, DNA-gemini-neutral lipid complexes are formed. The scattering patterns of the latter showed evidence of a strong interaction of the neutral lipids with the free gemini surfactants and the overcharged DNA-gemini complexes. Effectively, overcharging DNA-gemini complexes seem to aid in its incorporation into the neutral lipid matrix. These findings shed the light on the structure of DNA-gemini-neutral lipid systems and provide insights into the factors that influence the spontaneity of the self-assembly process.

More importantly, the presented work provides a general strategy that can be applied to the study of similar systems using small angle x-ray scattering. A helium and vacuum chambers were made to enable testing the feasibility of the technique at the Canadian Light Source. Further, a pipeline was written to automate the reduction and analysis of SAXS data.

ACKNOWLEDGEMENTS

I would like to thank my supervisors, Pawel Grochulski and Ildiko Badea for making this work possible. I am grateful for the Graduate chair Ed Krol and Jian Yang for the support. I gratefully acknowledge Masoomeh Poorghorban (Department of Pharmacy and Nutrition, University of Saskatchewan) for her feedback on testing various parts the software and for her helpful suggestions and James Gorins (CMCF, Canadian Light Source) for the help with the testing the helium and vacuum chambers. I am grateful to McDonald Donkuru for the synthesis of the gemini surfactants. I would like to thanks Waleed Mohammed-Saeid and Mays Al-Dulaymi for their generous help with the DNA isolation. Indeed, I cannot forget the support of Shaun Labiuk (CMCF) and Deborah Michel in the labs.

I would like to thank Thomas Weiss, beamline scientist at the BL4-2 beamline at the Stanford Synchrotron Radiation Laboratory, as well as all members of the BL4-2 beamline for the help in data collection. The x-ray scattering experiments presented in this thesis were carried out at the Stanford Synchrotron Radiation Laboratory, a national user facility operated by Stanford University on behalf of the U.S. Department of Energy, Office of Basic Energy Sciences. The SSRL Structural Molecular Biology Program is supported by the Department of Energy, Office of Biological and Environmental Research, and by the National Institutes of Health, National Center for Research Resources, Biomedical Technology Program.

Last but not least, I would like to thank my family for their support, and in particular my farther, without whose support this work would not have come to light.

Contents

LIST OF ABBREVIATIONS

AFM	Atomic Force Microscopy
CT	Caillé Theory
DLS	Dynamic Light Scattering
DOPE	1,2-Dioleyl-*sn*-glycerophosphatidylethanolamine
DPPC	1,2-Dipalmitoyl-*sn*-glycero-3-phosphocholine
EM	Electron Microscopy
FT	Fourier Transform
GAP	Global Analysis
GFP	Green Fluorescent Protein
HCP	Hexagonal Close-Packed
HWHM	Half Width at Maximum Height
KB	Kirkpatrick-Baez
MCT	Modified Caillé Theory
MLV	Multi-Lamellar Vesicles
NNLLSQ	Non-Negative Linear Least Squares
OLV	Oligo-Lamellar Vesicles
PDDF	Pair Distance Distribution Function
PDF	Pair distance Distribution Function
PET	Polyethylene Terephthalate (Mylar®)
PT	Paracrystalline Theory
PVC	Poly-Vinyl Chloride
SANS	Small Angle Neutron Scattering
SAXS	Small Angle X-ray Scattering
TD	Temperature Disorder
TEM	Transmission Electron Microscopy
ULV	Uni-Lamellar Vesicles
WAXS	Wide Angle X-ray Scattering
XPODS	X-ray analysis software for Partially Ordered and Disordered Systems

LIST OF FIGURES

LIST OF TABLES

1 INTRODUCTION

An ultimate goal of the study of matter is to be able to use, control and manipulate its behavior for the benefit of mankind. This behavior, which can be described by its physical and chemical properties, is tightly related to the type and arrangement of atoms forming the molecules, as well as the interaction of these molecules amongst each other. That is to say: its behavior is related to its structure. Despite the great progress in structural biology in the past few decades, our understanding of the behaviour of biomolecules in their natural environment is still very limited. This is mainly due to the complex nature of biological systems. One aspect of this complexity, is that biomolecules do not work individually, but rather collectively or in a series of interactions between different types of molecules. No wonder, inter-molecular interactions and spontaneous assembly of molecules are of great interest in the study of biological systems. Methods, tools and models to tackle such challenges are still, to a great extent, in their early development. The work done in this thesis generally falls within this scope.

DNA and lipids are primary constituents of the living organisms where they play fundamental roles in numerous biological events. The first in-depth studies of the structure of both had come about in the fifties and sixties, respectively. The DNA structure was first resolved by Watson and Crick [1] after the famous x-ray photograph and the important contribution made by Rosalind Franklin [2]. The structure of lipids was pioneered by Luzzatti, who has founded many crystallographic basics of lipids and surfactants structure [3].

DNA mediated interactions play a fundamental role in biology [4]. Many processes in the cell occur as a result of DNA interaction with other molecules. Examples of such processes are winding and unwinding of DNA, DNA condensation in chromosomes, circular DNA condensation in bacteria, activation and block of certain genes as a method of regulation of expression, etc. Many of these interactions are a part of the central dogma [5]. The fact that DNA is a charged molecule makes DNA interactions a frequent process.

Lipids on the other hand are abundant in the living organisms, and included in many organelles in the cell. The most notable location is in the cell membrane where they play a crucial role in numerous vital functions [4]. The flexibility, dynamical and self-assembling nature of lipids, makes them the main molecule of choice to perform functions that requires major structural changes and rearrangements or requires formation and breakdown of cellular compartments. Examples of such processes are endocytosis, fusion and transport across barriers. This dynamic and self-assembling nature of lipids, as well as the natural abundance in cells (and hence the low toxicity), had also made them (or their derivatives) molecules of choice for many attempts to use as artificial drug delivery agents. Moreover, the ability to design cationic lipids that spontaneously condensate with DNA had made them an attractive choice for the purpose of gene therapy (for example, reviewed in [6,7]).

The nature of DNA-protein interactions has been studied in many complexes. This was aided by the possibility of crystallizing the proteins, DNA or the complex, and thus enabling the detailed structural study of the bases of the interaction by x-ray diffraction. The fact that higher resolution structures were obtained for various DNA-protein complexes have made it possible to study and understand the details governing such interactions on the atomic level [8,9]. DNA-lipids interaction is rather a much less understood phenomenon. This can be attributed to various reasons. One possible reason is the lack of direct method to obtain detailed structural information about the nature of the complexes. Another possible reason is the complexity of this interaction. By complexity I mean the dynamic nature of lipids which are held together by weak forces. This leads to diverse constructs which cannot be described by a single model. This diversity could be seen in the form of polydispersity is the sizes of the particles/ domains, high thermal fluctuations in positions of atoms and inhomogeneity of the resulting condensate. In many cases, the degree of diversity and stability depends on the input ratios of the components [10]. An expected consequence is local or short term disorder in the formed lattices (high thermal vibrations) as well as long range disorder in the lattice (stacking faults and undulations).

From x-ray diffraction prospective, this disorder leads to a much broader intensity peaks, eventually leading to the decline of the higher order diffraction peaks. This intensity decline is accompanied by increase of the diffuse scattering in the background. Therefore, the diffraction pattern exhibits extensive information loss, but on the other hand, the diffuse scattering in the background encodes information about the disorder of the system. In fact, it is less accurate or even one may call incorrect, to attempt to assign three dimensional coordinates for atomic positions for lipid molecules from a diffraction pattern. It is rather more precise to consider a distribution function describing a range of possible positions or perhaps to consider an ensemble of structures [11]. An additional complexity however, is that the fact that DNA is charged makes counter ions play an important role in the neutralization process. Upon the binding of DNA to another molecule, these counter ions will be replaced by the new molecules and they will be released to the solution giving rise to higher diffuse scattering background.

For decades, the success of structure determination by x-ray mainly depended on highly ordered crystalline specimens. Even though, and rather very early, André Guinier showed that simple structural information, such as the radius of gyration can be obtained from a completely disordered specimen. Since then two separate communities have developed for structure determination by x-ray. The first, uses x-ray patterns from highly ordered samples such as single crystals or polycrystalline samples (powder diffraction), while the second, uses x-ray scattering patterns from completely disordered samples to get global structural parameters by using information encoded in the small angle regimen. The former methods (crystal diffraction), are generally much more developed, and much more detailed in the information they provide compared to the latter. Crystallographic methods, depend on assuming that the diffracted crystals are almost perfect in terms of local order, though there is a degree of imperfection (mosaicity) when considering the crystal in total. These techniques usually attempt to find methods to perfect the data within that context, and eliminate parts of the data that shows otherwise. Thus, the structural information obtained here depends on the intermolecular correlation in the lattice. The second method (mainly solution scattering), depends on the complete opposite assumption, i.e. the molecules are completely disordered and that there is no intermolecular interactions can be probed. Further, any probed interactions are considered to be a hindrance in data interpretation. Usually, there is an attempt to perfect the data within that context and to eliminate any effect of intermolecular interaction probed. In both strategies, there was always a need for isolating the target molecules and introducing an artificial environment. In general, the obstacles described above, seem to have hindered the examination and the determination of biological complexes in their natural environment by x-ray. Indeed, we are still far away from examining the scattering patterns from complicated structures such as full organelles.

More recently, partial order has been addressed. In literature, and as far as I know, there seem to be four main directions that have been shown to be useful in tackling such problem. The first is nano-crystallography [12,13]. This involves diffraction of a series of nano or micro sized single crystals. The second direction involves using disorder models. This approach takes advantage of all observations by introducing disorder parameters and/or by calculating the structure factor from analytical models. This allows the use of both Bragg's peaks as well as diffuse scattering simultaneously [14–20]. The third direction is x-ray imaging. This includes both microscopy (for example Scanning Transmission X-ray Microscopy (STXM) and Transmission X-ray Microscopy (TXM) [21,22]) and diffraction based imaging (such as Coherent Diffractive Imaging (CDI) or also known as Coherent X-ray Imaging (CXI)) [23–25], correlated scattering [26], ptychography [27,28] and x-ray holographic methods [29]). The fourth direction or group of methods generally depends on the pair distance distribution function. These methods are generally considered as refinement methods that relay on making changes in a real space model until a PDF function similar to the one obtained from the scattering data is achieved. Examples of implementations of such methods are: Reverse Monte Carlo [30,31], PDFgui [32] and studying diffuse scattering from single crystals methods by 3D Patterson maps [33].

Most of the above methods are still developing and there are still many obstacles that remain unresolved. They can be generally classified into two distinct groups. One of which deals with the system as ordered and models the disorder. The second considers the system as completely disordered and accounts for the partial order. The issue is however, is still a subject of research and a complete theoretical framework or established methodology for all partially disorder systems do not yet exist.

Indeed, if one would roughly classify matter based on its diffraction pattern into ordered (crystals) and disordered (dilute solutions) and partially ordered systems, then partial order of matter is the dominant form of bio-molecules in the cell or in biological organisms. This re-emphasises the importance and the need to develop new methods for structural determination of partially ordered/disordered specimen. I hope that the work done in this study contributes to that long term goal.

The following chapters of this thesis can be divided into three main parts. The first part (chapter 2) provides a general overview about the structure of lipids and lipid-DNA complexes.

The second part (chapters 3 and 4) focuses on the tools used or needed for small/wide angle scattering (SAXS/WAXS) data collection and interpretation. Chapter 3 describes the SAXS/WAXS instrument, and demonstrates an initial attempt to make the instrument available at the CMCF beamline at the Canadian Light Source (CLS). The subsequent chapter (chapter 4) in this part demonstrates attempt to automate the data analysis. The third part is an application of x-ray scattering and diffraction on a drug delivery system that involves DNA-lipid complexes. This includes the solution structure of the pure gemini surfactants, their DNA complexes (chapter 5) and the full gemini-based formulations for DNA delivery (chapter 6).

2 THE STRUCTURE OF THE LIPIDS AND DNA-LIPID SYSTEMS

Lipids are a class of organic compounds that are (or contain) fatty acids or their derivatives. This includes fats, oils, sterols and waxes. They are characterized by the presence of a hydrophilic and a hydrophobic portion. The hydrophobic portion is mostly a hydrocarbon chain which is flexible and will yield a degree of order depending on the temperature and chemical environment. The first step in understanding lipid structures is usually by experiments in which the lipids phase (i.e. the supra-molecular organization and ordering of lipid molecules) is determined [34].

2.1 Diffraction from mesophases

X-ray small/wide angle scattering is a widely used structural technique in nanomaterials. The scattering profile at the small angle provides information about the overall structure of the particles scattered in solution, whereas the finer structural details can be obtained as the angle of diffraction increases. If the particles are arranged in a repeating manner, the scattered waves will add up to appear as spots or rings on the detector. From the distances and intensities of these spots or rings the structural arrangement of the molecules of interest can be identified. SAXS/ WAXS have been widely used in identifying of lipid phases in many studies [35]. The target of the following section is to provide a short introduction to x-ray scattering and diffraction of biomembranes. Much of what is presented in this section can be found in many standard textbooks of crystallography and small angle scattering (for example references [36–41]). Unless mentioned otherwise, the presented material is taken from reference [36].

2.1.1 X-ray scattering

X-rays are electromagnetic waves with an electric field component characterized by sinusoidal oscillations as a function of time, in a direction that is perpendicular to the direction of the propagation of the primary wave. According to the theory of electromagnetic waves, the electric field exerts a force on charged particles, such as electrons in atom, hence forces them to accelerate. This energy is then either absorbed, leading eventually to the ejection of the electron from the atom, or radiated in the form of waves that are either equal in energy and frequency of the incident waves (elastic or Thompson scattering) or lower in energy and frequency than the incident waves (inelastic or Compton scattering). These radiated waves are called scattered x-rays, and are monitored by recording a quantity called intensity. The latter quantity can be defined as the energy per unit area per unit time. For monochromatic x-rays, the intensity is proportional to the square of the maximum amplitude of the wave.

Light (or electromagnetic waves), including those of short wavelength as x-rays, have two properties that complement each other, and both are useful in different applications. The first is that they can be thought of as photons. An electromagnetic wave has an energy of $E = \mathrm{h\nu} = \mathrm{hc}/\lambda$ where, c is the speed of light and h is Planck's constant, ν is the frequency and λ is the wavelength. X-rays have a high penetrating power, and travel with a speed that is almost equivalent to the speed of light in vacuum, in any medium they are in. Thus, effectively not affected by refraction and have a refractive index that is slightly smaller than unity. Even in dense medium, this the deviation from unity is in minute, and in the majority of cases is in the order of 10^{-5}.

The scattering process however, is usually, and more conveniently, explained by the other property of light which is the wave property. X-rays propagate in straight lines, and since they have a strong penetrative power, they are not focused with usual lenses. The basic theory behind various techniques of scattering is essentially the same. It is primarily based on the interpretation of the scattered waves from individual atoms and the interference from those scattered waves.

2.1.2 Scattering form a free electron

The scattering from a free electron is known as classical scattering theory. When an x-ray photon strikes an electron, the electric field of this wave induces a dipole oscillation of this electron, leading to the creation of a secondary wavelet having the same the same energy as the primary wave. Thus, every electron in the scattered volume becomes a source of a spherical scattered wave, having the same intensity and energy. The intensity emitted from a point source (or almost a point source) is the amount of energy per second per unit solid angle in a certain direction. Such concept is by which scattering is defined. Thus, the amount of photons emitted per second per unit solid angle as a function of the scattering angle is known as the scattering pattern of from an object.

The intensity of the scattered wave is described by the Thomson formula:

$$I_e\,(\theta) = I_0 \frac{e^4}{m^2c^4a^2}\left(\frac{1 + cos^2(2\theta)}{2}\right)$$

Considering that $r_e = e^2/mc^2$, then

$$I_e(\theta) = I_0 r_e^2 \frac{1}{a^2}\left(\frac{1+cos^2(2\theta)}{2}\right)\ (2.1)$$

Where,

I_e	is the intensity of the scattered wave from an electron,
2θ	is the angle between the primary and the scattered beam (the diffraction angle),
I_0	is the primary beam intensity,
e	is the charge of an electron,
m	is the mass of an electron,
a	is the distance between the electron and the point at which the intensity is measured,
r_e	is a quantity with unit of length known as the classical electron radius.

The numerical value of $e^4/m^2c^4 = 7.94 \times 10^{-26}$cm^2 and ($e^2/mc^2 = 7.90 \times 10^{-26}$ cm^2).

The last term in the equation (in brackets) is the polarization factor and is practically equal to 1 in the small angle regimen. We generally measure and deal with the relative intensity i.e. factors of I_e . In the cases were the molecular weight is of interest one could put the scattering pattern on absolute scale. The formula that describes the total scattering (both coherent/Thomson scattering and Compton scattering) can be written as:

$$I_e(\theta) = I_{coherent}(\theta) + I_{Compton}(\theta)$$

2.1.3 Reciprocal space

If an incident wave, described by a vector $\boldsymbol{s_0}$ with its a length equal to $1/\boldsymbol{\lambda}$ (Figure 2.1) goes through a scattering centre at the origin $\boldsymbol{O}$, and the scattered wave vector $\boldsymbol{s_1}$ corresponds to a scattering angle $\mathbf{2\theta}$, then the scattering vector $\boldsymbol{s}$ is defined as:

$$s = \frac{s_1 - s_0}{\lambda}$$

The modulus of the scattering vector can then be given by $s = \frac{2\sin\theta}{\lambda}$

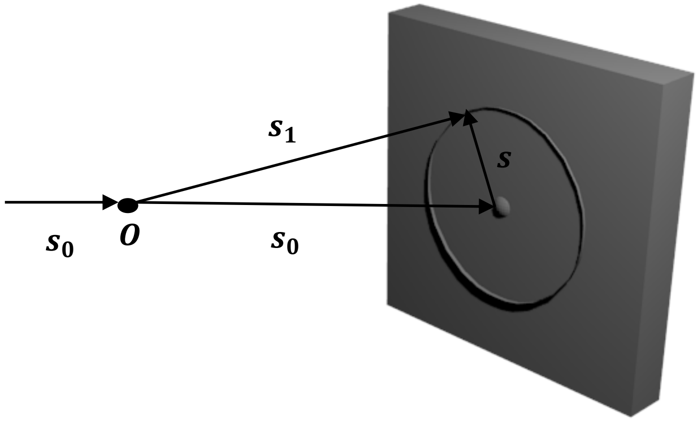

Figure 2.1. A schematic illustration of the scattering.

By convention, and for mathematical convenience, the momentum transfer q is more commonly used in small angle scattering, and is defined as:

$$q = 2\pi s = \frac{4\pi \sin\theta}{\lambda} \tag{2.2}$$

The phase differences which will influence the nature of interference are related to the distances d between the two scattering sources d by Bragg's law:

$$n\lambda = 2d\,sin(\theta) \tag{2.3}$$

Where,

d is the distance between the planes,
λ is the wavelength of the incident wave,
θ is half of the diffraction angle.

The scattered waves from all electrons will be emitted simultaneously leading to the interference of these waves. These scattered waves, ignoring Compton scattering, are similar in energy but vary in their phases.

2.1.4 Scattering from bilayers and partially ordered systems

The continuum description as an electron density model is more suited for describing the structure of bilayers than that of the discrete description (such as atomic positions). One of the most common phases is the lamellar system. In multilamellar vesicles (MLV), which is a one dimensional repeat of 2D fluidic stacks (representing the lipid bilayers), the position of the first peak in the unit cell lattice parameter which refers to the distance from the head of one bilayer to the head of the subsequent bilayer. The observed powder diffraction pattern intensity is given by:

$$I(q) = N\,|F(q)|^2\,\frac{S(q)}{q^2} \tag{2.4}$$

Where, $q = \frac{4\pi\, sin(\theta)}{\lambda} = \frac{2\pi}{d}$, the $1/q^2$ term is the Lorentz correction for wide angle scattering, $F(q)$ is the form factor (which is the Fourier transform of the electron density of a single bilayer), $S(q)$ is the structure factor (the Fourier transform of the lattice function) and N is related to concentration. An illustration of the elements of the equation above (equation (2.4)) can be found in Figure 2.2. The ratios between the positions of the Bragg's peaks in reciprocal space can be used in the determination of the space group. For example, as shown in the figure, in lamellar system the positions of the peaks q_{001}: q_{002}: q_{003} .. etc., would be equal to $\frac{2\pi}{d} : \frac{2\pi}{2d} : \frac{2\pi}{3d} :$ ... (i.e. equal to $1: 2: 3 \ldots etc.$), where d is the lattice parameter (calculated from mid of one bilayer to the mid of the consequent one).

However, in lamellar lipid systems usually there is a degree of disorder added by the presence of unilamellar vesicles (ULV) dispersed in the solution, especially for weakly bound membranes. The diffraction from ULV gives rise to purely diffuse scattering thus leading to the rise of diffuse scattering in the background. To account for these uncorrelated unilamellar vesicles an extra diffuse scattering term may be added to the previous equation, thus equation (2.4) it becomes:

$$I(q) = N_{correlated}|F(q)|^2\,\frac{S(q)}{q^2} + N_{uncorrelated}\frac{|F(q)|^2}{q^2} \tag{2.5}$$

Where, $N_{\text{uncorrelated}}$ is a scaling factor for the diffuse scattering from uncorrelated unilamellar vesicles. The equation above however, does not account for the inter-particle interaction nor the overall particle form or size of those unilamellar vesicles. Such scattering intensity is dominant at a much smaller angle than that where the Bragg's peaks due to the stacking of the bilayers will appear [42].

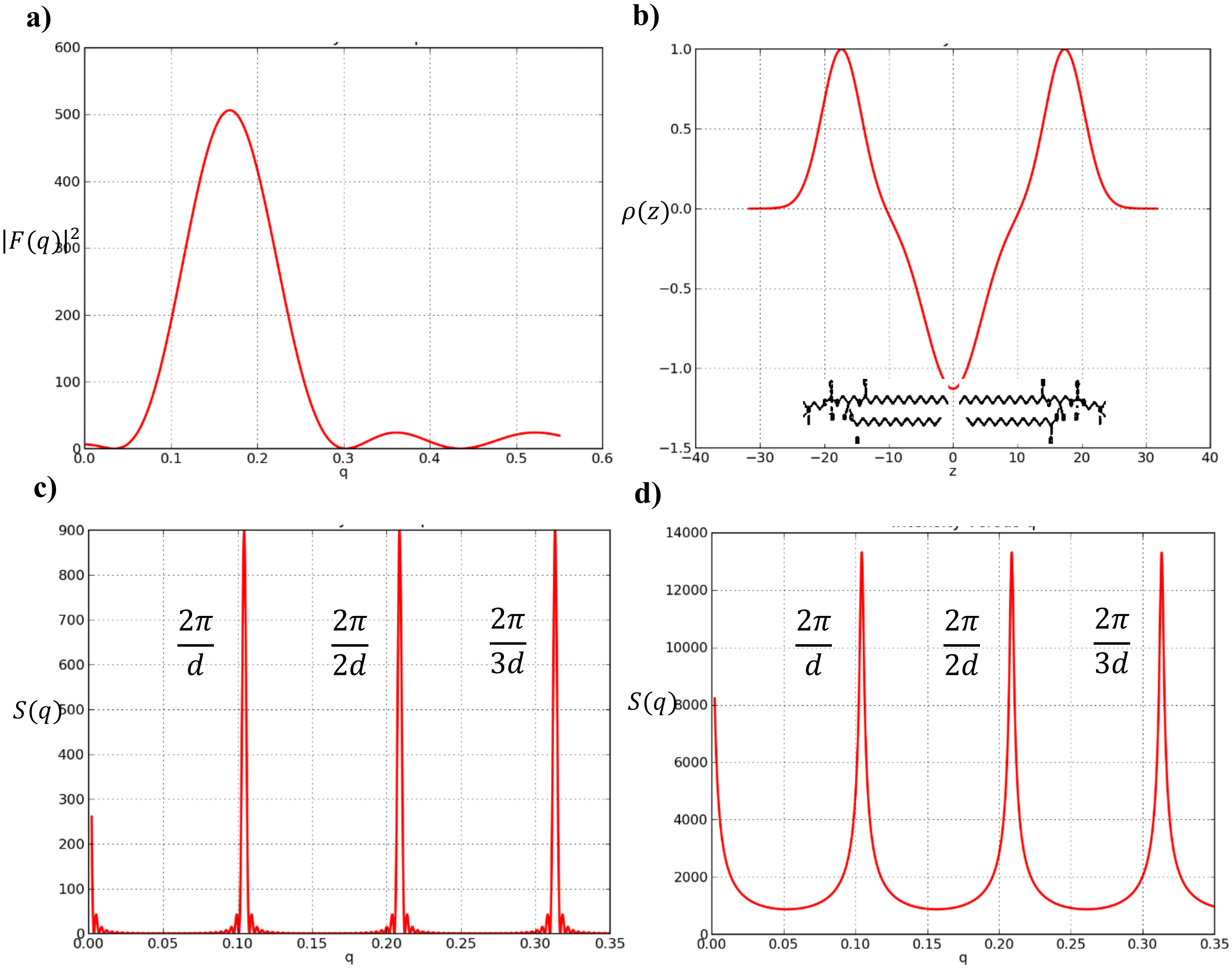

Figure 2.2. Elements of the scattering equation of bilayers.

The figure shows an illustrated example of the elements of equation (2.4)*. a) Shows the amplitude squared* $|F(q)|^2$*, b) Shows an electron density profile which is the Fourier transform of the form factor, c) Shows the calculated structure factor* $S(q)$ *of a perfectly crystalline lamellar phase (1D lattice) but with limited number of bilayers and d) Shows the same structure factor in panel* ***c*** *but corrected for the variation of the sizes of the domains using an* *exponential function. As shown in the diagram the correction for the domain size polydispersity (panel* ***d****) leads to the disappearance of the ripples that appears in the originally calculated structure factor (panel* ***c****). These ripples appear due the Fourier series truncation error which rises due to the limited size of the domains (i.e. limited number of bilayers). The correction leads to the smoothening of the curve (which what is usually observed experimentally). These diagrams are presented here for the purpose of conceptual illustration only. Further details on the methodology of calculating these quantities can be found in reviews on the topic (for example ref* [43,44]*).*

2.1.5 Scattering from multiple phases, multiple crystals and mixtures

The scattering intensity from a mixture of uncorrelated (non-interacting) molecules or a mixture of uncorrelated (non-interacting) multiple domains/crystals, which may or may not be embedded in one another can be approximated as the sum of the scattering patterns of these molecules/domains weighted by their partial contributions to the total scattering i.e. a linear combination of the different phases. Thus, the measured total scattering for *N* phases can be given by:

$$I = I_{bk} + v_1 I_1 + v_2 I_2 + v_3 I_3 + \cdots + v_n I_n = I_{bk} + \sum_{i}^{N} v_i I_i \tag{2.6}$$

Where, I_{bk} is the total background, v_i is the weighting coefficient of the i^{th} phase and I_i is the scattering intensity of the i^{th} phase.

2.2 Structural organization of lipids

The organization of lipids can be classified into two main types; short-range organization and long-range organization. The shape of the lipid molecules plays an important role in the formation of these supra-molecular organization.

2.2.1 Short-range organization

This refers to the conformation taken by the hydrocarbon chains. The main types seen in lamellar systems are: the fluid or liquid phase (Lα), the gel phase (Lβ\`), the ripple (Pβ\`) and the crystalline (subgel) phase (Figure 2.3). The conformation of the hydrocarbon as well as the shape of the individual lipid molecules will together determine the distances between the heads of the molecules within a single bilayer and thus this will influence the volume occupied by individual lipid molecules. Such phases can be determined by the Bragg's peak intensity at a d-spacing of 4-5 Å (indicated by red arrows in Figure 2.3). This distance is related to the head to head distance of lipids in the plane (i.e. x and y direction) of the bilayer [34,45].

The phase (or also called *subcell*) taken by lipids has an important effect on the membrane elasticity and curvature. These two properties (elasticity and curvature) play an important role in the interaction of the lipid molecules with heterogeneous molecules such as membrane proteins, peptides and small molecules. The transition between phases is usually temperature dependant. However, there are also many other factors that can influence such transition including salt concentration and the presence of multiple types of lipids within the bilayer [46–48]. The gel, ripple and fluid phase are the most commonly described in biologically related applications. It is thought that the fluid phase is the most biologically relevant as it is usually found at temperatures that are similar to body temperature [43,44]. The molecules in the fluid phase are obviously less organized and characterized by the absence of the Bragg's intensity peak at a d-spacing of 4-5 Å, and thus there is no evidence seen for the existence of subcells, as the heads are not organized. Whereas, the gel phase can show hydrogen bonds between the lipid heads and its scattering patter is characterized by the presence of a sharp intensity peak at a d-spacing equal to 4-5 Å [49].

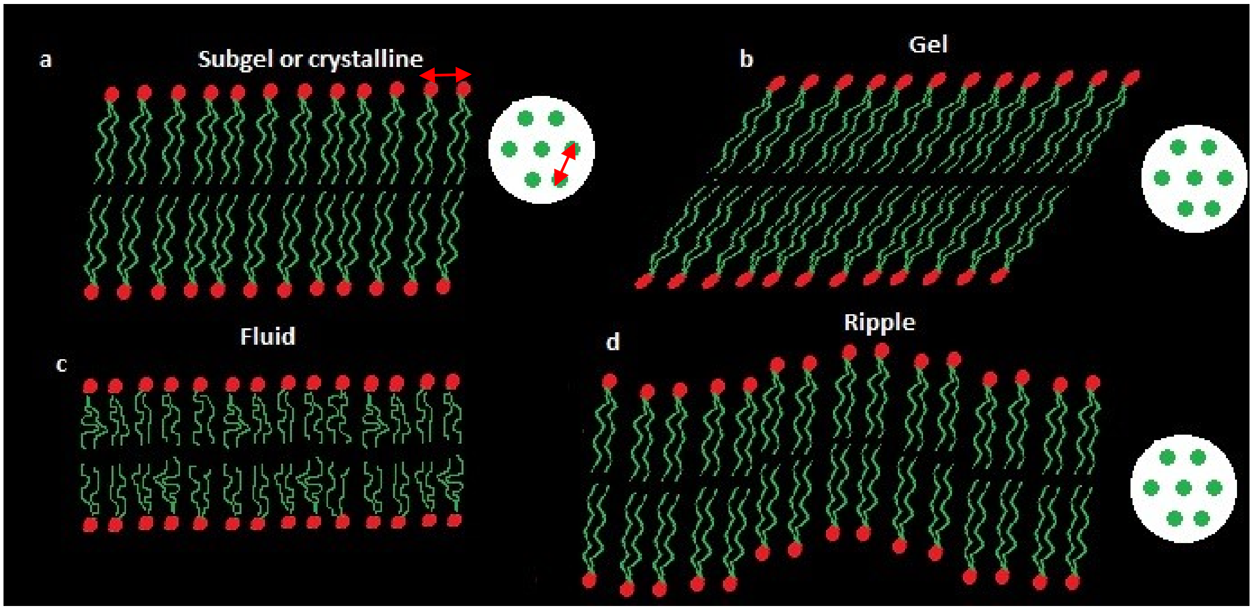

Figure 2.3. Phases that can be characterized by wide angle scattering.

The figure shows the different phases along the normal of the bilayer formed as a result of short range organization. Such phases can be determined by x-ray diffraction form the position and intensity of the peak in the WAXS range at 4-5 Å (red arrows). The cross sections of hydrocarbon chains (if applicable) are shown on the right of each phase in the white circles. In the fluid phase (c) the chains oriented with no fixed organization.

2.2.2 Long-range organization: Lamellar and Non-lamellar lipid systems

Lipid bilayers will usually organize further into an upper level organization (also referred to as lipids phases) in which bilayers will stack on each in one, two or three dimensional unit cells and thus can be described as liquid crystals (Figure 2.4). The nature of this organization is mainly thought to be related to the shape and nature of chemical groups of the individual lipid molecules [45,49]. Lipid phases can be classified into two broad categories. These are Type I phases and Type II phases (inverted phases), also known as “oil in water” and “water in oil” phases respectively [49]. Further, lipid aggregation/organization can either be in the form of simple discrete particles such as micelles and unilamellar vesicles or can be in the form of a continuous crystalline lattice.

Lipid diffraction (or SAXS/WAXS) gives rise to a scattering pattern that is characterized by the presence of Debye rings (powder pattern). This indicates that lipid microcrystals are oriented in all directions within the sample just as normal solid powder. However, the interpretation of these patterns is fundamentally different due to the nature of lipids. In the literature, the analysis of reflections/rings corresponding to the long-range order is referred to SAXS whereas the reflections/rings corresponding to the short-range order is termed as WAXS. The long-range order usually gives rise to 3-4 reflections/rings (in fully hydrated specimen). In many cases, the corresponding d-spacing of those rings lays within the range of 20-90 Å. Whereas, the short-range order usually gives rise to one reflection/ring that corresponds to a d-spacing of 4-5 Å [43,44]. It is important to note that the reason for the absence of higher order peaks is due to the various types of disorders. These can be classified as follows:

i. Disorders of the first type: are thermal disorders (TD).

ii. Disorders of the second type: can be understood as fluidic undulations in the Lα fluidic phase or stochastic stacking defects in more rigid phases. In lipid systems, these form of disorder are modeled to be able to extract disorder parameters from diffraction data using two commonly used disorder theories: the Paracrystalline Theory (PT) [15,36] and the Modified Caillé Theory (MCT) [14,50]. The MCT is well known to be more suited for the Lα phase [51].

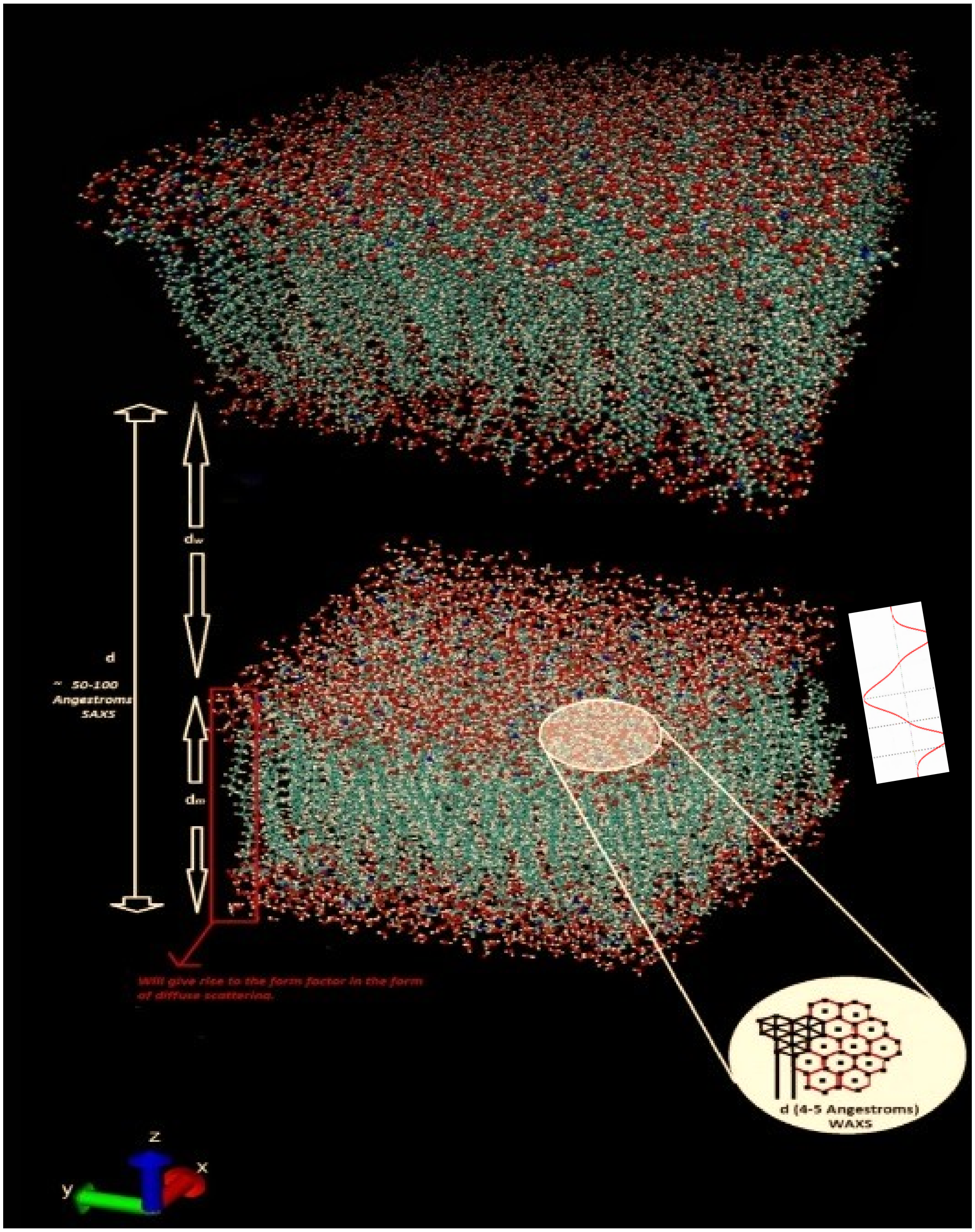

Figure 2.4. A schematic diagram showing the overall structure of lipid bilayers.

In multilamellar vesicles the distance d in the SAXS range is the lattice parameter, which can be determined by the position of the first peak. The distance d in the WAXS range (in the white circle) is the distance between heads which is becomes almost the same between all lipid heads in the gel phase giving rise to another peak at ~ 4-5 Å. In the fluid phase this peak almost vanishes due to the thermal fluctuations of the molecules. The distance dm can be calculated from the diffuse scattering by fitting it to a suitable model. The remaining parameter dw is simply dw= d- dm. A schematic electron density profile plot of the lower bilayer is shown on the right (see Figure 2.2 for further details).

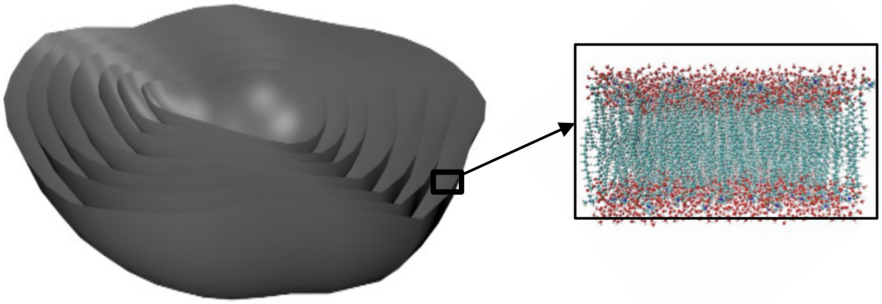

Figure 2.5. The structure of MLV.

MLV can be approximately 1-10 microns in size in which lipid bilayers (usually between 10-200 bilayers) are stacked in an onion-like structure [43].

The most common and perhaps most extensively studied lipid phase is the fully hydrated lamellar system. It is a one dimensional system, in which bilayers stack on top of each other forming spherical lamellae (onion-like structure) and its cross-section would show 200 or more concentric rings of bilayers separated by spaces that are occupied by water (Figure 2.5). These are referred to as multilamellar vesicles (MLV).

Many non-lamellar lipid (and surfactants) liquid crystalline phases have been reported. This includes bicontinous cubic [52,53], inverted hexagonal [54,55], rhombohedral [56], tetragonal [57,58], discotic [59,60], hexagonal close packed micellar [61] and others. Hyde S. have reviewed and tabulated the majority of lyotropic liquid crystalline mesophases that had been reported [49]. The phases can is identified by the ratios of the positions of the observed Bragg's peaks in reciprocal space.

2.2.3 The effect of the shape of the molecules on lipid phases

To rationalize the effect of the shape of the individual lipid molecules, the ratio of the size of hydrophobic tail to the size of the hydrophilic head is usually used. The resulting ratio is known as the shape parameter or also the critical packing parameter [62]. The packing parameter S is given by

$$S = \frac{v}{a_0 l_c} \qquad (2.7)$$

Where, v is the hydrophobic chin volume, a_0 is the head group area and l_c is the critical/effective hydrophobic chain length.

The general rule is that the value of S or the shape/packing parameter is an indicator of the phase as follows:

$S < 1/3$ normal micelles are formed (type 1 micelles), $1/2 > S > 1/3$ cylindrical micelles are formed. $1 > S > ½$ lamellar phases (Lα) are formed, and $S > 1$ inverted phases are formed (type 2 micelles). Although possible, it is usally difficult to accurately estimate the parameters that determine S. Further, in addition to the shape parameter the concentration of the lipids also have an important influnece on the formed phases [63].

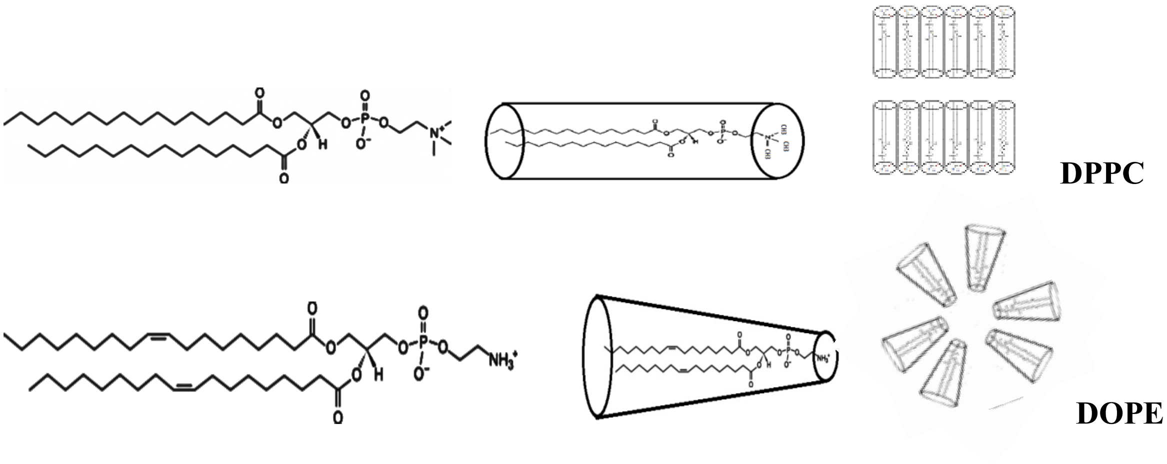

Figure 2.6. The chemical and topological structure of two standard lipids.

*Lipid molecules shapes can be classified into cone, inverted cone or cylindrical shapes. Those rough shapes are key factors in the understanding of the reasons behind the phases taken by certain lipids. Here, the lamellar phase of 1,2-Dipalmitoyl-*sn*-glycero-3-phosphocholine (DPPC) can be explained by the cylindrical shape of the DPPC molecule whereas inverted cone or wedged shape (small head) of the 1,2-Dioleyl-*sn*-glycerophosphatidylethanolamine (DOPE) molecules is the main factor that leads to the formation of the inverted hexagonal phase.*

Thus, the shape of the molecule greatly influences the nature of the observed phases (Figure 2.6). One way of looking at this is to realize the effect of the shape of the molecule on the curvature of the membrane. Cone shaped molecules (with the head being the head of the cone) exhibits negative curvature leading to inverted phases, whereas the opposite shaped cones (the head being the wide side of the cone) exhibits a positive curvature leading to type I phases.

Cylindrical shaped molecules usually lead to membranes with zero curvature (i.e. flat membranes) [49]. One intuitive example in literature is varying the ratio of the two lipids 2,3-Dioleyl-oxypropyl-trimethylammonium (DOTAP) and 1,2-Dioleyl-*sn*-glycerophosphatidylethanolamine (DOPE) leads to a change of the observed phases from lamellar to hexagonal. The first lipid takes a cylindrical shape (thus tend to form lamellar phase) while the second is inverted cone-like (so tends to form inverted phases, mainly hexagonal). As the DOPE is increased a transition from the lamellar phase to the inverted hexagonal phase is seen [64].

2.3 The structure of DNA and DNA-lipid Phases

The structure of the DNA can usually be described by general parameters from which models for the helix can be built [65]. Several forms of DNA are well characterized and can be easily distinguished form x-ray data [66]. The form which DNA takes depends on the environment which the DNA is in. Other aspects such as those related to the length, concentration and GC content of the DNA molecule may influence the DNA molecule supercoiling and aggregation behaviour [67].

In the context of DNA-lipid interactions the distances between the lipids or surfactants heads will definitely be influenced by the structure of the DNA which influences the positions of the negatively charged phosphate groups. This is generally plausible in cases of lipids with a single charge on. In the case of lipids or surfactants with more than one charge on such as gemini surfactants, the distance between the two (or more) positive charges should match with the distance between the phosphate groups on the DNA, which is self is influenced by other structural parameters and manifest its self in the overall structural form of the DNA.

B-DNA is the most common form of DNA and the most physiologically relevant. Originally solved from diffraction data of DNA fibers in 92% relative humidity [68,69]. DNA is known to take this form in fully hydrated low salt conditions. One of the most important features of this form is the formation of the major and minor grooves. These grooves provide a large surface area for other biological molecules (such as proteins or drug molecules) to interact with the DNA molecule. In many cases, molecules interact with DNA specifically through one of the two grooves. The B-DNA is a right handed helix, with 10 residues per turn. It has an axial rise of 3.4

Å and helix pitch of 34º. The helix diameter is 20 Å [5]. The B-DNA is considered to be the most common and most stable DNA form in solution and thus thought to be the usually existing form in fully hydrated lipid-DNA phases [70].

Cationic lipids were first shown to be able to deliver DNA into mammalian cell by Felgner et al [71]. Such findings had greatly motivated the development of drug delivery systems using cationic lipids. The native states of both DNA and cationic lipids are neutralized by having counter ions loosely bound near the surface of these polyelectrolyte molecules. Upon mixing the two molecules with opposite charges (DNA and cationic lipids), they will self-assemble to neutralize their charges and the counter ions will be released into the solution and thus leading to a large entropic gain.

The structure of self-assembled complex will primarily depend on many factors including the nature of the lipids, the length of the DNA, the membrane charge density and the lipid: DNA charge ratio. Many phases have been characterized by x-ray diffraction. This includes the lamellar (Lc) phase [70], the inverted hexagonal phase [64] and the honeycomb-like hexagonal phase [72]. Moreover, cationic lipids siRNA complexes that were previously determined included lamellar, hexagonal and gyroid phases [73,74].

The lipids: DNA charge ratio is one of the parameters that determine the stability of the complex. When the cationic lipid: DNA charge ratio is equal to 1, all lipid and DNA are thought to be incorporated into the complex. Whereas, when the charge ratio is >> 1, then excess free lipid will be in solution leading to the co-existence of multiple phases. Similarly, when the charge ratio is << 1, free DNA will exist in solution. Upon small deviations from neutrality, the complex can still hold some extra charge showing no excess free lipids or DNA, this is termed as overcharging [75]. The membrane charge density and the lipid: DNA charge ratio are quantities that has been shown to influences DNA transfection [76,77]. In this work, the effect of varying the DNA: gemini surfactants charge ratios is investigated.

3 THE SMALL AND WIDE ANGLE SCATTERING INSTRUMENT

3.1 Introduction

In the previous chapter, the self-assembling nature of lipids was discussed. As mentioned previously, one of the techniques used to characterize the supramolecular structure of lipids is small angle x-ray scattering (SAXS).

The main target of the SAXS instrument is to eliminate parasitic scattering which may rise from any source other than the sample. Parasitic scattering can for example rise from different components of the beamline or from the air path between the sample and the detector [40].

3.1.1 Basic components of a diffraction setup

Generally speaking, diffraction beamlines that uses monochromatic x-rays usually share a common philosophy in their design. The main beamline optics are needed to collimate and shape the beam, produce a monochromatic beam and reject higher harmonics. Thus, the following general setup scheme is not uncommon. The primary white beam coming from the storage ring or insertion device is shaped using collimating slits, before it goes through a monochromator. Usually, there is a need for an optical element to reject higher harmonics and to focus the beam such as a focusing mirror. A final guard collimating element (e.g. slit or pinhole) is placed just before the sample. The scattered x-rays are collected on a detector. In SAXS/WAXS and soft x-ray beamlines, the beamlines are designed so that x-rays are always kept in vacuum. Thus, there is usually a vacuum path between the sample and the detector. In single crystal diffraction, the detector is a 2D detector, while in the case of radially isotropic scattering patterns (e.g. SAXS or powder) both 1D and 2D detectors can be used.

3.1.2 Collimation systems

In theory, beam collimation should be considered before and after every optical device the beam goes through. Practically, this is not always possible due to a variety of reasons including high cost, loss of flux and limited physical space. In general, there is several common collimation schemes on SAXS beamline. The most common of which is using a three (or more) slit system.

The first set of slits (the beam defining slits) is used to shape the white beam before it enters the beamline optics. The second set of slits (the scatter slits) is after the beam had gone through the monochromator and the focusing mirror (can be more than one slit, one after each optical element). The third set of slits (the guard slits) is placed just before the sample. The guard slits do not touch the beam, but remove the parasitic scattering around the main beam (for example that is scattered from the previous slits). This three slit system is used in many beamlines (for example 18ID beamline at APS [78]). Slit collimation however, is well known to cause distortions to the scattering pattern (smearing) that needs to be corrected for during the data analysis. An alternative scheme for collimation is the point collimation system, in which pinholes are used rather than slits. This is far more common in home sources than synchrotron. One of the main reasons for that is that pinhole collimation leads to a considerable reduction of the flux. In general, the choice of collimation systems is largely dependent on the primary beam shape. Other traditional collimating systems that are less common at synchrotrons are the Kratky block collimator and Bonse-Hart channel-cut crystals optics (reviewed in [79]).

More recently, other collimating optics has been used. For example, Kirkpatrick-Baez (KB) mirrors are used on several diffraction and SAXS beamlines at Diamond light source. Another example is using a compound refractive lens. The latter has been used on the BW4 beamline at DORIS III and more recently on the MINAXS beamline at PETRA III [80,81]. KB mirrors and compound refractive lens not only shapes the beam but also efficiently focuses the beam. For example, the setup on MINAXS beamline produces a micro or nano-focused beam that is theoretically and practically had recently had been shown to be of great advantage [82–84].

3.1.3 Sample enviroment , ion chambers, beamstop and detectors

There are many different sample environments for SAXS samples. This is due to the diverse nature of the samples of interest that can be studied by the technique. It is perhaps worth pointing out that microfluidics and automated robotics technologies are gradually becoming widely available to allow high-throughput data collection and/or from minute amount [83–88]. On most SAXS beamlines, the beam flux is usually recorded upstream and downstream of the sample to allow the correction for absorption (for example using ion chambers). The beamstop is usually placed before the Kapton® window and just before the detector. The choice of detectors on SAXS baemlines may depend on many factors including background or dark count, pixel size and detector speed. The importance of these factors depends on the type of experiments to be conducted.

3.2 Results and discussion

The CMCF-ID beamline is an undulator based beamline dedicated for single crystal diffraction (Figure 3.1) [89–92]. To enable future tests for SAXS/WAXS measurements on the baemline, a Vacuum and a He chambers have been designed and constructed.

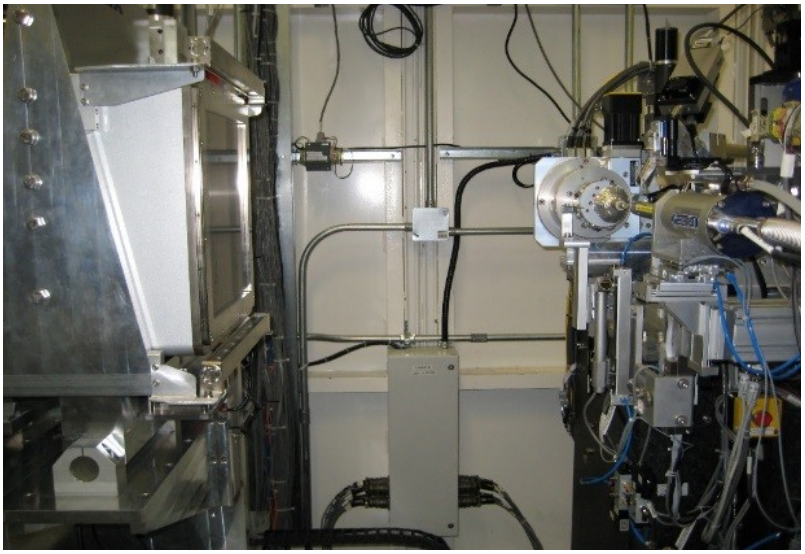

Figure 3.1. The CMCF-ID beamline endstation.

3.2.1 Vacuum SAXS /WAXS flight path

Scattering from partially disordered and disordered systems is usually very week. Thus, to enable SAXS measurements at the CMCF, a vacuum chamber was made to be placed between the sample and the detector (Figure 3.2). The chamber starts with a cone having a 30 microns Mylar window of ~ 7 mm diameter. The cone is made of Teflon (fluorinated hydrocarbons) as a low scattering material and with absorption edges that are far away from used energy range (8-12 keV).

The window at the detector was made of 50 microns Kapton® (polyimide film) and was glued to an aluminum ring.

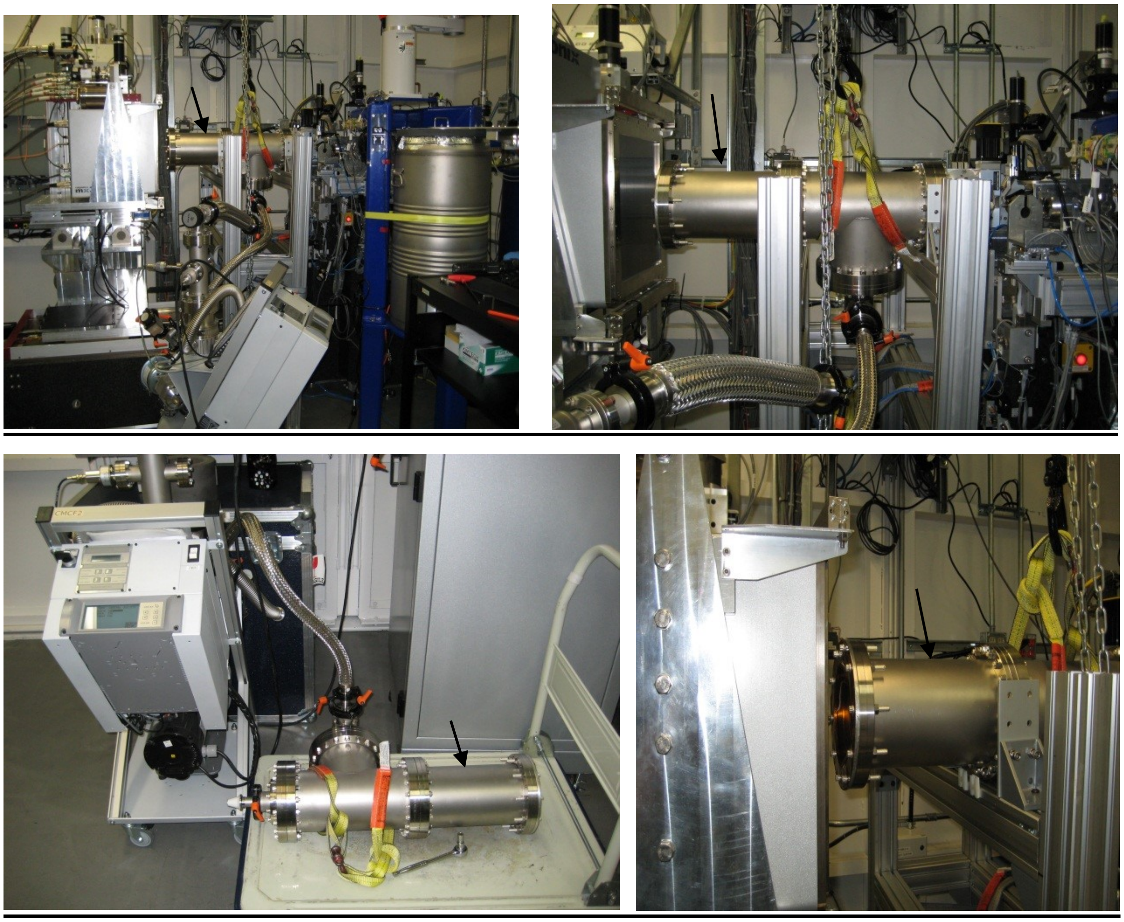

Figure 3.2. Vacuum flight path.

The figure shows the vacuum flight tube mounted on a table located between sample and the detector on the CMCF-ID beamline. The tube is connected to a regulator and a vacuum pump.

The beamstop was shaped from a silver wire that is ~ 3 mm thick and was placed inside the chamber to block the main beam before reaching the Kapton® window, and thus avoiding scattering from the window (Figure 3.3). Silver is usually used as a material of choice due to its low fluorescence at the used energy range. A semi-circular groove of ~ 2 mm depth was made at the front end of the beamstop (i.e. the end facing the beam). The latter, is made to prevent the scattered rays from beamstop surface from reaching the detector.

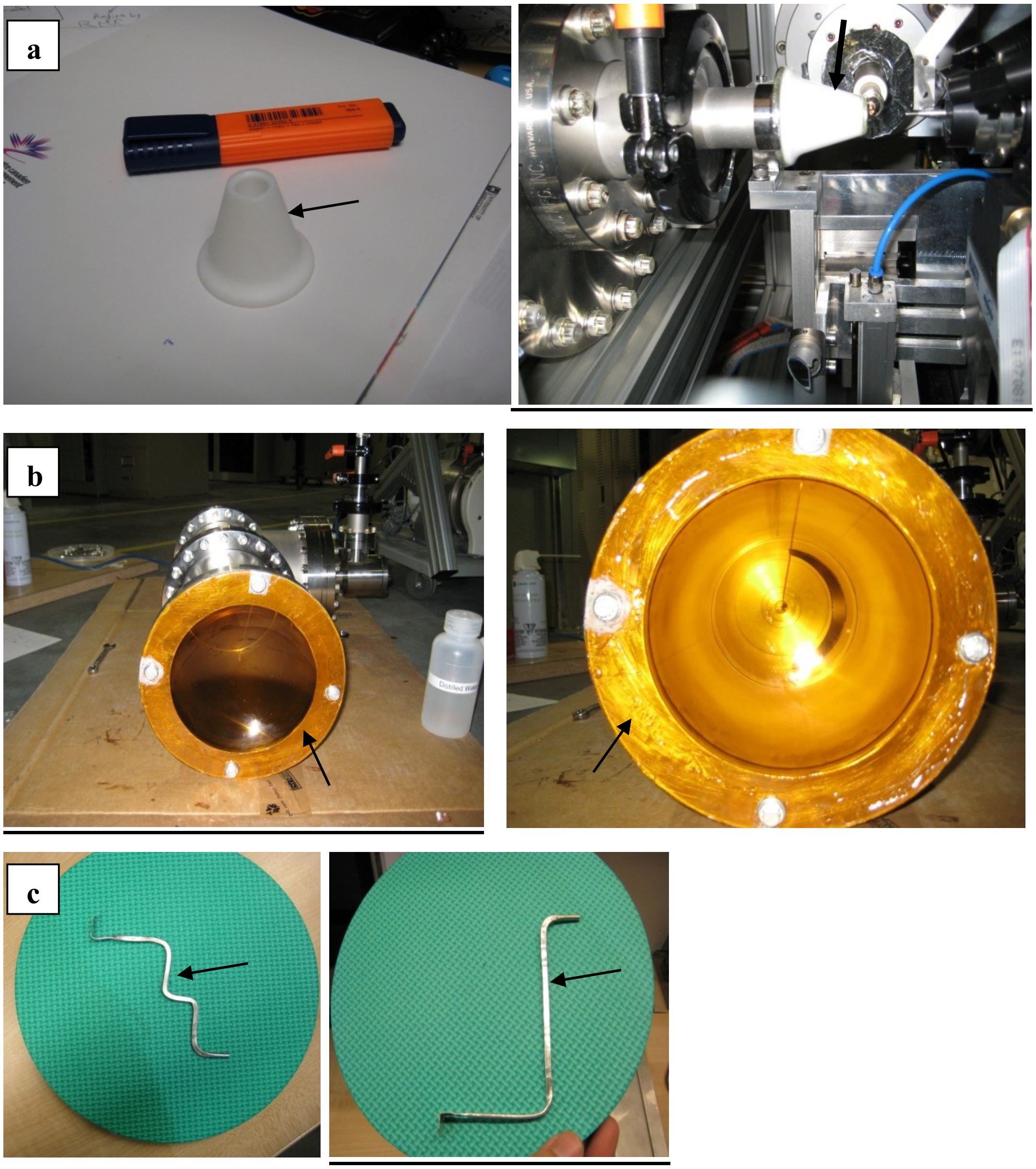

Figure 3.3. Elements of the vacuum flight path.

a) The used Teflon cone with a 30 microns Mylar window at it apex. b) A Kapton® window (50 microns thick) placed on the end of the vacuum tube facing the detector. c) Different prototypes for the silver beamstop before glued inside the tube.

3.2.2 Helium diffraction flight path

A helium chamber was designed and constructed from PVC pipes (Figure 3.4). The front terminal of the pipe (toward the sample) was capped by a cone with a 30 microns thick Mylar window, while the detector facing end was sealed by a 50 microns thick Kapton® window. The beamstop was made from a copper wire with a 5 mm diameter attached to a small lead cylinder placed in the centre in order to block the beam. The copper wire was then glued inside the chamber just before the Kapton® window.

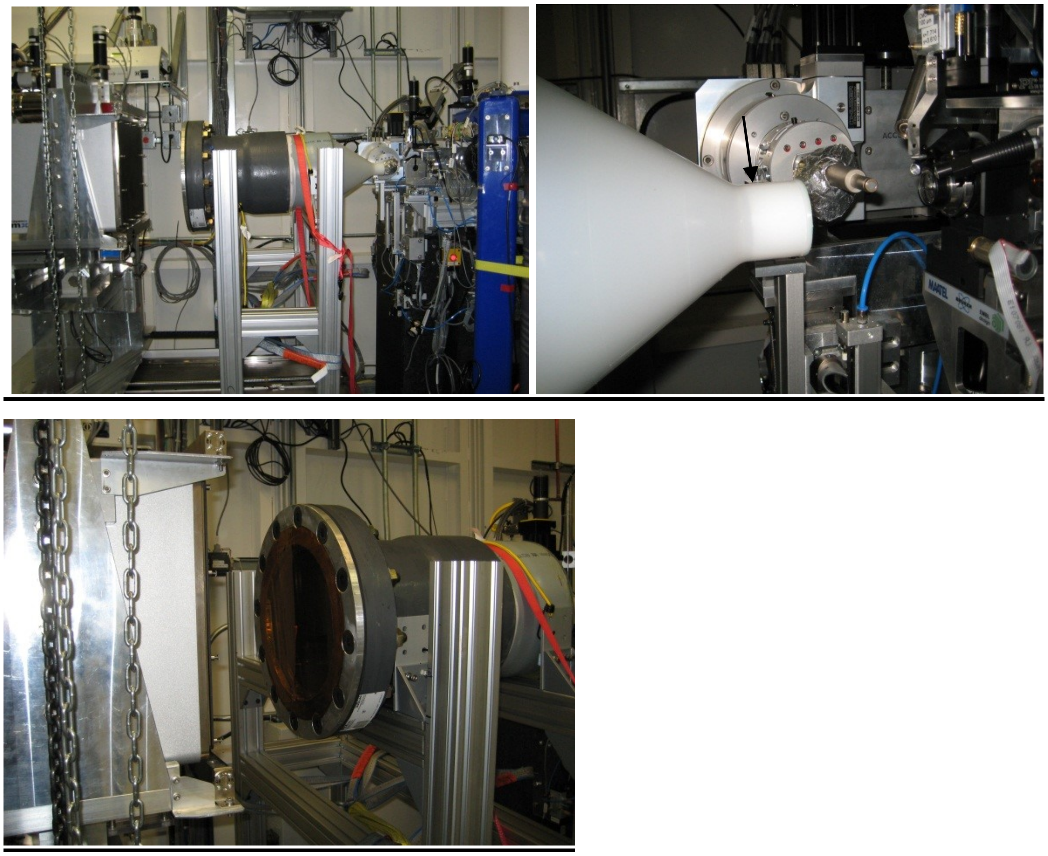

Figure 3.4. Helium flight path.

The figure shows the helium flight tube mounted on a table located between the sample and the detector on the CMCF-ID beamline.

4 AUTOMATION OF SAXS/WAXS ANALYSIS FOR LIPIDS

4.1 Introduction

Small and wide angle scattering (SAXS/WAXS) are structural techniques used for the determination of proteins as well as lipid systems in solution. For proteins, low resolution models can be obtained from dilute water soluble proteins [93,94]. However at higher concentrations, a measure for interaction (e.g. the second virial co-efficient) can be calculated. The latter can be potentially be used as a measure of nucleation of the protein in a specific medium [95].

SAXS/WAXS can be used in the structural analysis of lipid systems. By structural analysis, I mean that it enables the identification of the supra-molecular arrangement (phases) taken by the molecules in the system as well as lattice parameters allowing the construction of idealized models of the system studied [49]. Moreover, structural parameters can be obtained from such experiments including disorder parameters and electron density profiles [96]. If the lipid system is diluted and discrete particles are formed, the scattering pattern at the small angle regime can provide information about the overall shape as well as the interaction potential or the size distribution if the particles are poly-disperse in size [97].

Many software packages or pipelines are available for the analysis of SAXS/WAXS data [88,98–103]. Some of which were written to provide excellent capabilities specifically for diffuse scattering purpose but does not provide tools for powder patterns with Bragg's peaks [98,103]. Others were written for the use in specific purposes or specific portions of the analysis [101,104–106]. Some are dependent on commercial packages (e.g. Matlab®). Many beamlines use code that was written to be used locally on the beamline. On the other hand, powder diffraction software provide tools for crystalline samples but do they not consider diffuse scattering. Thus, there is a lack of a common platform for data analysis that can provide a global tool for a wide variety of samples. Furthermore, there are a variety of methods and scattering models that are commonly used in the analysis of scattering patterns of lipids that are not available in any of the available packages. Most biophysics labs that study bio-membranes tend to write their own local code e.g. using Matlab®.

The lack of a global platform hinders the standardisation of analysis methods and makes the comparisons between different methodologies challenging.

A pipeline for the automated data reduction and basic analysis of SAXS/WAXS was developed. This open source software is aimed to be as a stand-alone system or integrated into other software systems. Generally, it is designed to be suitable for rapid screening of samples on synchrotron beamlines. In the following sections, current progresses as well as future developments are presented.

4.2 Results and discussion

XPODS software (X-ray analysis software for Partially Ordered and Disordered Systems) is a set of modules written to automate SAXS/WAXS data reduction and analysis. The software is written in Python and FORTRAN. It is designed to act as a pipeline that starts by reading raw images and an input parameter file. The images would be reduced to a 1D curve upon which standard data analysis would be applied. Though written as a pipeline, the modular system allows further expansion so that certain modules can become independent programs that can be used independently, while still keeping the pipelines functional. The program is composed of a set of basic/lower level modules that performs various processing tasks (Figure **4.1**). These basic modules are utilized by two main higher level modules which run the processing workflows. Above those, there is a main control module that controls the remaining modules and that redirects the workflow to the suitable pipeline module according to the given commands. Figure 4.1 shows a general outline of the modular system of the software. Only the most important modules are shown, further details can be found in the software manual (**Appendix A**).

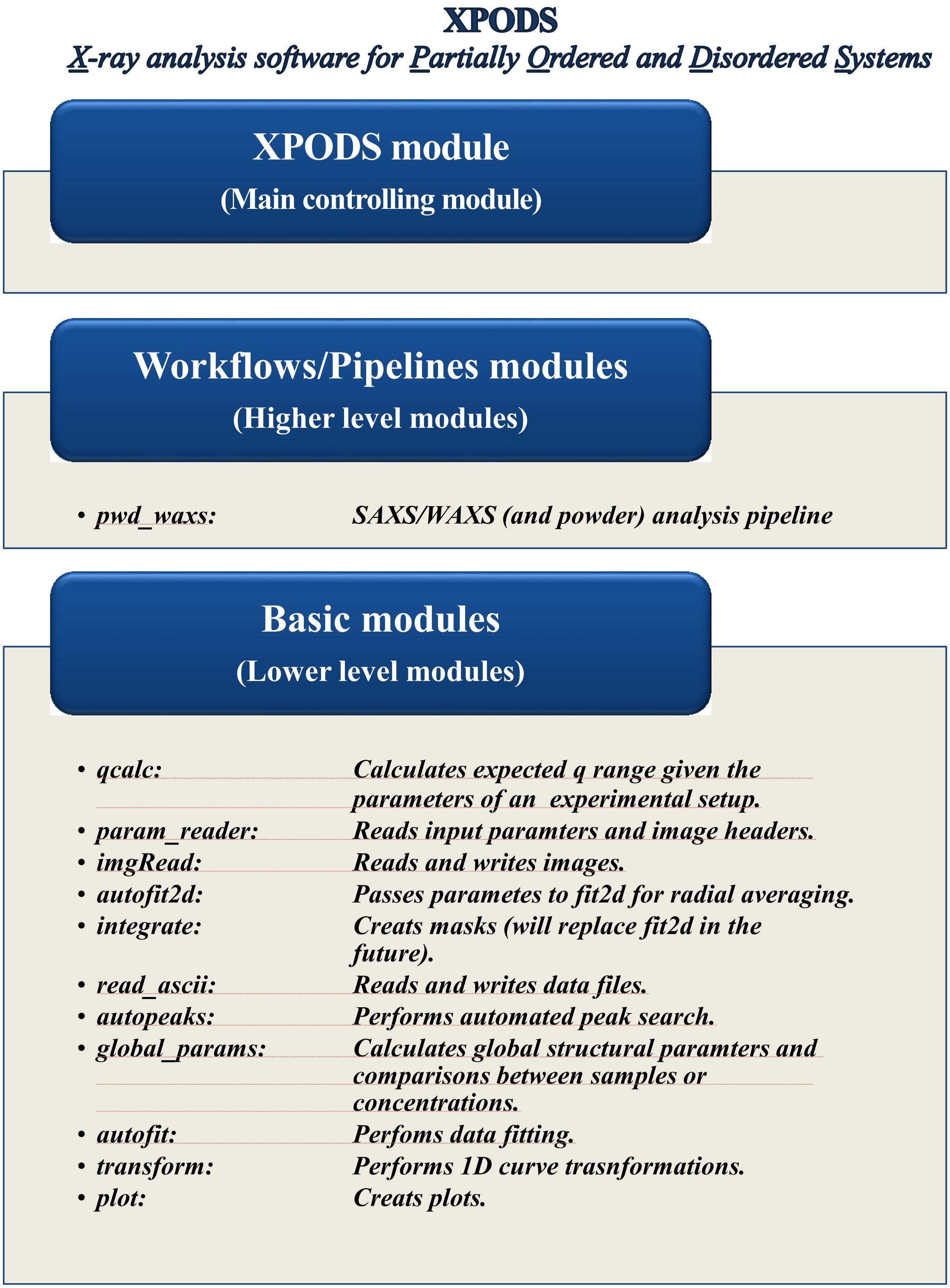

XPODS

X-ray analysis software for Partially Ordered and Disordered Systems

XPODS module

(Main controlling module)

Workflows/Pipelines modules

(Higher level modules)

pwd_waxs:	*SAXS/WAXS (and powder) analysis pipeline*

Basic modules

(Lower level modules)

qcalc:	*Calculates expected q range given the parameters of an experimental setup.*
param_reader:	*Reads input paramters and image headers.*
imgRead:	*Reads and writes images.*
autofit2d:	*Passes parametes to fit2d for radial averaging.*
integrate:	*Creats masks (will replace fit2d in the future).*
read_ascii:	*Reads and writes data files.*
autopeaks:	*Performs automated peak search.*
global_params:	*Calculates global structural paramters and comparisons between samples or concentrations.*
autofit:	*Perfoms data fitting.*
transform:	*Performs 1D curve trasnformations.*
plot:	*Creats plots.*

Figure 4.1. Main modular system of the XPODS.

XPODS is composed of a main control module which will pass input parameters to one of the higher level modules depending on the given command. These higher level modules will automate the processing using functionalities provided by the basic modules.

4.2.1 The Wide Angle X-ray Scattering (WAXS) and powder diffraction pipeline

Briefly, images are read by the *imgRead* module and a mask search is performed by the *integrate* module. The mask search starts at the approximate / initial given beamcentre and the mask is found according to a signal: noise ratio cut-off (i.e. the intensity ratio of current pixel: beamcentre pixel) (Figure 4.2). Optionally, a threshold mask can also be applied (Figure 4.3).

The experimental parameters (in the image header or *prp* files) are then piped into *fit2D* and a radially averaged curve is obtained. The output files are in simple *ascii* format where data is put in three columns (2θ, intensities and errors in intensities) or four columns (2θ, intensities, errors in 2θ and errors in intensities). The errors in the diffraction angle (2θ) are currently by default set to zeros, whereas the errors in the intensities are the standard deviation of the radially averaged intensities as calculated by *fit2D*.

XPODS will then read the produced files. If the appropriate parameters are given, the program will normalize for flux, time and correct for absorption. Optionally, polarization and Lorentz corrections can be applied. Corrected curves in the same folder will be averaged by default (i.e. will consider them as multiple images of the same sample). If a background is given, it will be subtracted. Results are provided in scales of 2θ, q and $d - spacing$. The module *autopeaks* will then do a peak search to find peaks, if any. Identified peaks are then fitted into the given peak profiles using a non-linear least squares fitting algorithm. The program makes use of the general fitting functions available in the python library *SciPy*. Finally, the integral of the peaks will be calculated and the ratios between the positions of the peaks will be tabulated.

In general, plots and output files are created at every step to keep a record of the processing. It is possible to process multiple samples/projects as a batch. In this case, XPODS will make comparison plots between the processed samples/projects.

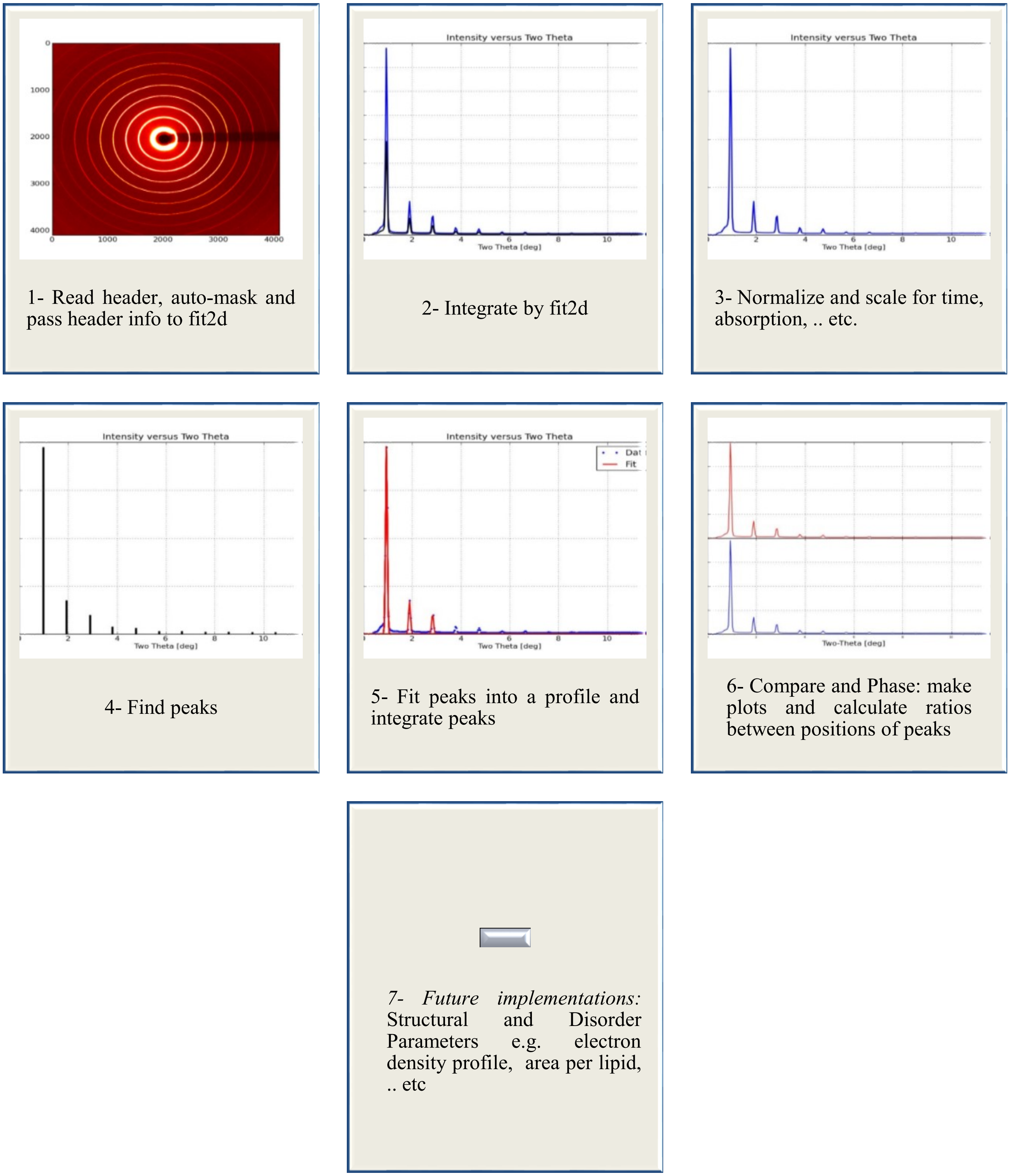

1- Read header, auto-mask and pass header info to fit2d

2- Integrate by fit2d

3- Normalize and scale for time, absorption, .. etc.

4- Find peaks

5- Fit peaks into a profile and integrate peaks

6- Compare and Phase: make plots and calculate ratios between positions of peaks

7- Future implementations: Structural and Disorder Parameters e.g. electron density profile, area per lipid, .. etc

Figure 4.2. Workflow of processing WAXS data in XPODS.

4.2.2 Numerical example

Silver behenate is a standard powder used for calibration of both the distance and beam centre in SAXS/WAXS experiments. This is because it gives several strong rings in the mid and low angle regions [107,108]. The first ring appears at a *d-spacing* of $d = 58.380$ Å. If finely grinded powder is used, the peak shapes or profiles can act as an indicator of quality of the beam. In this section, numerical example of silver behenate images processed by XPODS is shown.

Images were taken at the BL2- 4 beamline at SSRL, with a flight tube length of 1100 mm. The beam centre was found using *fit2D* and the sample to detector distance was refined so that the *d-spacing* of the first ring was equal to 58.380 Å. Peaks were found and fitted to Lorentzian profiles (Table 4.1).

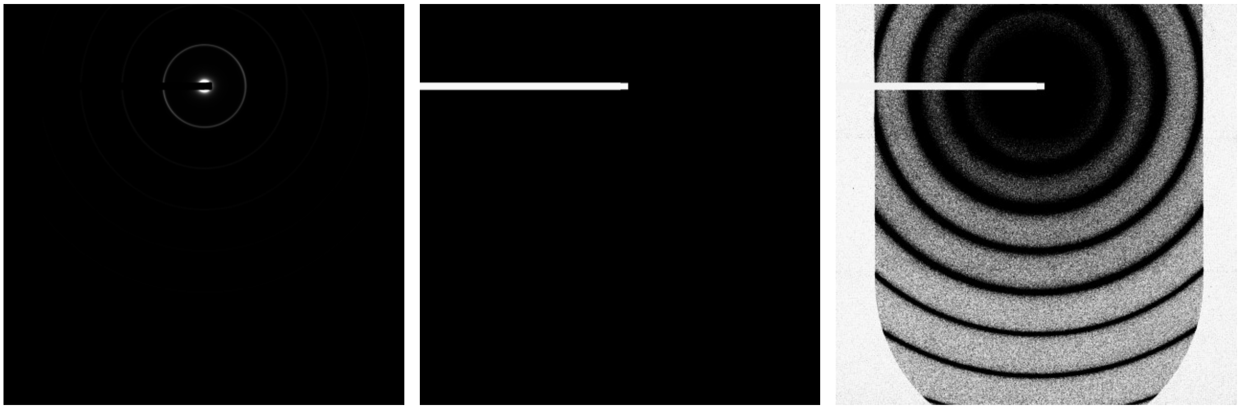

Figure 4.3. Masking in XPODS.

The figure shows origenal image, beamstop masked image and image after applying a threshold mask.

Height	**Centre (2θ angle (degree))**	**FWHM**	**Width**	**Sigma**	**Point index**
1.000E+03	1.109	2.378E-02	3.500E-02	1.100E-02	2.080E+02
1.596E+02	2.218	2.582E-02	3.800E-02	1.097E-02	1.317E+03
9.308E+01	3.325	2.650E-02	3.900E-02	1.125E-02	2.424E+03
3.122E+01	4.435	2.718E-02	4.000E-02	1.154E-02	3.534E+03
2.192E+01	5.542	2.854E-02	4.200E-02	1.212E-02	4.641E+03

Table 4.1. Automatic peak identification.

The table shows found peaks and estimated parameters that were used in fitting to the required peak profile functions.

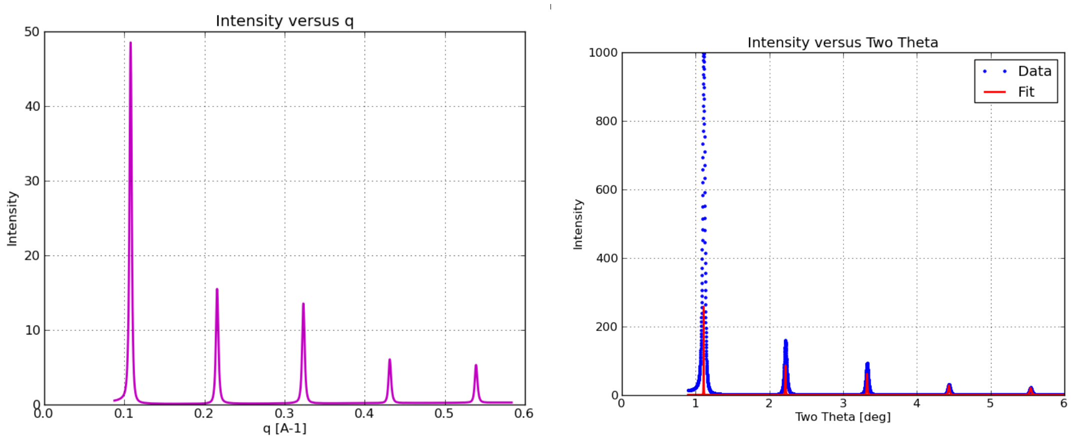

Figure 4.4. Peaks profiles of silver behenate.

The figure shows plotted peaks and fitted profiles.

Peak (2θ angle in degrees)	Q [A-1]	d-spacing [A]	S [A-1] (s=1/d)	Intensity (Height)	Integral	Relative intensity (Height)	Relative integrated intensity
1.109E+00	1.079E-01	5.826E+01	1.717E-02	1.000E+03	6.642E+01	1.000E+02	1.000E+02
2.218E+00	2.157E-01	2.912E+01	3.434E-02	1.596E+02	2.934E+01	1.596E+01	4.416E+01
3.325E+00	3.234E-01	1.943E+01	5.147E-02	9.308E+01	2.263E+01	9.308E+00	3.407E+01
4.435E+00	4.314E-01	1.457E+01	6.865E-02	3.122E+01	1.427E+01	3.122E+00	2.148E+01
5.542E+00	5.388E-01	1.166E+01	8.578E-02	2.192E+01	1.191E+01	2.192E+00	1.799E+01

Table 4.2. Silver behenate peaks profiles.

The table shows the positions, integrated intensities and relative intensities (considering highest peak as 100 %) of silver behenate peaks.

No.	**Position (q nm-1)**	**Ratio (relative to the first peak position)**
0	1.079E-01	1.000
1	2.157E-01	2.000
2	3.234E-01	2.999
3	4.316E-01	3.100
4	5.390E-01	4.997

Table 4.3. Peak positions ratios of silver behenate.

The table shows the ratios between the positions of the peaks from the position of the first peak.

The ratios between the peaks from the first peak were found to be equally spaced within the range of errors which is what is expected (Table 4.3) i.e. the ratios between peak positions is *1:2:3:4:5*.

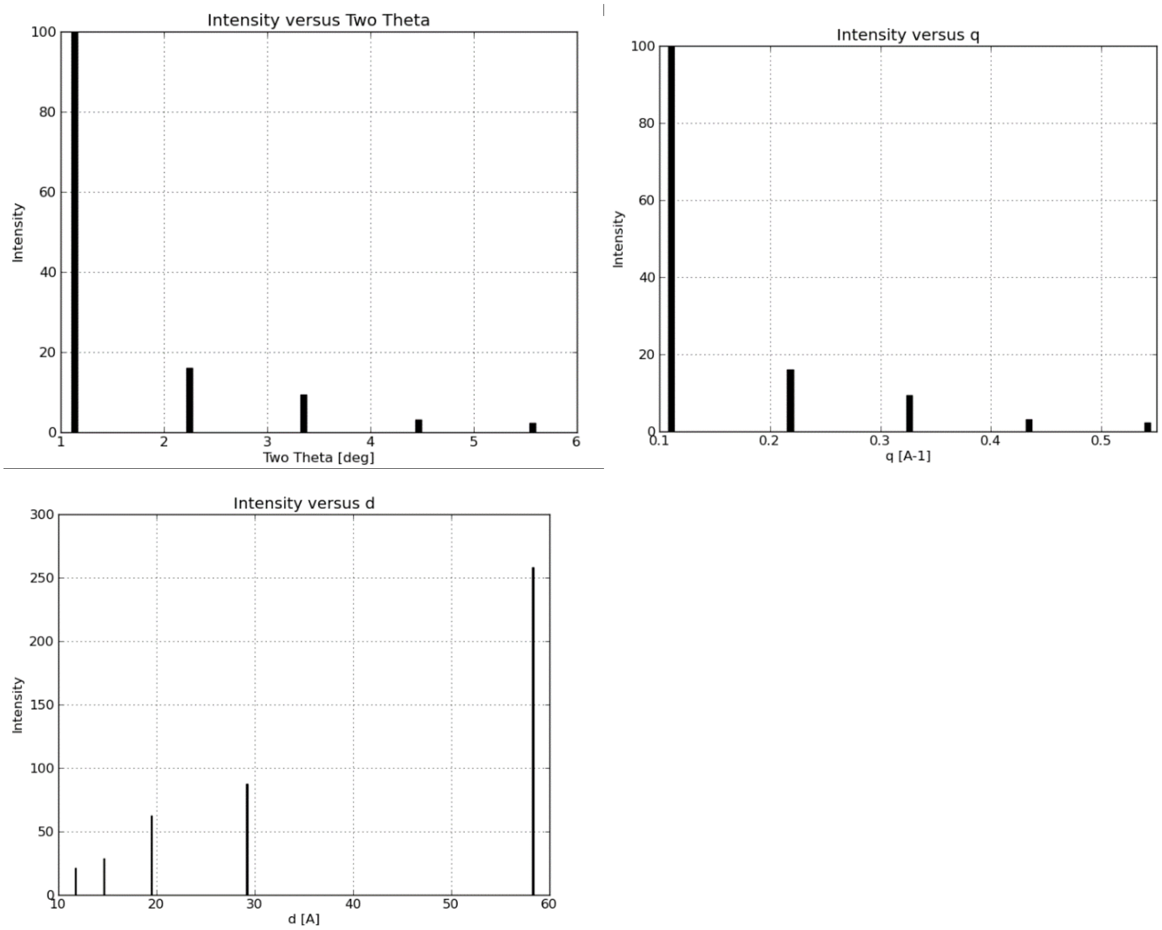

Figure 4.5. Bar plots of silver behenate peak positions.

Silver behenate peaks plotted as bar plots on 2θ, q and d-spacing scales.

4.3 Conclusions and future prospective

In this chapter, the feasibility of automation of SAXS/WAXS data reduction and analysis was shown. A pipeline was written to automated data reduction and initial analysis. The software however is still, at its early of development. At this stage, it uses other software such as *fit2D* to reduce the data. This dramatically reduces the flexibility and possible capabilities. Furthermore, although produces standard *ascii* files, one may consider the file system used to be still primitive. Moreover, the pipeline reads a very limited number of detectors raw image formats. Future work will therefore attempt to develop a mature file system for the software and expand on the input file formats. This is as well as modules to allow independence from other software will be written. This is in order to expand its capabilities and allow more flexibility in image analysis. Additionally, efforts will be put to parallelize the code and optimize the performance as well as improve user friendliness.

5 SAXS-BASED STRUCTURAL STUDIES OF GEMINI SURFACTANTS

5.1 Introduction

5.1.1 The structure and properties of gemini surfactants

Gemini surfactants are a class of cationic surfactants that have been used as a drug delivery system for molecules such as DNA [109]. They adopt different structures that may have a different ability to deliver the DNA [110–112]. Charge interactions and hydrophobicity are known to be the main deriving forces of such amphipathic molecules to adopt certain arrangements. Varying the charge ratios between the gemini surfactants and the DNA in formulations by changing their concentrations as well as changing the concentrations of the other helper lipids will have an effect on the structure of the formed particles. Understanding the structure of these nanoparticles should greatly enhance our knowledge of the delivery process.

The gemini surfactants molecule is composed of two monomers that are linked chemically at or near the head group. The term is used for all dimeric surfactants despite of the length of the spacer. The molecule has two positively charged head groups and two hydrophobic tails (of length m). The head groups are linked with a spacer (of length s). The different types of gemini are named according to the length of the hydrophobic tail and the length of the spacer (m-s-m) (Figure 5.1) [113]. In this chapter a study of the structural features of the 12-3-12, 12-7-12 and 16-3-16 gemini surfactants and their corresponding DNA-complexes is presented.

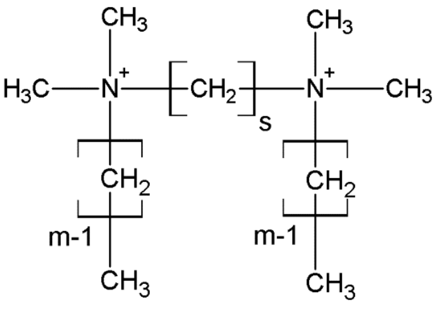

Figure 5.1. The chemical composition of the gemini surfactants molecules.

The molecule is characterized by having two polar head groups and two hydrophobic tails. The head groups are linked by a spacer.

5.1.2 Gemini surfactants as a drug delivery System

Previously, the several types of gemini surfactants have been tested for nucleic acid transfection. Molecules with spacer and tail lengths (s= 3) and (m=12 and 16) were studied and their ability to transfect a plasmid coding for interferon-gamma was evaluated both in vitro and in vivo. Gemini surfactants with three carbon atoms spacer (s=3) showed a better ability to transfect the DNA into the cells for both chains (m=12 and 16). Both molecules were mixed with DNA in a 1: 10 charge ratio along with DOPE as a helper lipid. The complexes formed particles of size within the nano-range of 100-200 nm. SAXS/WAXS was used to identify the structural arrangement (phases) of the nanoparticles and it was generally concluded that the particles take polymorphic phases (multiple phases) [111,114,115].

5.1.3 The structure of the gemini-based formulations

The structure the lipid-DNA assemblies may influence its ability to deliver the DNA into the cells [77]. Since charge interactions and hydrophobicity are known to be the main driving forces of amphipathic molecules to adopt certain arrangements, it was postulated that varying the charge ratios of the gemini surfactant– nucleic acid in formulations will have an effect on the structure of the formulation particles, and thus have an effect on transfection. The target of this study can be summarized as follows:

1. To examine the effect of the change of relative concentrations of the building elements of the gemini nanoparticles, namely the nucleic acid drug, the gemini surfactant and the helper lipids.
2. To characterize the structural properties of different formulations. These formulations are prepared by varying the relative concentrations of their components.
3. To identify the most convenient relative concentrations of the different four components that would maximize the delivery of the DNA into the cells.

SAXS/WAXS was used to attempt to propose a structural model for the gemini-based lipoplex particles in different formulations. In this work, a systematic study of the structural properties of the formulations is presented. Further, the effect of varying the charge ratio is examined. The structure of the individual components of the formulation as well as the intermediate complexes was studied. The latter are then compared to the final scattering patterns of the formulations.

5.2 Methods

5.2.1 Sample preparation

Gemini surfactants (16-3-16, 12-3-12 and 12-7-12) were hydrated with double distilled water to a final concentration of 1 mM, 3 mM , 6 mM, 30 mM and 73 mM (hydrated solids). The latter four concentrations will be referred to as (1X, 2X, 10X and 25X), i.e. 1 fold, 2 fold, 10 fold and 25 fold concentrations, where 1X refers the dilute concentration usually used in transfection. The resulting solutions were used directly in the x-ray experiments to obtain the scattering patterns of the pure gemini surfactants. The gemini-DNA complexes were prepared by mixing the previously prepared gemini surfactants solutions of concentrations (1X, 2X, 10X and 25X), with DNA in different DNA: gemini surfactants charge ratios (1:20, 1:10, 1:5, 1:1 and 5:1). The charge ratios were calculated from the phosphate: nitrogen ratios (P/N). The DNA plasmid pGTmCMV.IFN-GFP was used in the preparation of the samples. The resulting dispersions were vortexed to ensure proper mixing.

5.2.2 X-ray data collection, reduction and interpretation

The final SAXS/WAXS experiments were performed at the BL4-2 beamline at SSRL using the energy of 11 keV and sample to detector flight path of 1100 mm. All samples were loaded in 1.5 mm boron rich glass capillaries. Images were collected using 10-20 seconds exposure times. Several images per sample were taken. The semi-automated image reduction and processing was made by XPODS (see Chapter 4 for further details), which is briefly described as follows. After obtaining the 1D radially averaged scattering curve, all diffraction patters were checked visually for radiation damage. Patterns that showed radiation damage were removed. If no signs of clear radiation damage observed, curves were averaged. All scattering curves were normalized, by exposure time, flux and were corrected for absorption. An automated peak search, peak profile fitting and peak intensity integration was performed (using XPODS). Where applicable, the ratios between peak positions were used for phase identification.

5.3 Results and Discussion

5.3.1 The structure of 12-s-12 gemini surfactants and 12-s-12 DNA complexes

Previous neutron scattering studies have shown that the 12-3-12 and 12-6-12 gemini surfactants neutron scattering patterns fits to a tri-axial ellipsoid shaped micelles. Neutron scattering patterns from micelles are known to be dominated by the scattering from the core of the micelles. Whereas, x-ray scattering patterns can be dominated by the counter ion shells of the micelles [116]. Further, the fitting results have shown that longer spacer gemini tends to form a more flattened shape micelles [112]. These findings had generally confirmed the earlier electron microscopy images of 12-2-12 and 12-4-12 which have shown that the micelles grow into worm-like (or thread-like) shapes as the gemini concentration increases. The electron microscopy images showed that the gemini micelles start with spheroidal shapes and then undergoes elongation as the concentration increases. When the gemini concentration is high enough, the long micellar threads then stack adjacent to one another [117].

The scattering patterns from 12-3-12 obtained in this study (Figure 5.2) are generally consistent with previous studies and show similar features. From the shape of the scattering curve and previous studies discussed above, it can be seen that the x-ray scattering patterns that are presented in this study are dominated by the bromide ions shells. This is also consistent with the well-known core and shell models for charged micelles [118,119]. As the concentration of the gemini surfactants increases the Gaussian-shaped lobe increases in intensity and shifts towards a lower q due to the increase of the size of the individual micellar threads (Figure 5.2). At even higher concentrations, the long threads start to stack on top of each other in a regular manner but with considerably large stacking faults. This gives a rise to a Bragg's peak at ~ 150 Å which refers to the distances between the threads. An inset of the graph shows that this peak is composed of many overlapping sharper peaks that are fused together to make one broad peak. This may be due to the variation of the distances between the threads, and hence the presence of multiple unit cells with variant lattice parameters.

Upon the addition of DNA to the charged surfactants, a sharp Lorentzian-shaped peak appeared in the scattering patterns (Figure 5.3) at an average d-spacing (amongst all charge ratios) equal to ~ 42.46 Å for the concentration corresponding to 25X. This indicated that a new crystalline DNA-gemini complex is formed. The position of the sharp peak is related to the lattice parameter of the formed crystallites and for concentrations corresponding to 25X it was found to be at a d-spacing equal to 44.037, 43.161, 43.984, 42.00 and 39.133 Å for DNA: gemini charge ratios 1:20, 1:10, 1:5, 1:1 and 5:1, respectively. It has been shown previously that a DNA-DNA correlation is usually exist in DNA-lipid phases. This DNA-DNA correlation leads to the appearance of a relatively sharp Bragg's peak at a d-spacing corresponding to the distances between the DNA helices [70,77,120,121]. Therefore, based on these studies, the sharp Bragg's peak that appeared upon the addition of the DNA, can be explained by the presence of a DNA-DNA correlation. Thus, the repeating DNA-DNA distance is related the lattice parameter (i.e. related to the size of the formed unit cell). Higher order peaks did not appear in the scattering patterns due to the high degree of disorder in the formed lattice.

As the DNA concentration increases compared to the gemini, the Gaussian shaped lobes from the free unbound gemini gradually disappear, indicating that more micelles become bound to the DNA. One would expect that the ratio of the integrals of both of the overlapping patterns would quantitatively reflect the free: bound gemini ratio. A closer look at the scattering pattern of the 25X DNA-gemini complex containing excess gemini (charge ratio of 1:20 in Figure 5.4) one can see a remaining signature of the previously seen inter-threads peak in the pure gemini surfactants (Figure 5.2) but with a shift to a much smaller q (momentum transfer). This may be due to that the DNA had perturbed the threads stacking and had made this distance to be much longer. The charge ratio variation effect described above is seen in all concentrations in a similar way (Figure 5.5). In other words, the formation of a crystalline lattice is seen at all concentrations and the position of the peak is similar (for the same charge ratio). This fact is of extreme importance since the micelles lengths are changing at different concentrations but with a fixed thicknesses or radii (i.e. fixed cross section). Therefore, one could conclude that the DNA-DNA distance is related to the thickness of the micelles (micellar bilayer).

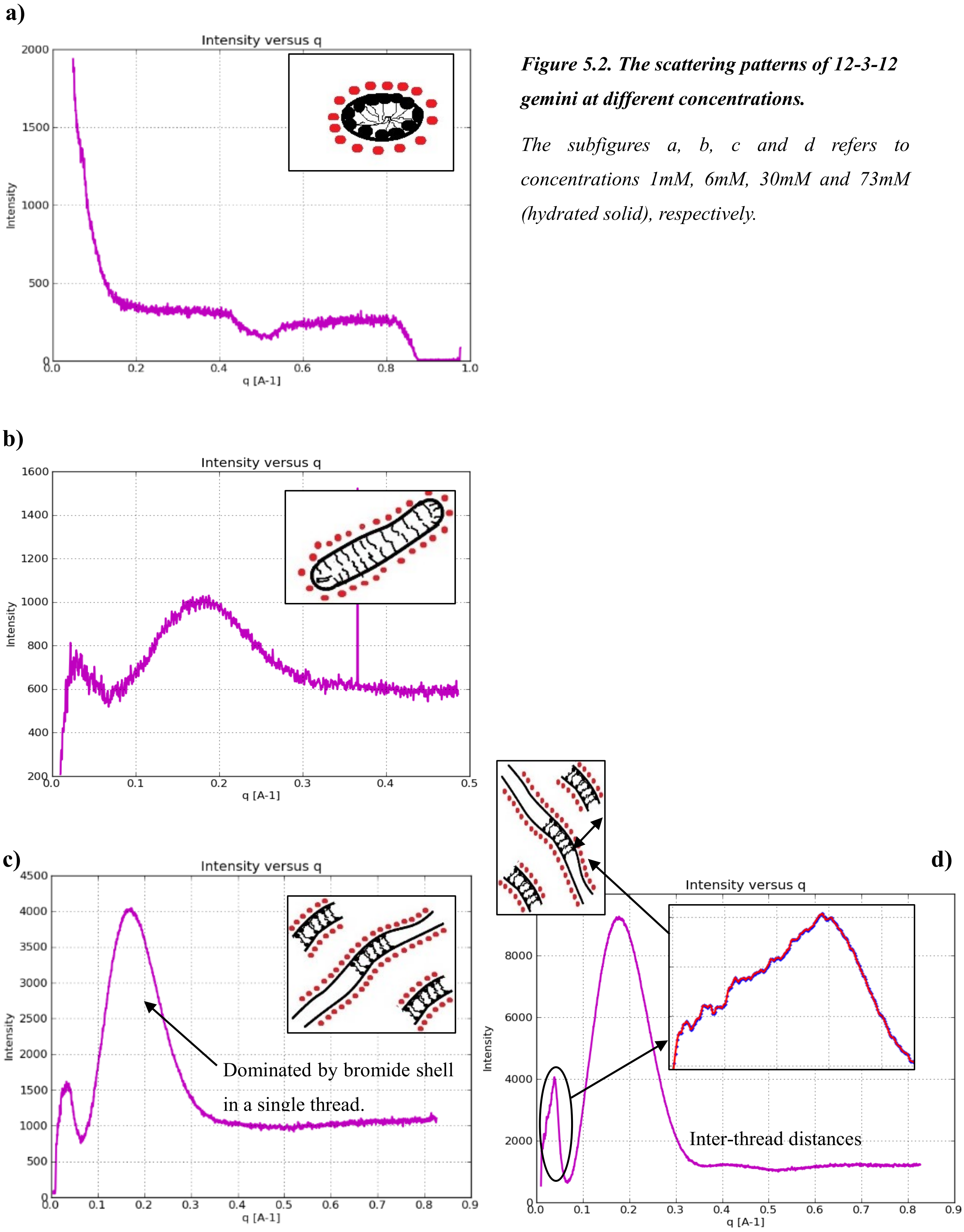

Dominated by bromide shell in a single thread.

Inter-thread distances

Figure 5.2. The scattering patterns of 12-3-12 gemini at different concentrations.

The subfigures a, b, c and d refers to concentrations 1mM, 6mM, 30mM and 73mM (hydrated solid), respectively.

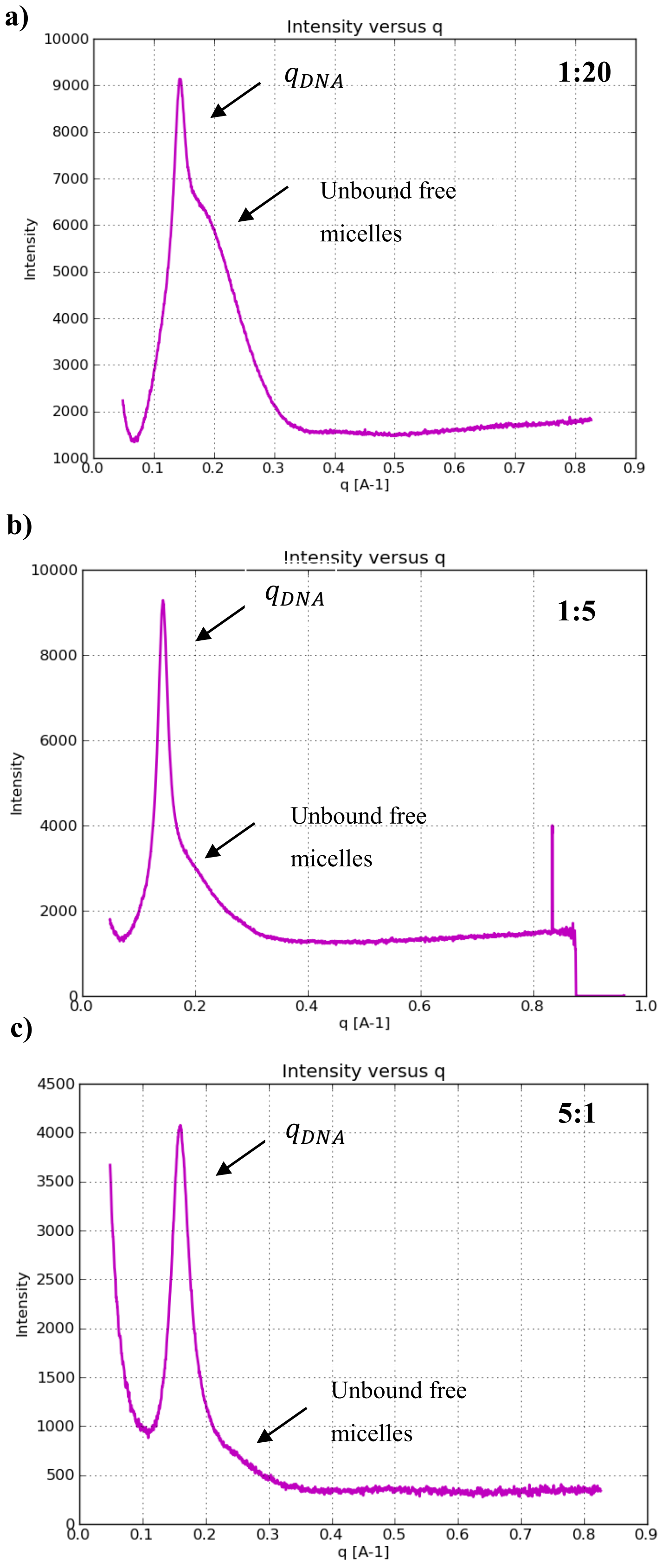

Figure 5.3. The effect of varying the DNA: gemini ratios (charge ratio) in gemini 12-3-12.

The figure shows the scattering patterns (a,b and c) from DNA-12-3-12 gemini complexes with DNA: gemini charge ratios of 1:20, 1:5 and 5:1, respectively. Clearly, the prominent peak is a composed of two overlapping peaks. The sharp Lorentzian-shaped peak is the DNA-DNA correlation peak, while the broad Gaussian-shaped lobe is the scattering from free gemini surfactants dominated by bromide counter ion shells.

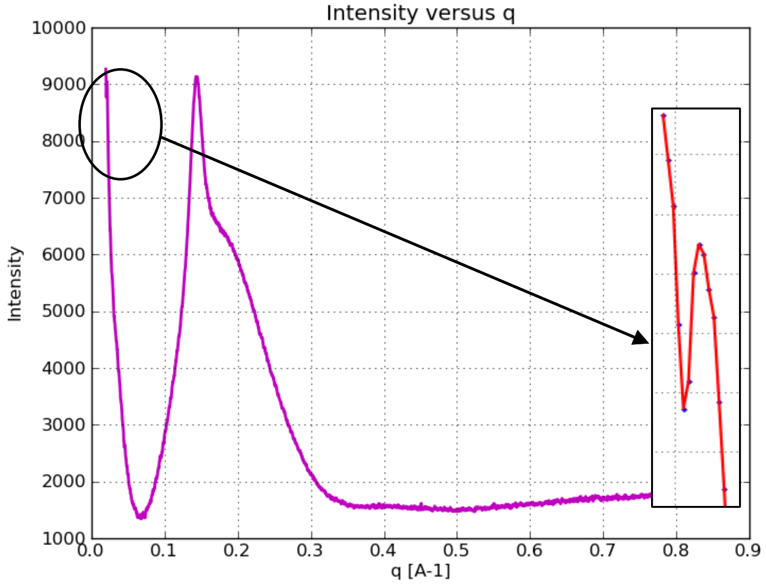

Figure 5.4. The effect of DNA on the inter-micellar threads distance.

The figure shows the full scattering pattern of the DNA-12-3-12 of the 25X concentration with charge ratio 1:20. The inset of the small angle region shows the presence of a weak Bragg's peak. This peak can be explained as the distances between the gemini threads. Thus, the distances between the threads had become much larger (compared to the pure gemini) upon the addition of the DNA. This is because the DNA goes in between the threads.

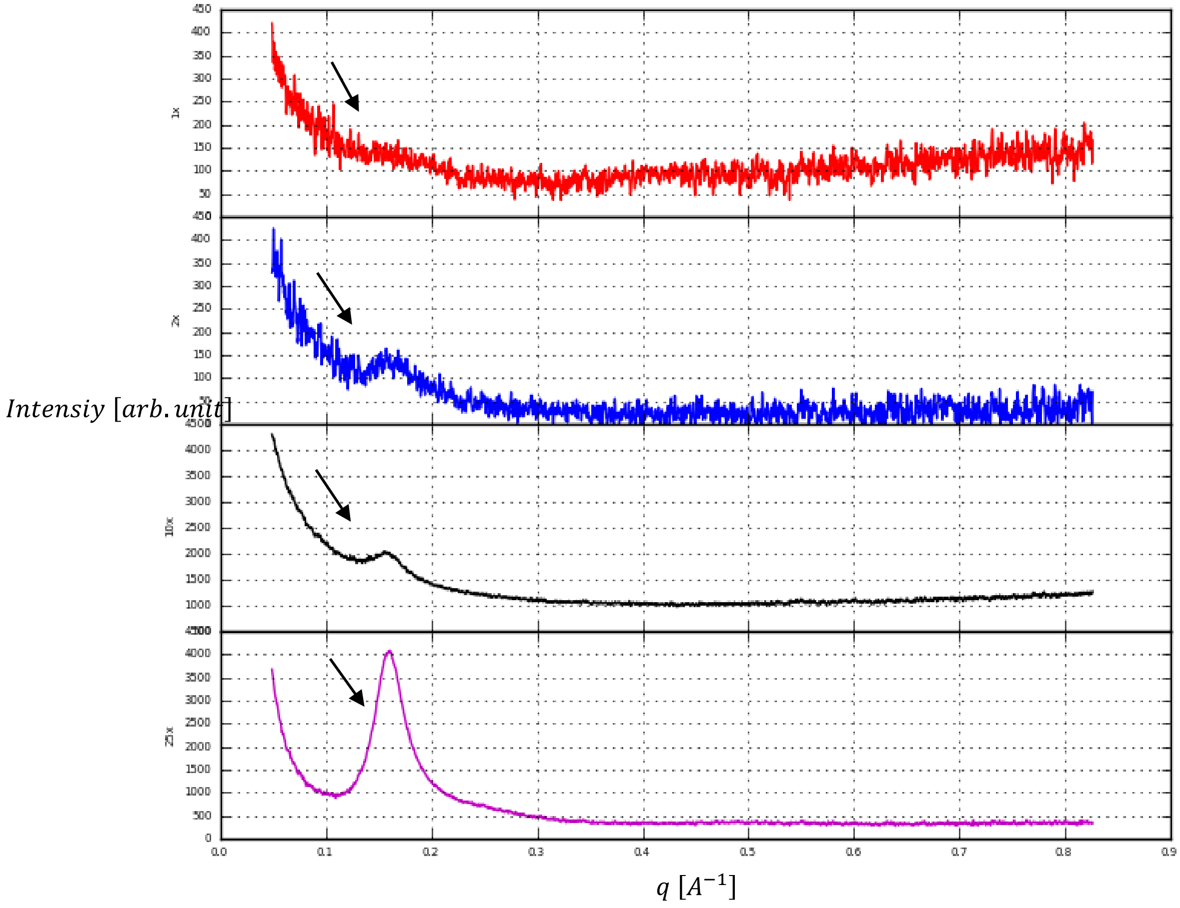

Figure 5.5. DNA-12-3-12 gemini.

The figure shows selected DNA-gemini complexes of the 12-3-12 gemini with 1:5 charge ratio at different concentrations. The scattering patterns from top to bottom refer to concentrations 1X, 2X, 10X and 25X, respectively. The arrow is pointing the Bragg's peak (or its remaining signature).

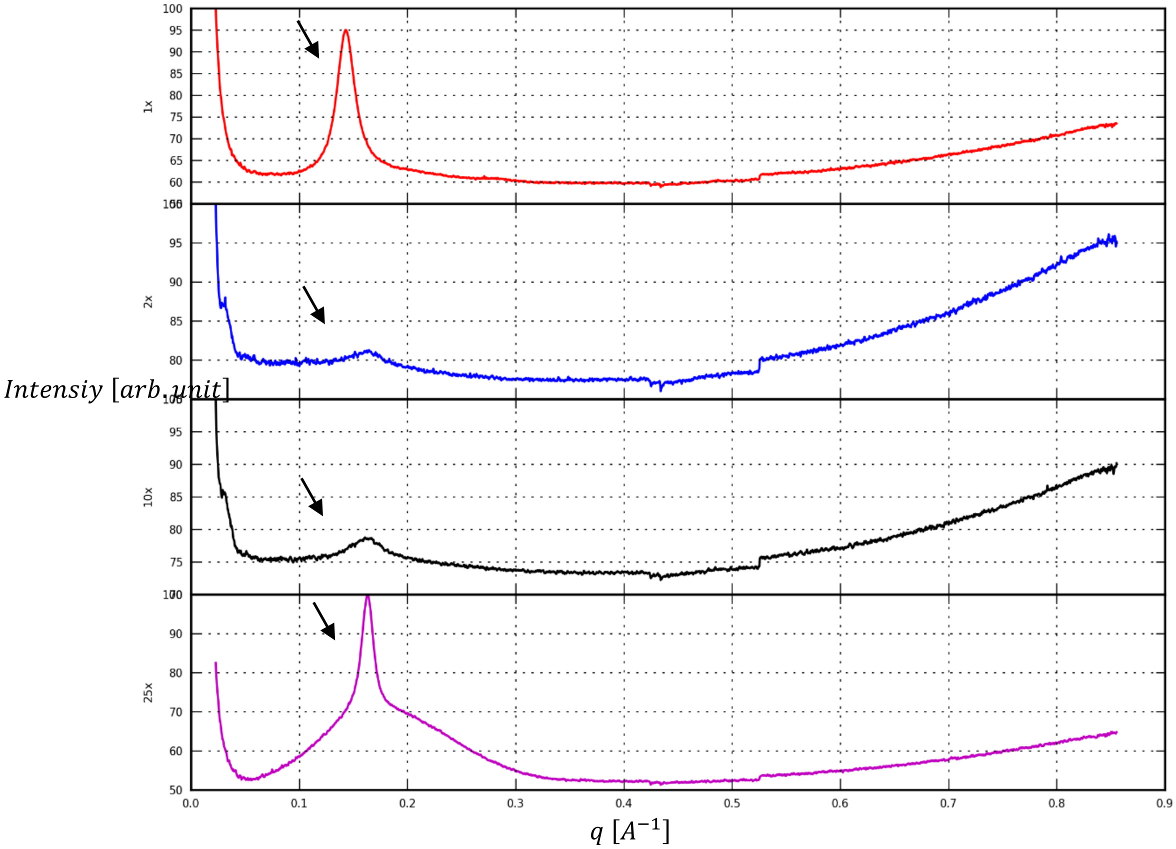

Figure 5.6. DNA-12-7-12 complexes.

The figure shows the scattering patterns of the DNA-gemini complexes of the 12-7-12 gemini with 1:10 charge ratio at different concentrations. The scattering patterns from top to bottom refer to concentrations 1X, 2X, 10X and 25X, respectively. The arrow is pointing the Bragg's peak (or its remaining signature).

Similar to 12-3-12, the DNA-12-7-12 scattering patterns at different concentrations, using 1:10 charge ratio, follows the same general trends (Figure 5.6). The background is not subtracted from these patterns. Water subtraction leads to negative intensities in the first three concentrations. This may be due to the loss of the counter ion shells after the binding to the DNA leading to a much less the scattering power, except at high enough concentrations. Further, this effect may have increased by the presence of water between the tails in the case of long spacers which leads to lower contrast micellar cores. One can see that there exist a variation in the patterns of the DNA 12-7-12 complexes. The reason for the reduced sharpness of the Bragg's peak may be due to the high CMC of the 12-7-12 and due to the much lower tendency to form a crystalline complex with the DNA. In other words, the 12-7-12 gemini micelles has a lower binding affinity to the DNA and thus x-ray snap shots of the solution are variant from one image to another. Some of the images collected from the first and last concentrations also had the same defect and thus were excluded from the analysis. Despite that, it is clear that the same concept as the 12-3-12 gemini applies, i.e. at excess gemini (example at 1:10 DNA: gemini charge ratio), free gemini micelles exist in the solution and only part of which makes a complex with DNA. The difference between the two gemini is only in the dimensions of the ellipsoid micelles (or the thickness of the micellar threads in high concentrations). The latter is also evident by the fact that the position of the DNA-DNA correlation peak is at a smaller d-spacing in the case of the 12-7-12 gemini DNA complexes (~ 38.16 Å at 1:10 charge ratio in the concentration corresponding to 25X).

5.3.2 The structure of 16-3-16 gemini surfactants and 16-3-16 DNA complexes

If the first Bragg's peak of the gemini surfactants 16-3-16 scattering pattern was ignored, the ratio between the positions of the consequent peaks were found to be:

$\sqrt{4}/_3 : \sqrt{4}/_{R^2} : \sqrt{4/3} + 1/R^2 : \sqrt{4/3} + 4/R^2$ … etc. which corresponds to a 3D hexagonal close packed lattice, where the ratio between the lattice parameters $R = c/a$. The relationship between the d-spacing and the lattice parameters is determined from the relationship:

$$\frac{1}{d_{hkl}^2} = \frac{1}{a^2}\left(\frac{4}{3}(h^2 + k^2 + hk) + \frac{1}{R^2}l^2\right) \qquad (5.1)$$

The Bragg's reflections were therefore indexed as hexagonal micellar lattice (space group *P63mmc*) in which micelles are stacked in layers (in the form layers ABABA ... etc.) (Table 5.1 and Figure 5.7). R initially was found to be equal to 1.55 which is close to previously reported (1.63) [61].This indexing was found to only fit the pattern if the d-spacing of the first peak was ignored. One could therefore interpret that bromide ions stack around cationic micelles leading to a super-lattice or sub-cell and thus adding to the complexity of the structure. Such finding seems to be similar to the observed effect of counter ion shells in other gemini surfactants examined in this study. The finding that ions play an important role in formation of the structure and are an essential part of the lattice is a finding that has been reported previously in literature [122]. The first peak can be therefore interpret as the distances between the bromide ions which would be 32.73 Å, which are located around the gemini micelles near the charged head. The lattice parameters *a* and *c* were found be equal to 30.05 and 49.88 Å (R= 1.66) after refinement. Figure 5.9 shows the diffraction pattern of the gemini 16-3-16 in solution in different concentrations. It is evident that the strongest peaks are still seen in the diluted solution indicating the same structure is retained in both diluted and concentrated samples.

Peak No.	d-spacing (Å) (experimental)	d-spacing (Å) (Calculated)	Indices (hkl)
1	32.8	-	-
2	26.0	26.0	010
3	25.2	24.9	002
4	24.4	23.1	011
5	16.4	18.0	012
6	14.7	15.0	110
7	14.6	14.0	013
8	13.0	13.0	020
9	12.6	12.9	112
10	12.4	12.6	021
11	12.3	12.5	004
12	10.9	11.5	022
13	?	11.2	014
14	9.8	9.6	114
15	9.3	9.3	015
16	9.1	?	?
17	8.2	8.3	115

Table 5.1. Indexing of the 16-3-16 gemini surfactants.

Table shows the indexing of the 16-3-16 gemini surfactants diffraction pattern. Lattice parameters were found to be: a = 30.05 Å, c = 49.88 Å and R = 1.66.

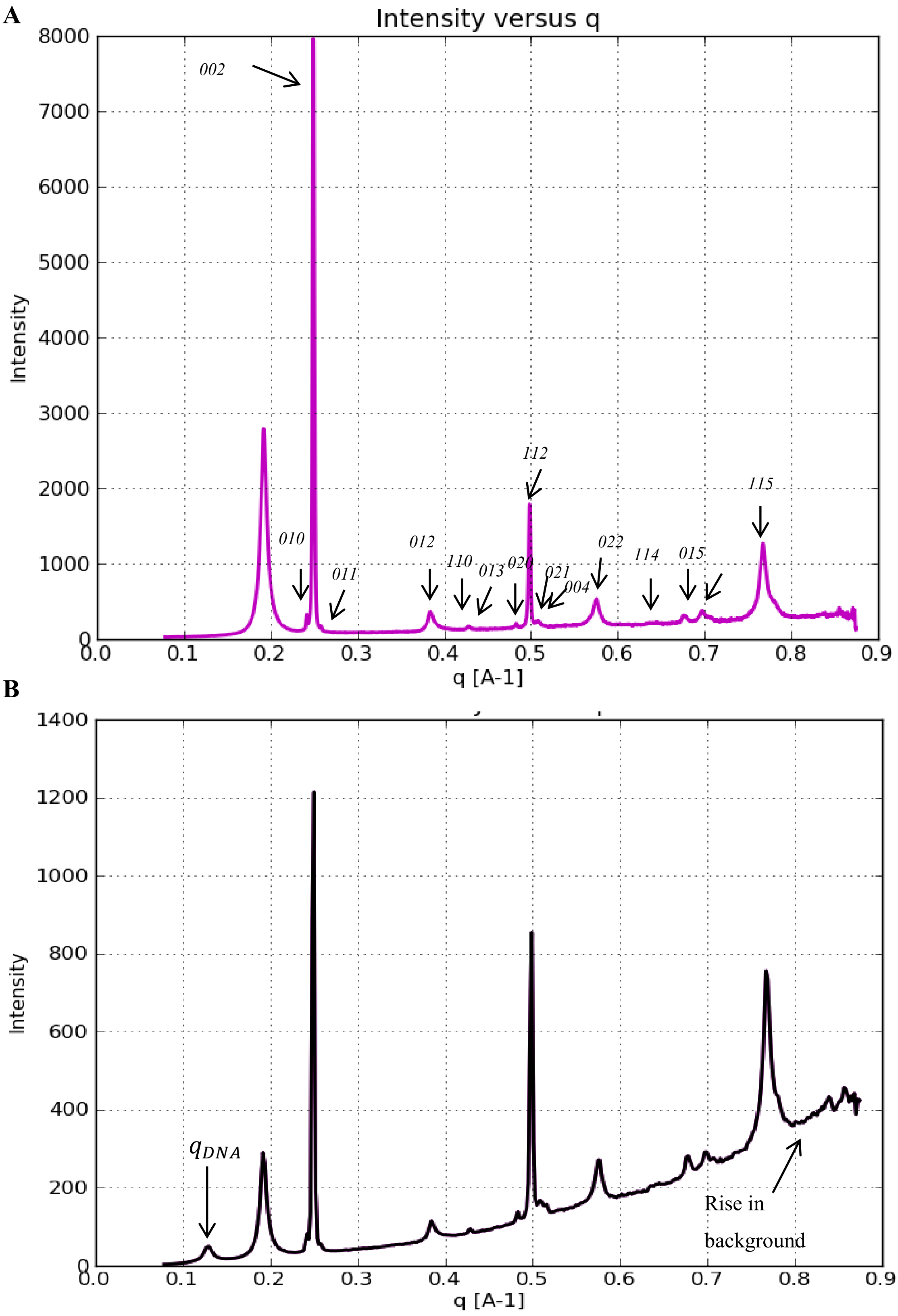

Figure 5.7. Indexing of 16-3-16 and the effect of DNA on the 16-3-16 gemini scattering pattern.

(A) The figure shows indexed reflections from concentrated gemini 16-3-16. (B) The figure shows the diffraction pattern of Gemini 16-3-16 – DNA complex. An extra reflection is seen representing the DNA distances.

The diffraction pattern and the proposed structure from this study (Figure 5.8) therefore explains the previously published AFM images [114]. The "sharp", step-like layering of the surfactants are visible in the AFM images. It is realized, that this is different from the much smoother surfaces seen in the images of the formulations [109]. Not surprisingly, the AFM images shows that the crystals are large disks. Moreover, Asawal et. al. has previously showed using small angle neutron scattering (SANS) that at concentrations that are higher than the CMC (2.5 and 10 mM), 16-3-16 are large disks that are 200 Å in diameter and 27 Å thick [123]. Thus, results shown in this study are consistent with the latter and infer that the large disks are a layer of combined or perhaps fused micelles. It is very important to realize that neutron scattering probes the 'core' only and may not see the effect of counter ion shells and hence the disk thickness obtained in this study is a few angstroms larger [116].

Interestingly, organo-silica fused porous material that was synthesised using the 16-3-16 gemini was shown to form layered (lamellar) continuous sheets with hexagonally packed patterns of pores [124]. The dimensions of the unit cell in this case were approximately three times larger compared to their corresponding dimensions reported in this study. It is worth noting that in fused organo-silica materials, the silica source surround the micelles during the synthesis and then fuses while the gemini surfactants acting as molds. The surfactants are then removed leaving pores in their original positions and the resulting material is composed of silica only (reviewed in [125]). The increase in the size of the unit cell seen in the resulting organo-silica may be due to the intercalation of the silica between individual micells and thus increasing the spaces between them.

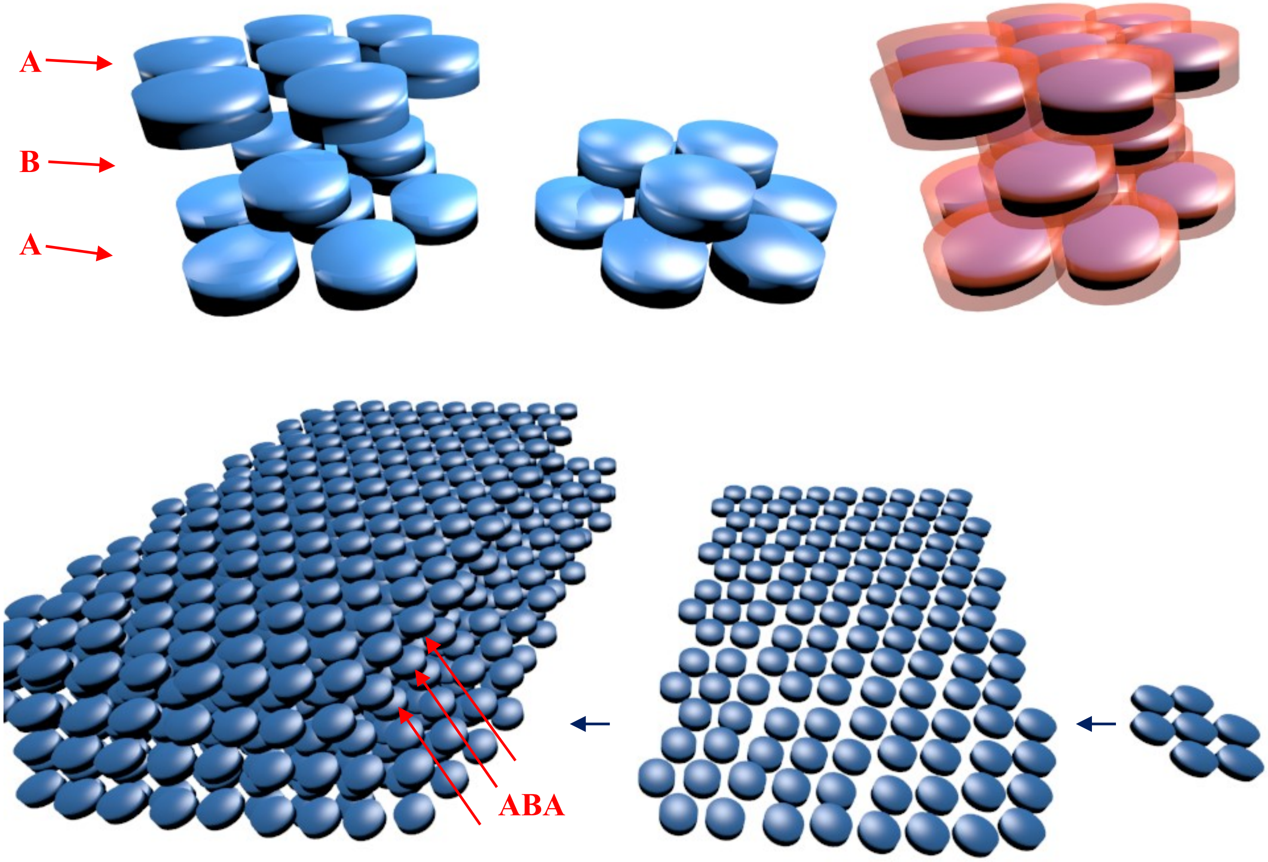

Figure 5.8. A schematic diagram of the proposed structural model of the 16-3-16 gemini surfactants.

Top panel: *A schematic diagram that shows the stacking behaviour of the micelles as hexagonally packed lattice (i.e. Shifted layering in the form ABABAB… etc.). We note that there is a possibility that they are somehow fused or close to being fused. The details of this will be reviled by the electron density. The diagram on the right shows a bromide ion layer contributing to the lattice.* ***Bottom panel:*** *The diagram shows the stages of layering of 16-3-16 for form a crystal. AFM images of 16-3-16 in previous studies shows similarity to the proposed model* [114].

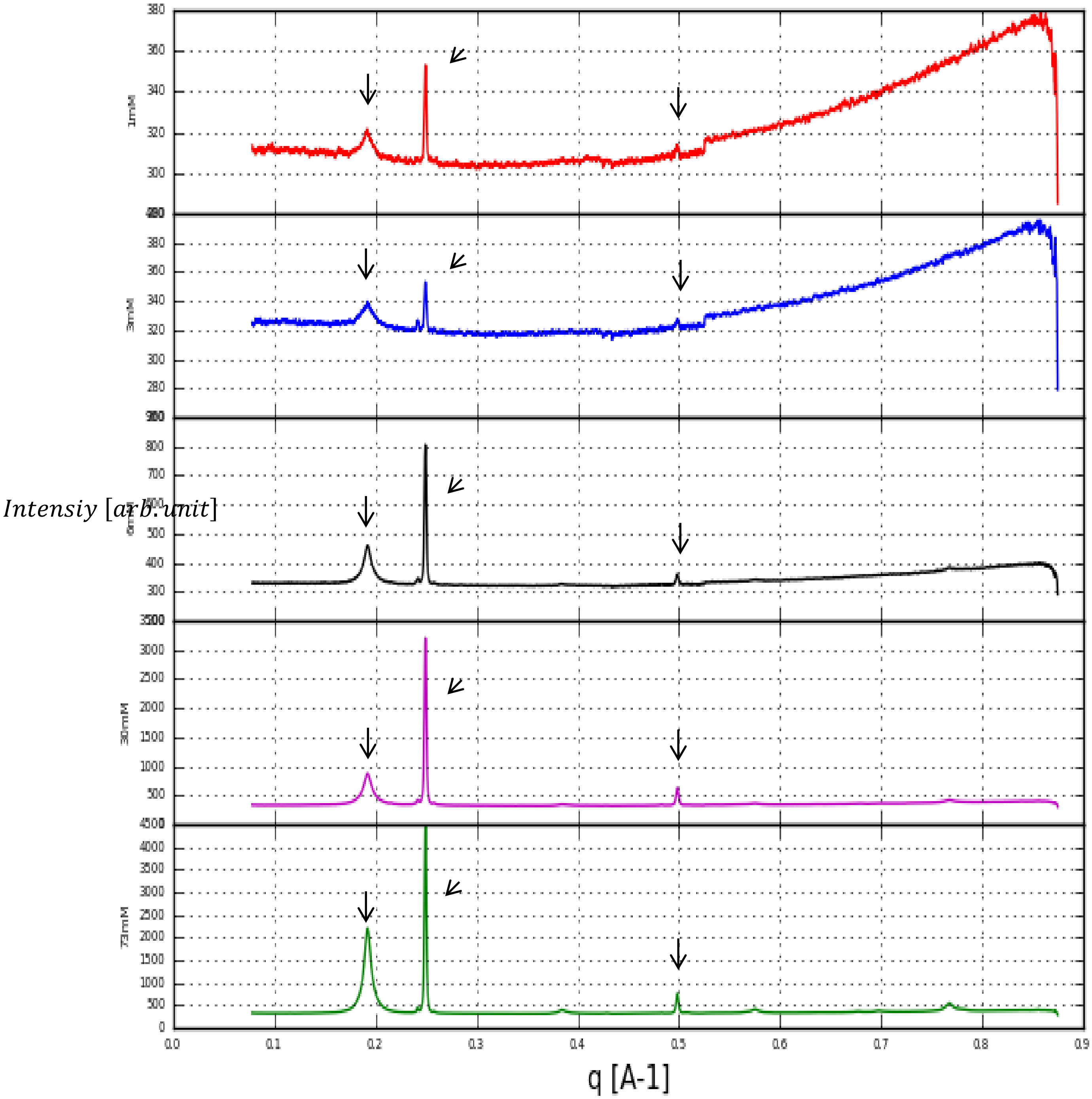

Figure 5.9. Scattering from 16-3-16 at different concentrations.

Figure shows the scattering pattern of gemini 16-3-16 at concentrations: (from top to bottom) 1mM, 3mM, 10mM, 30mM and 73mM. It is clear that the strongest peaks appear in all concentrations indicating the same structure is taken by the gemini in all concentrations.

Upon the addition of DNA (with 1:10 DNA: gemini charge ratio), the 16-3-16 pattern is still observed (from free micelles), and an extra peak appeared at a d-spacing = 48.84 Å (Figure 5.7). The new reflection/peak is due to DNA-DNA correlation and it indicates that a crystalline lattice is formed. The first reflection, which was referred to as the distance between the bromide ions, had shown reduction in intensity (compared to the remaining reflections). Additionally, we see a significant rise in the background. This can be interpreted as follows. As the DNA binds to the gemini, it replaces the bromide ions which would then become free in the solution and no longer part of the lattice and thus give rise to a higher background. It is generally well know that the counter ions release lead to a large entropic gain and thus considered as a major driving force for the assembly and interaction of the DNA with cationic lipids [10,70].

It could be therefore concluded that 16-3-16 forms discrete closely packed hexagonal lattice (that may be fused). The micelles are surrounded by bromide counter ions to neutralize their surface charge and reduce the repulsion between the layers. Upon DNA addition, the DNA replaces the bromide ions which are released into the solution, giving rise to a higher diffuse scattering background. This ion dispersion is thought to be an important deriving force of the assembly as it is accompanied by rise in entropy. The bromide ion release is also evident from the huge reduction of the intensity of the reflection that is related to bromide ions distances (much more than intensity changes in all other peaks).

5.4 Conclusions and future direction

In this chapter, the scattering patterns of 12-3-12, 12-7-12 and 16-3-16 gemini were studied along with their DNA-complexes. The 12-3-12 and 12-7-12 showed ellipsoidal to elongated worm-like micelles, whereas 16-3-16 showed a hexagonally close packed structure. As the gemini are mixed with the DNA, a disordered crystalline lattice is formed. The amount of free to bound gemini was found to be dependent on the charge ratio. These findings shed the light on the nature of the gemini-DNA interactions and illustrated a simple method for identifying the optimal charge ratios for different gemini surfactants.

Future studies will attempt to verify the initial conclusions presented in this chapter. The regarding the shapes of the 12-s-12 series micelles will be verified quantitatively by calculating the scattering patterns from analytical models. The parameters of the model are free parameters that can be obtained from the best fit. In addition, the reflections from 16-3-16 are indexed as a hexagonal packed lattice. This had worked well when the bromide ions considered as a separate lattice. Further attempts will be made to further improve the model and fully solving the structure by obtaining the electron density.

6 THE STRUCTURE OF GEMINI-BASED DNA DRUG DELIVERY SYSTEMS

6.1 Introduction

6.1.1 The nature of the self-assembled gemini-DNA based particles

The overall structures of the many macromolecular, nano-sized, self-assembling complexes such as cellular machineries, organelles and viruses are a consequence of a series of weak interactions that occur in a relatively ordered manner. These weak interactions lead to the formation of stable assemblies. These large assemblies are usually composed of smaller primary units such as proteins, DNA or lipid bilayers. In the majority of cases, the primary units form independently first to make specific structures. Thereafter, those units or components undergo a spontaneous assembly process, to form the larger complexes. Thus, the final assembled structure is influenced by the nature, order and rate of the events that it undergoes to be formed. Furthermore, it is obviously influenced by the environment in which these interactions occur and by the initial structure of its primary units. For example, previous studies showed that the observed enthalpies versus charge ratios profiles of the formed DNA-gemini surfactants complexes changes upon reversing the order of titration of the DNA and the surfactants [126].

The internal structural arrangement of the formulations including the dilute system/ nanoparticles that are composed of multiple components will heavily depend on the structure and structural properties of its components and the degree by which they interact with each other weather this interaction is spontaneous or induced by physical forces. Thus, there are three important factors to consider when mapping the internal structure of the multicomponent particles: (1) the structure and properties of the each component, (2) the degree of interaction between the components, (3) the applied external forces and physical methods used in the preparation of the particles.

Conventionally, the main deriving forces in the assembly are thought to be mainly the hydrophobic and Coulomb forces. However, external dispersive forces such as sonication maximize the mixing between the components and breakdown micro- and nano-clusters in the formulation [127,128]. This allows maximizing the distribution of the components amongst each other. Simple mixing on the other hand, does not breakdown the micro- and nano-clusters. Both spontaneous and energy-driven methodologies have advantages or disadvantages depending on the required properties. From structural point of view, naturally assembling composites that are not forced by physical means, represent a simplified form of many much more complex biological macromolecular assembles such as organelles or viruses. Hence, the study of such simplified analogous systems is of great interest. In this study, I report the effect of varying the charge ratio between DNA and the gemini surfactants on the structure of gemini surfactant based formulations designed for DNA transfection into cells. For the purpose of this discussion, I will refer to a crystal lattice of a specific type (example pure DPPC, DNA-gemini, etc.) i.e. a liquid single crystal as "domain".

6.2 Methods

6.2.1 Sample preparation

Gemini surfactants (12-3-12 and 16-3-16), plasmid DNA and helper neutral lipids 1,2-Dipalmitoyl-*sn*-glycero-3-phosphocholine (DPPC) and 1,2-Dioleyl-*sn*-glycero-phosphatidylethanolamine (DOPE) (both purchased from Avanti Polar Lipids, Alabaster, AL) were used to prepare the formulations. All formulations were prepared using sonication methods as described in previous studies [109]. The DNA plasmid pGTmCMV.IFN-GFP was used in the sample preparation.

For the 12-3-12 gemini, three different types of formulations were prepared; pure DPPC based, pure DOPE based and a 1:1 mixture of DOPE and DPPC. Each type was prepared in five different DNA: gemini surfactants charge ratios, specifically (1:20, 1:10, 1:5, 1:1 and 5:1). The charge ratios were calculated from the phosphate: nitrogen ratios (P/N). Each charge ratio was prepared in four different concentrations (1X, 2X, 10X and 25X), i.e. 1 fold, 2 fold, 10 fold and 25 fold concentrations, where 1X refers the most dilute concentration usually used in transfection [109]. Additionally, 16-3-16 gemini DOPE based formulations with 1:10 charge ratio at concentrations (1X, 2X, 10X and 25X) were used in this study. Samples were prepared by varying the DNA: gemini charge ratio, while the total neutral lipids: gemini molar ratio was kept constant at a molar ratio of 8.33:1. This constant gemini: neutral lipids ratio used in this study is similar to the standard 1:10 DNA: gemini charge ratio formulation used in previous studies [109].

The 1X 1:10 charge ratio was prepared in a similar way to the initial formulation used in previous studies, in which a 3 mM aqueous solution of gemini surfactants was mixed with aliquots of the plasmid DNA to reach the desired charge ratio. After the DNA-gemini complexes were mixed repeatedly by vortxing and incubated for 15 minutes, the neutral lipids were added [109]. The amounts of neutral lipids used were adapted to keep a constant total neutral lipids: gemini, using a 1 mM solution of neutral lipids vesicles for the 1X formulations. For higher concentrations, the initial concentrations of the components used in the preparation of the 1X were scaled 2, 10 and 25 folds in the 2X, 10X and 25X concentrations, respectively. All neutral lipids, despite the concentration, were suspended in the 9.25% isotonic sucrose.

6.2.2 The diffraction experiment : data collection, reduction and processing

The final SAXS/WAXS experiments were performed at the BL4-2 beamline at SSRL using energy of 11 keV and a sample to detector flight path of 1100 mm. All samples were loaded in 1.5 mm boron rich glass capillaries. Images were collected using 10-20 seconds exposure times. Several images per sample were taken. The semi-automated image reduction and processing was made by XPODS (see Chapter 4 for further details). Briefly, 1D scattering curves were obtained by radially averaging the intensities of the collected images. All diffraction patters were checked visually for radiation damage and the patterns that showed radiation damage were removed. If no signs of clear radiation damage observed, the processed curves referring to the same sample were averaged. Thereafter, all scattering curves were normalized, by exposure time, flux and were corrected for absorption. An automated peak search, peak profile fitting and peak intensity integration was performed.

6.2.3 Data interpretation

Fittings were performed following the model discussed in section 6.3.6. Optimal fitting was obtained by minimizing the Chi squared criterion. Python scripts were written to facilitate the process.

6.3 Results and discussion

6.3.1 The effect of the method of preparation on the structure of the complexes

In this study, formulations were prepared by the sonication of the neutral lipids to obtain vesicles (nano-micro sized depending on the concentration), which are then mixed with gemini-DNA complexes and then the formulations were left to self-assemble with the aid of simple mixing. Thus, if the gemini-DNA complex is strongly bound to each other on the molecular level, it is unlikely that they would separate after the neutral lipids are added. One could therefore expect that these gemini-DNA complexes would be embedded in the particles forming its core, which would be then surrounded by a matrix of neutral lipids. The reason why neutral lipids is likely to form a general matrix for the gemini-DNA complexes is that the amount of the neutral lipids used are much larger than that of the gemini-DNA complexes. Further, it was previously shown that the final particles takes a uniform size while the gemini-DNA complexes have much higher degree of polydispersity in size [109]. Thus, to be able to map the internal structure of the particles one would have to examine the structure of the individual components as well as the intermediate complexes and then compare or match such phases on the scattering pattern of the formulation.

As discussed in the previous chapter, the diffraction from all the DNA-gemini complexes shows a sharp Bragg's peak that is not observed in the diffraction patterns of any of the pure components alone, indicating that the complex is ordered. On the other hand, the neutral lipid matrix is liquid crystalline in nature with relatively high order in compared and thus also gives rise to sharp diffraction peaks. As will be discussed in the sections below, the diffraction patterns of the final assemblies showed a remaining signature of the diffraction peaks of both the DNA-complexes phase and the lipid matrix phase as well as other phases that will be discussed. The incorporation of the DNA-gemini complexes was evident through the induced disorder in the neutral lipid matrix as well as the spontaneous strong interaction between the gemini and the neutral lipids. Thus, the formulation can be understood in the form of a crystalline domain embedded inside another crystalline domain. Effectively, we have a mixture of components that assemble together spontaneously in a specific order to form the final lipoplex. The nucleus or nuclei of the lipoplex represents the tightly packed DNA by the gemini surfactants. This nucleus is embedded in a matrix of neutral lipids. The latter was the basis upon which a fitting model was developed which was used to analyse the scattering patterns of the formulations.

As mentioned earlier, the preparation of the DNA-gemini based complexes that were used in this study were prepared by simple mixing of the initial components (DNA and gemini) that were initially prepared separately, and then were left to self-assemble into a complex. The formed complexes were then mixed with the neutral lipids liposomes. It should be noted that the method used here depends mainly on a spontaneous assembly process. Only an incubation period and perhaps simple shaking is needed. It does not depend on using physical methods as sonication to enforce the homogenization and interaction process. It is not therefore expected that the gemini micelles would break down, but rather, they would stay intact and bind to the DNA in an arrangement that maximizes the attraction forces between them. The formed DNA-gemini complexes were then expected to get incorporated into the neutral lipids liposomes. This differs from other preparation methods that had been reported in other studies [129,130]. In the latter, the gemini surfactants and the neutral lipids are prepared simultaneously allowing the even distribution of the cationic charge within the neutral lipid bilayer, which would lead to a condensate that is less diverse.

6.3.2 The Structure of Neutral Lipids

6.3.2.1 DPPC

The DPPC showed the well-known lamellar structure (Figure 6.1) [131,132] as determined from the ratios between the positions of the peaks which was equal to 1: 2: 3... etc. (Table 6.1). The structure of DPPC at 25 mM shows a lamellar phase having multi-lamellar vesicles. This can be seen from the sharpness of the peaks. Lower concentrations show gradual declination of the crystallinity due to the reduction of the size of the lipid domains, thus converting from multi-lamellar vesicles to oligo-lamellar vesicles. The sizes of the vesicles are reduce due to dilution effects and due to mechanical and physical forces applied on them (e.g. sonication, heat, addition of glass beads etc.).

The d-spacing of the first peak (lattice parameter or lamellar repeat) of the 25 mM concentration was equal to 64.85 Å which refers to *Lβ′* DPPC phase (gel phase), which is the expected phase of the fully hydrated DPPC at room temperature [131]. On the contrary, the lattice parameter of nano-particle (dilute preparations) was found to be 79.36 Å which is even larger than lamellar repeat of the *Pβ′* phase (ripple phase) which has been reported to be 70.2 Å [133] and 72.0 Å [134] in different studies. The latter phase, is usually seen at high temperatures (between 34ºC-41.3ºC) [133]. Thus, it is not surprising to be seen also small particles, especially in sucrose solution.

Indeed, the mechanical forces exerted by the glass beads which are used to reduce the vesicle size, as well as the high dilution along with the osmotic pressure of the dilute sucrose solution, are all factors that may aid in the swelling of the bilayers. As seen from the scattering patterns, the 25X and 10X concentrations, which make larger domains, share a very similar neutral lipid structure. While the 1X and 2X are similar to each other but different from the former two in terms of d-spacing and the degree of disorder. Further, the effect of filtration is shown in the same figure. One can realize that the sharpness of the peaks is increased upon filtration. This is due to the reduction of the size-polydispersity after filtration.

1 mM		**2 mM**		**25 mM**		***hkl***
d-spacing (Å)	**q ($Å^{-1}$)**	**d-spacing (Å)**	**q ($Å^{-1}$)**	**d-spacing (Å)**	**q ($Å^{-1}$)**	
79.36	0.0792	79.36	0.0792	0.6485	0.0969	001
-	-	40.51	0.1551	0.3269	0.1922	002
-	-	-	-	0.2185	0.2876	003

Table 6.1. Peak positions of DPPC.

The table shows the peak positions and the hkl indexing of DPPC at concentrations 1 mM, 2 mM and 25 mM.

6.3.2.2 DOPE

The scattering pattern from DOPE vesicles have shown Bragg's peaks at positions (Table 6.2) with a ratio of $1:\sqrt{3}:\sqrt{4}$ (*graphs not shown*) which refers to the well know inverted hexagonal structure of DOPE [55].

1 mM		**2 mM**		**10 mM**		**25 mM**		***hkl***
d-spacing (Å)	**q ($Å^{-1}$)**	**d-spacing (Å)**	**q ($Å^{-1}$)**	**d-spacing (Å)**	**q ($Å^{-1}$)**	**d-spacing (Å)**	**q ($Å^{-1}$)**	

57.57	0.1091	58.48	0.1074	62.44	0.1006	63.73	0.0986	100
-	-	33.58	0.1871	36.36	0.1728	36.72	0.1711	110
-	-	29.45	0.2133	31.51	0.1993	31.51	0.1990	200

Table 6.2. Peak positions of DOPE.

The table shows the peak positions and the hkl indexing of DOPE at concentrations 1 mM, 2 mM, 10 mM and 25 mM.

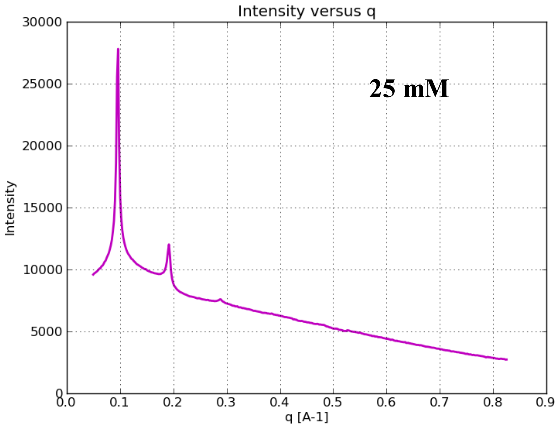

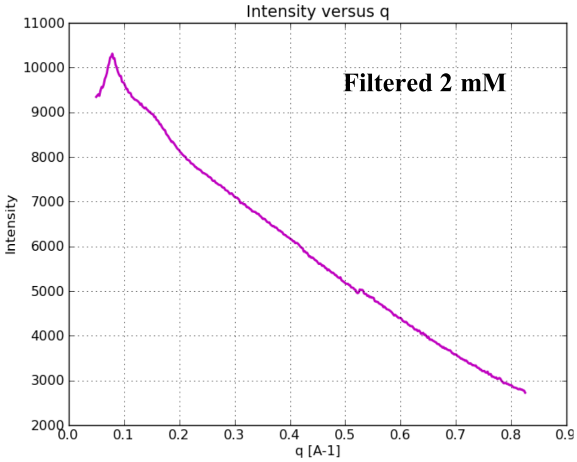

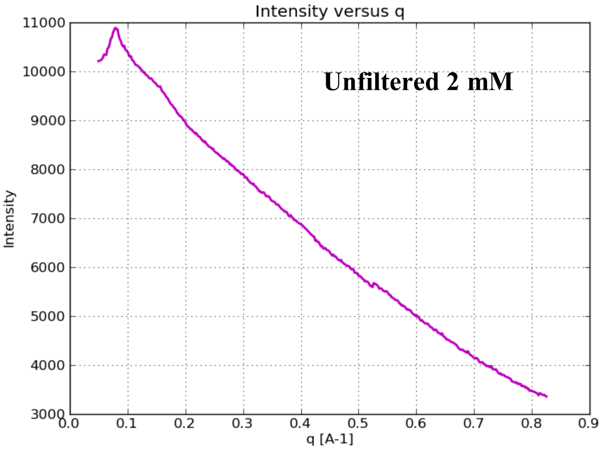

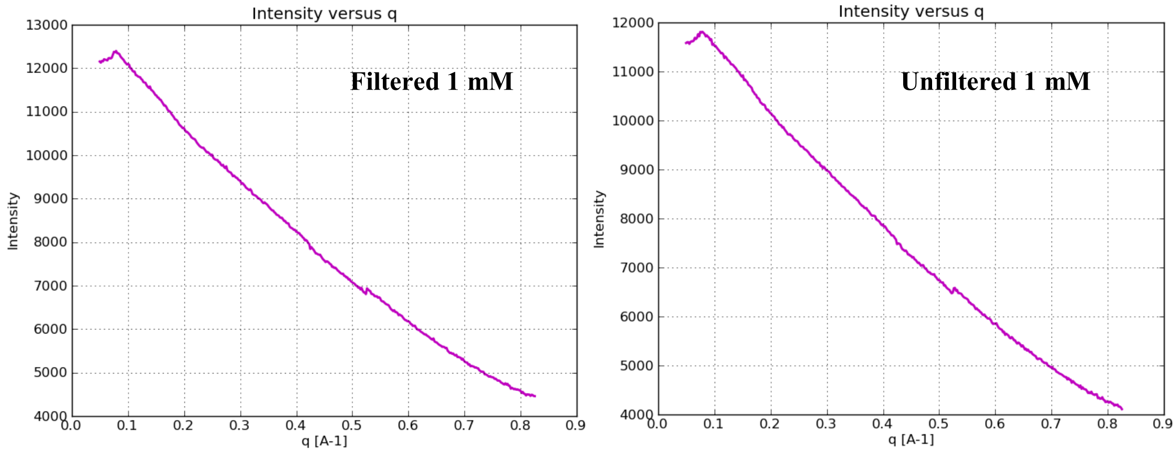

Figure 6.1. X-ray diffraction pattern of DPPC in sucrose with water subtracted as a background at different concentrations.

6.3.3 The effect of varying the DNA: 12-3-12 gemini charge ratio

In all formulations (Figure 6.2, Figure 6.7 and Figure 6.6), the origins of the main diffraction peaks was easily identified, especially in the cases of 1:1 DNA: gemini surfactants charge ratio. In most cases, the diffraction peaks of the neutral lipids were observed. In addition, the DNA-DNA correlation peak from the DNA-gemini complexes was identified, or at least a remaining evidence of its existence was seen. It was found however, that there are changes that occur as the charge ratio deviates from 1:1. These effects are discussed below. The scattering patterns shown here are a selected subset in order to represent the general trends. A full list of the recorded patterns summary graphs are shown in Appendix B.

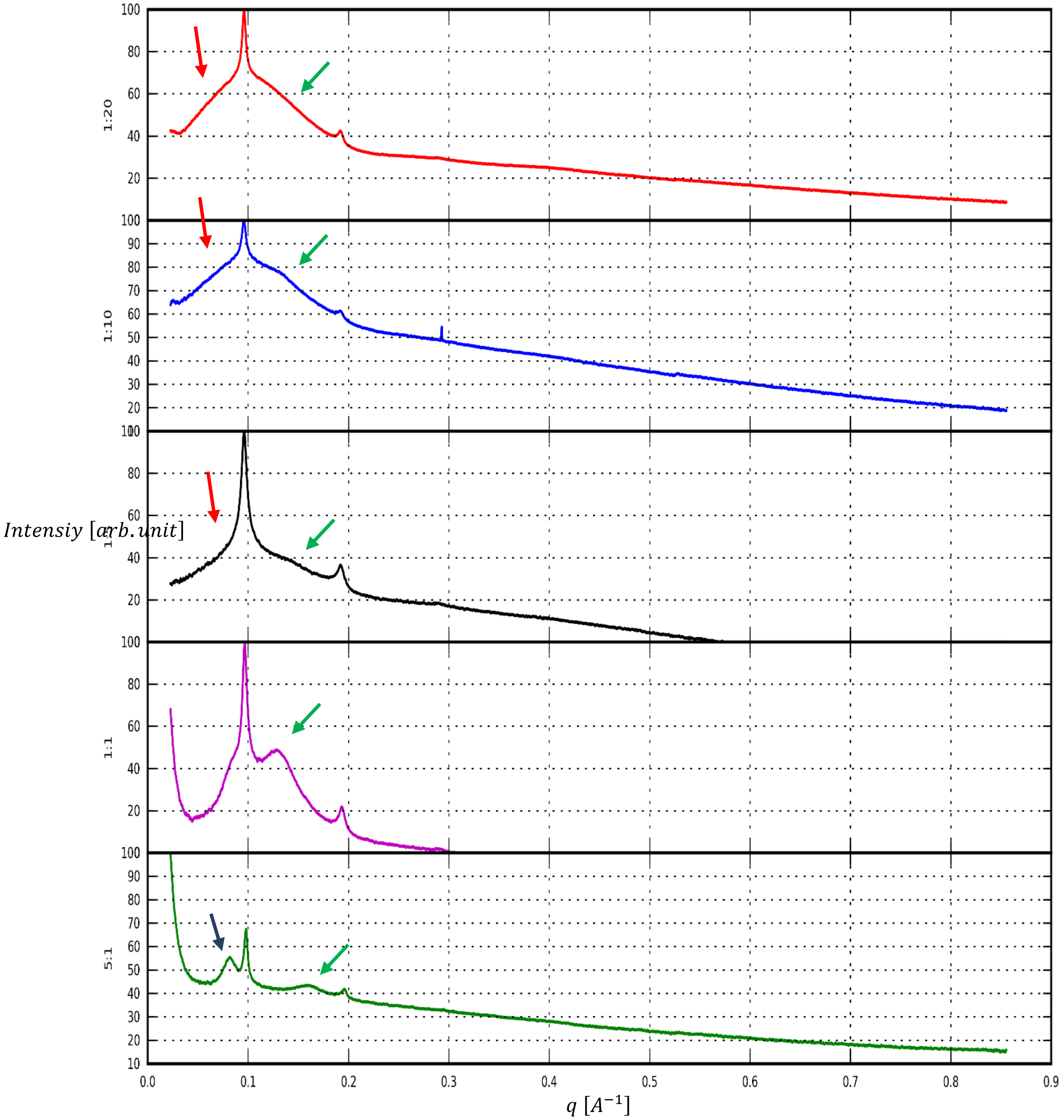

Figure 6.2. Gemini-DNA-DPPC complexes.

The figure shows the scattering patterns from 12-3-12 gemini-DNA-DPPC complexes with different DNA: gemini charge ratios ranging from 5:1 to 1:20 after background subtraction (water and capillary). The red, blue and green arrows point to excess gemini-DPPC, DNA-DPPC, and DNA-gemini complexes respectively.

In the case of 12-3-12 gemini-DNA-DPPC complexes (Figure 6.2 and Figure 6.3), the scattering patterns showed that in the presence of excess DNA, DNA interacts with DPPC to form a lamellar columnar phase (L_c phase, Figure 6.4) showing a peak at 72.8 Å. This is mainly seen at high concentrations. As the concentrations decrease to 2 mM DPPC (2X) and 1 mM (1X), the L_c peak disappears indicating this incorporation is minimized. This is likely due to the decrease of the size of the domains to only a few lamellae i.e. oligo-lamellar vesicles (OLV). Indeed, the incorporation of DNA with neutral lipids is much less compared to the incorporation with charged lipids as the former is only seen in the presence of excess DNA (i.e. at high DNA: gemini charge ratio). The interaction between DNA and DPPC is usually mediated by divalent ions [121,133,135].

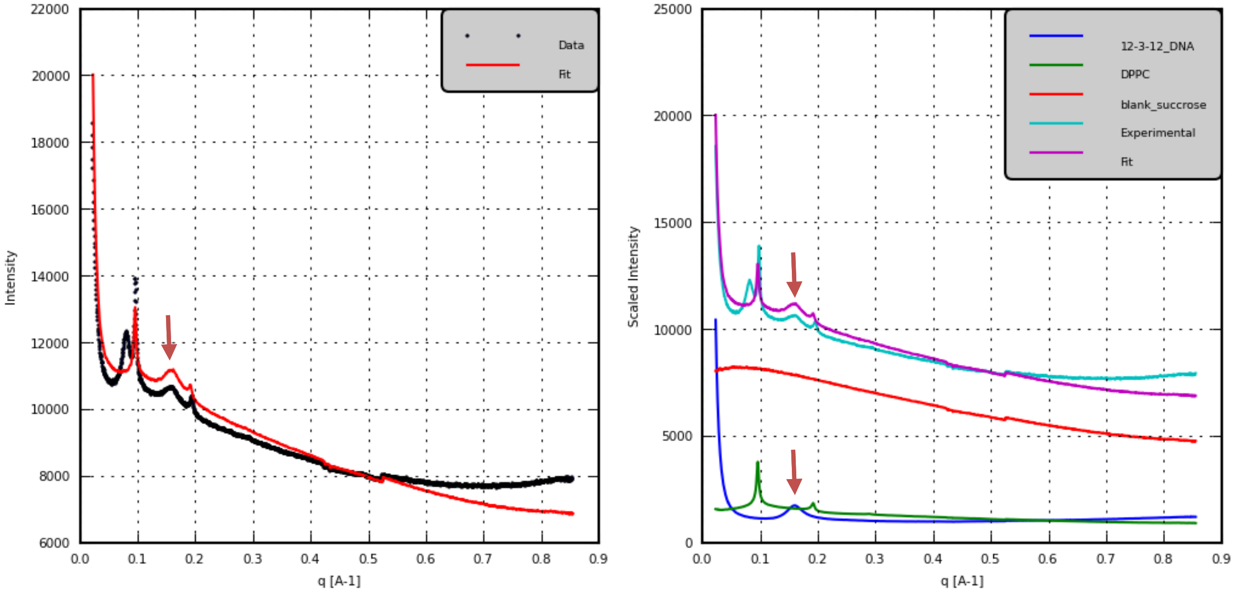

Figure 6.3. Effect of DPPC on DNA-DNA correlation peak at high DNA: gemini charge ratio.

The figure shows DNA-12-3-12 gemini-DPPC formulation (25X) with DNA:gemini 5:1 charge ratio. The arrows are pointing to the DNA-DNA correlation peak which is observed both before and after the addition of the neutral lipids.

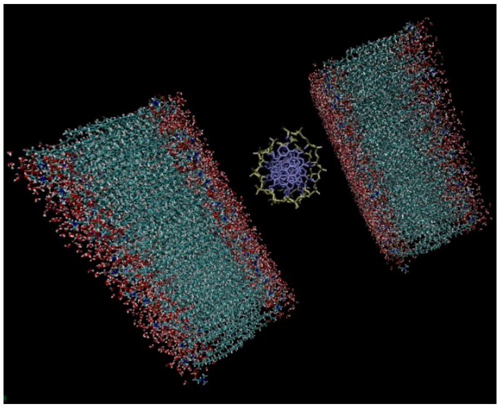

Figure 6.4. DNA-DPPC Lc phase.

Figure shows a schematic diagram of a slice through the DNA-DPPC Lc phase formed by the neutral lipids-DNA interactions, seen in micron sized domains.

Although divalent ions were not directly added, traces of divalent ions from the DNA buffer used in the DNA isolation or traces of lead (Pb^{+2}) ions present in the sucrose solution (Sigma Aldrich Inc. sucrose product manual) may have mediated such interaction, especially that the DNA concentration is low compared to the neutral lipids. This interaction is much more likely to occur if the domain sizes are large and the solution is sufficiently dense (i.e. at higher concentrations) to enforce the large DNA into the vesicles. It does not seem that this enforcement occurs when domains are reduced to a small sizes (dilute regimen). This is expected as in the latter case, the DNA plasmid molecules may be larger or equal to the size of lipid domains.

Previously, it has been reported that at a high concentration of plasmid DNA, a plasmid-plasmid stacking that leads to the formation of a hexagonal lattice may be seen. The lattice parameter for such structure have been reported to be 170 Å, which its corresponding d-spacing is much larger than that observed here [136]. Thus, this excludes the possibility that the observed peak is a plasmid-plasmid supercoiled correlation. The d-spacing for the L_c in this study was found to be slightly variable (74, 77 and 72 Å) at different concentrations. Considering the ~ 37 Å normal thickness of the DPPC bilayer [132], then the inter-bilayer d_{water} is approximately 35-40 Å. This is generally close but a little smaller compared to the L_c phase of DPPC reported in previous studies, which was 79 or 80 Å (d_{water} = 42-43 Å) [133]. The latter assembly depended on divalent ions only without the presence of any cationic lipids, and hence the larger d_{water}. Whereas the d_{water} previously reported in the presence of charged lipids seem to be much smaller example 26-30 Å (example see review [137]).

Therefore, in general, one may conclude that inter-bilayer water region in the Lc phase is dependent on the charge density of the membrane. It may also be influenced by other factors such as degree of hydration. Thus, the smaller d-spacing observed here may be an indicator of that there is a degree of mixing of small amount of gemini molecules remaining free and unbound to the DNA with the DPPC lipid bilayers leading to a mildly positively charged membrane surface at certain regions.

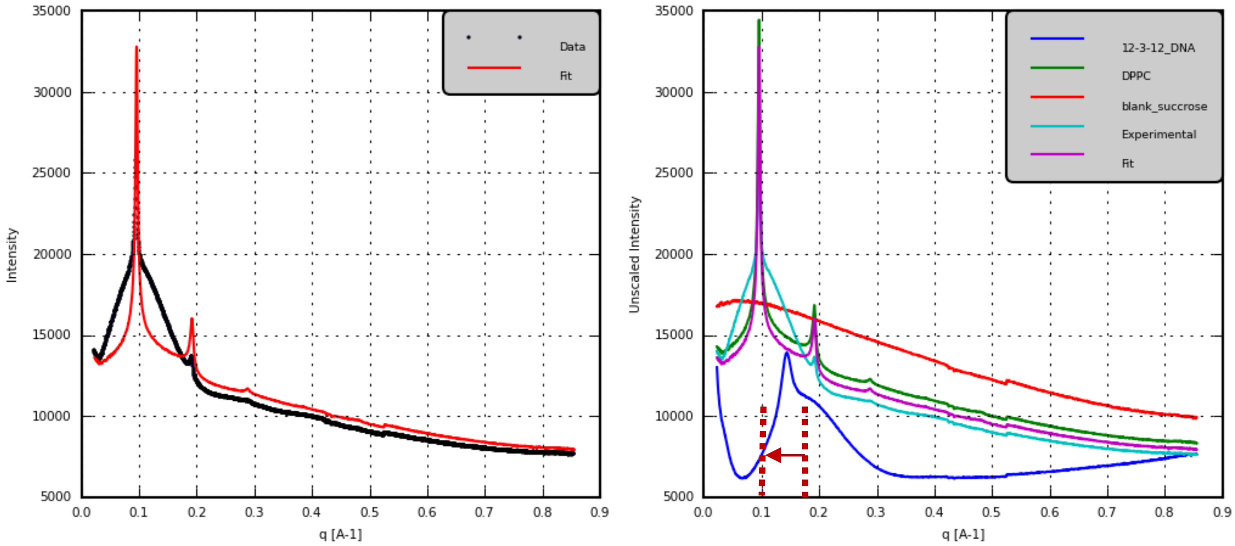

Figure 6.5. Effect of DPPC on DNA-DNA correlation peak at low DNA: gemini charge ratio.

The figure shows DNA-12-3-12 gemini-DPPC formulation (25X) with DNA:gemini of 1:20 charge ratio. The arrow and dotted lines are showing the shift of the scattering lobe from free micelles to a lower q (see text for details).

In the case of excess gemini, a sign of DPPC-gemini interaction was observed. The latter interaction, is evident by a Gaussian shape lobe formed upon the increase of the gemini content, the integral of this lobe increases as a function of the DNA: gemini charge ratio decreases. On the other hand, the sign of the free gemini that is seen in the DNA-gemini complexes had disappeared and was shifted to a smaller q by ~ 35-40 Å (Figure 6.5). This difference which likely to be related to the increase of the size of the micelles, is approximately equal to the natural thickness of a single DPPC bilayer. Thus, it is likely that micelles had undergone an increase in thickness, possibly by an average of ~ 37 Å due to the formation of a bilayer around the micelles (Figure 6.8).

It was realized however, that at a DNA: gemini charge ratios starting from 1:1 in particular and specifically those with higher gemini surfactants content, there is a shift in the DNA correlation peak (of the DNA-gemini complex) towards a lower *q* by ~ 5.5 Å (from 43.5 to 48.9 Å). This may be due to a DNA-gemini-DPPC interaction. Thus, when free/excess gemini exists, they tend to cover the DNA-gemini clusters by binding to the free DNA surface allowing a direct DPPC interaction with the surface of these clusters (and subsequently leading to the existence of larger size repeating units). Whereas, in the presence of high amount of DNA, the opposite occur, where the DNA is incorporated excessively in the DNA-gemini clusters leading to an overall negatively charged surface and a tightly packed cluster. This negatively charged surface, as well as the tight packing of DNA-gemini clusters, are factors that would hinder the DPPC interaction with these clusters.

Thus, it is likely that the presence of excess gemini surfactants on the surface of the DNA-gemini clusters/complexes allows the attraction of the neutral lipids and thus incorporation of the complexes into the nanosized DPPC vesicles, which would be much weaker in the case of excess DNA. On the other hand, as the free gemini surfactants increase, it is expected that the toxic effect on the cell membrane increases due to the strong interaction with the free highly charged micelles with the cell membrane. It follows, that the design of the gemini based particles for transfection purpose should consider a balance between both aspects; the incorporation into the neutral lipid matrix and toxicity. The free/excess DNA and gemini concentrations are at a minimal at the charge ratio 1:1 and DNA-gemini complexes DNA-DNA correlation peak is more defined (higher relative intensity) compared to other charge ratios. It could be therefore concluded that the 1:1 DNA: gemini charge ratio is close to the optimal binding charge ratio for the 12-3-12 gemini. However, a slightly higher percent of gemini might be necessary to induce optimal incorporation of the complexes into the neutral lipids.

At high DNA content, 5:1 DNA: gemini charge ratio, the DNA correlation peak appeared at a smaller d-spacing, possibly due to a newly formed hexagonal lattice. The smaller unit cell suggested that the DNA-gemini complex remained unchanged and did not show signs of interactions with the neutral lipids due to the overall neutral or negative charge of the complex and thus does not attract the negatively charged neutral lipids. In all charge ratios, the DNA-DNA correlation peak remains either directly seen or in the case of high gemini surfactants content its signature can be identified through the asymmetry of the Gaussian elevation.

The lamellar system was found to dominate the scattering patterns of gemini-DNA formulations prepared with a DOPE-DPPC mixture (Figure 6.6). These formulations showed a similar behavior to the formulations prepared with pure DPPC. The only difference is that in case of the presence of both lipids, there some weak signs of phase separation between the two neutral lipids which is indicated by the splitting of the first peak in dilute formulations (Appendix B). This is expected as it is mainly a mixture. In fact, it was thought that this phase separation would be observed even more clearly. Thus, in general, the DPPC and DOPE lipids seem to have the natural tendency to mix to a high degree. The difficulty however is to choose the correct ratio between them that allows their optimal incorporation into one homogenous phase. It has been reported that phase separation occurs more frequently with lipids that are different in their tail structure [121,138]. This is generally comes as part of growing area of lipid research and which was subject of many studies in the past decade, known as lipid rafts [139–142]. It has been previously reported that local clustering resulting from phase separation is not uncommon in lipid mixtures. Such arrangement is thought to result in local disordered regions. This local disorder is also seen in the case of embedded exogenous molecules in the membrane such as proteins. It is thought that lipid rafts in general plays important roles in the regulation of the cell membrane functions. X-ray diffraction scattering has been used to study lipid rafts [143,144].

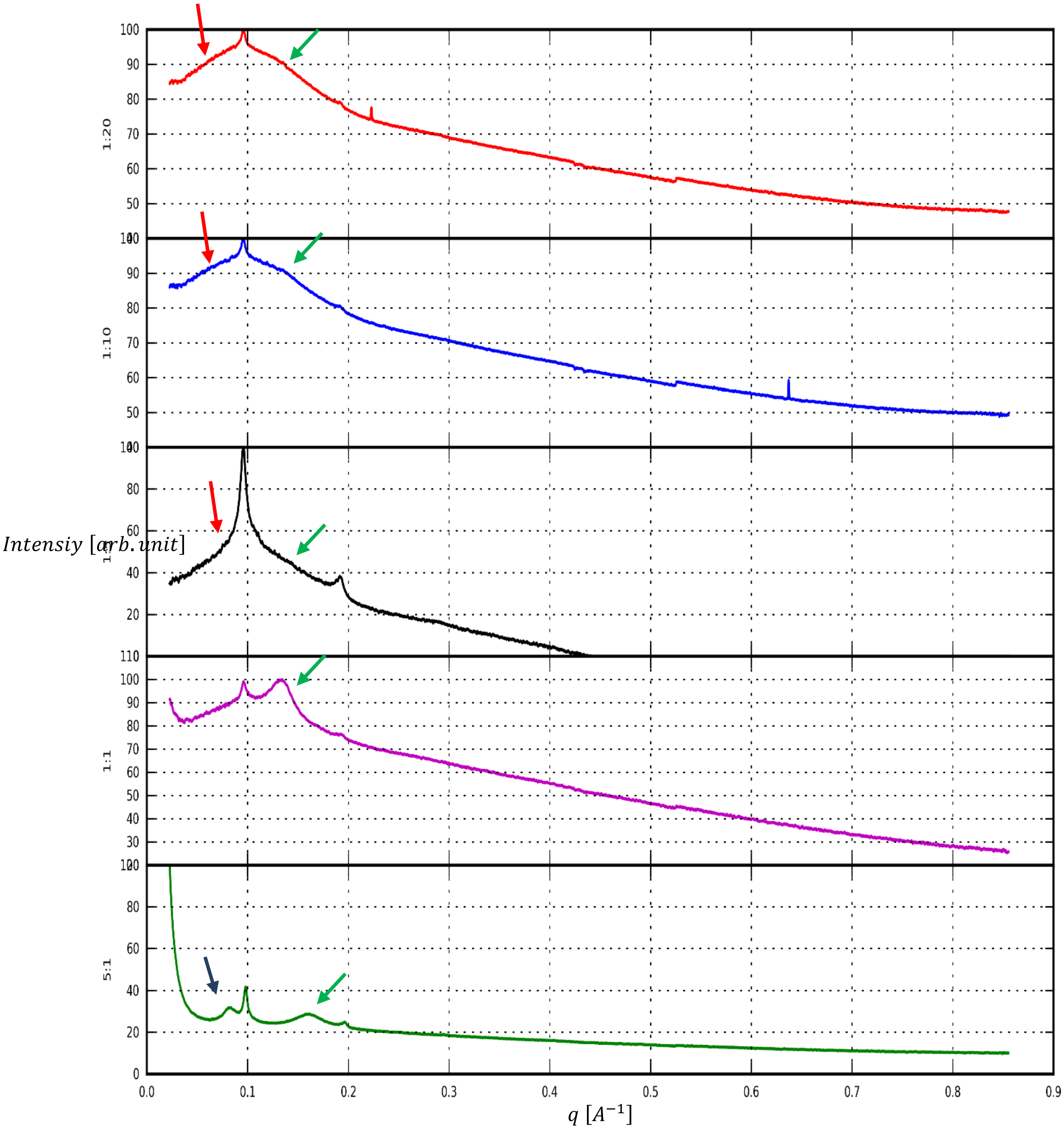

Figure 6.6. Gemini-DNA-DOPE-DPPC complexes.

The figure shows the scattering patterns from 12-3-12 gemini-DNA-DOPE-DPPC complexes (25X) with different DNA:gemini charge ratios ranging from 5:1 to 1:20 after water background subtraction. The red, blue and green arrows point to excess gemini-DPPC, DNA-DPPC, and neutral DNA-gemini complexes respectively.

The cell membrane contains both lipids, where DOPE is thought to dominate the internal leaflet of the membrane and DPPC dominate the external leaflet of the cell membrane [145]. The DPPC percent in the cell membrane is more than the DOPE and both components are stabilized by a small percent of cholesterol, which is known to induce stiffness of the lipid membranes [146]. Thus, using a ratio of neutral lipids that are similar to the cell membrane can be perhaps a plausible ratio to use in the preparation of our DNA delivery system.

In the case of gemini-DNA formulations prepared with pure DOPE (Figure 6.7), at high DNA content the formation of an inverted hexagonal columnar phase (H_{IIc} phase) would lead to a slight reduction of the water lumen if occupied by a single DNA strand [147] and would probably increase if occupied by a double strand. However, due to the change of the lattice parameter which is induced by other factors as the osmotic pressure and due to the high degree of disorder, it is rather difficult to assure that there is a H_{IIc} phase formed in excess DNA. Further, DOPE-DNA H_{IIc} phase is known to form much weaker and heavily influenced by the presence of divalent ions and may need the incubation of the samples for to be fully developed [147]. Moreover, since the lattice parameter fluctuations are also seen if with pure gemini only without DNA, then we cannot claim/depend on this change only as an evidence of H_{IIc} phase formation. Additionally, since the DNA in total is little, then one should see a peak split in the hexagonal phase (two phases) if the H_{IIc} phase exist. Thus, a H_{IIc} phase formation is rather unlikely or if formed would be in very small amounts and probably in the case of high concentrations only.

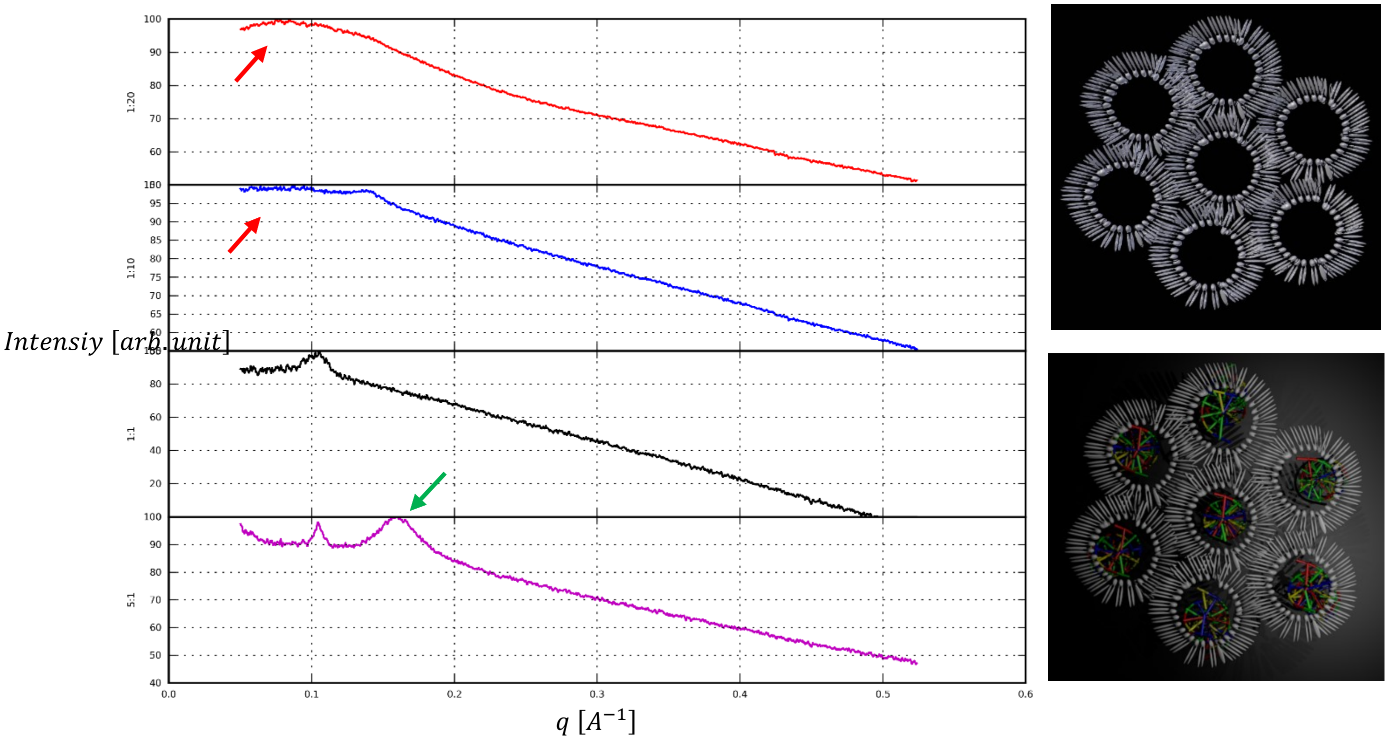

Figure 6.7. Gemini-DNA-DOPE complexes.

The figure shows the scattering patterns from 12-3-12 gemini-DNA-DOPE complexes with different DNA: gemini charge ratios from 5:1 to 1:20 after water subtraction. The red and green arrows are pointing point to excess gemini-DOPE and neutral DNA-gemini complexes respectively. The side panel on the right are schematic diagrams of the H_{II} *and* H_{IIc} *phases of DOPE and DOPE-DNA, respectively.*

However, in the case of DOPE based formulation prepared with excess gemini, a gemini-DOPE interaction was seen. This would have only occurred if free unbound gemini was available in the solution. The latter interaction resulted in the increase of the diffuse scattering that, in some cases, completely covered the Bragg's peaks (as indicated by arrows on Figure 6.7). This effect was also seen in the DOPE-gemini scattering patterns (without DNA). The formed lobes seem to be of lower relative intensity compared to that of the ones formed with DPPC (Figure 6.5). This is expected as the density/contrast is different from the bilayer that is expected to form around the micelles in the case of DPPC and the inverted monolayer that is expected to be formed in the case of DOPE. Since the degree of contribution of the gemini-DOPE interaction increase with the increase of the pure gemini surfactants, then one could conclude that the incorporation of the DNA complexes increases if the neutral complexes were overloaded with excess free gemini (e.g. bound to its surface).

6.3.4 Neutral lipids-gemini interactions

As discussed above, the DOPE gemini patterns cannot be fully explained as a mixture or a linear combination of multiple crystal patterns, indicating that they strongly interact and form what could be considered as a new phase. As mentioned previously, it is realized that this interaction leads to a lattice parameter change and also leads to the increase of diffuse scattering, which gradually smears out the Bragg's peaks of the DOPE lipids as the free gemini concentration increases relative the DOPE. As discussed above, this may indicate that as the gemini concentration increases the incorporation of the DNA-gemini complexes increases. This is because the DNA-gemini complexes will also carry excess gemini which would allow it to easily incorporate into the neutral lipid liposomes.

The relative broadening of the DOPE peaks could be due to the increase of disorder, (i.e. stacking faults) which would increase if the charged gemini is lodged into the water channels of the DOPE cylinders. This is in addition to the diffuse scattering from the thickened ellipsoidal gemini as it is surrounded by a monolayer of DOPE molecules (Figure 6.8). In general, the interaction with the DPPC apparently seems to be much stronger than DOPE. This may be due to the fact that, and as a result of the lamellar structure of DPPC, the polar heads are more exposed in DPPC than in DOPE. Further, the lamellar nature of the DPPC facilitates the incorporation of small clusters of molecules.

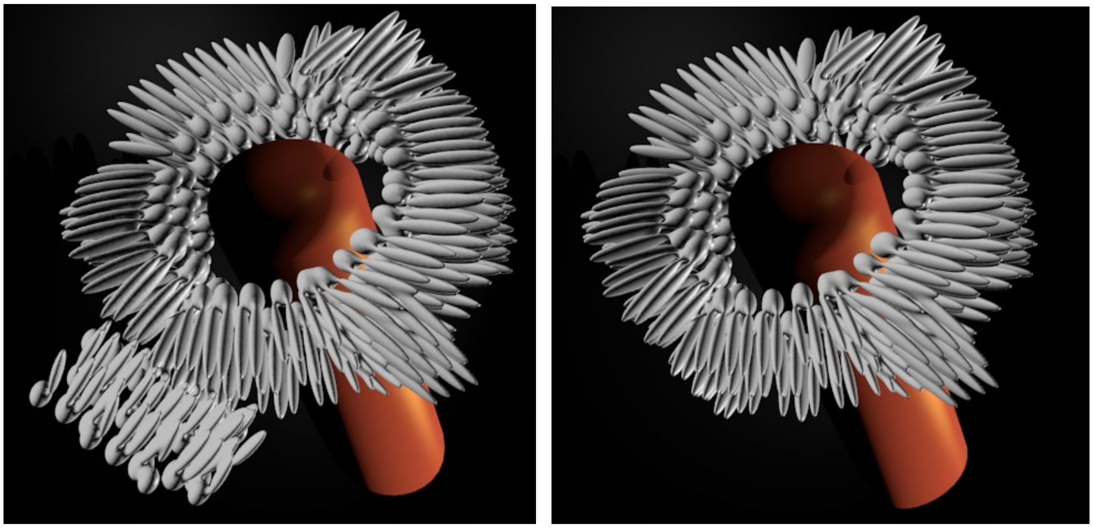

Figure 6.8. Micelle-neutral lipids formed complexes.

The figure shows a cartoon of the proposed gemini surfactant micelle-neutral lipids formed complexes. Since it is a simple mixture, the micelles stay intact, and it grows in diameter by a double (in case of DPPC) or an inverted single layer (in the case of DOPE). The charge induced repulsion force between the amino heads are shielded by a layer of bromide ions.

The possible models mentioned above, and schematically shown in Figure 6.8, represent a form of phase separation. In the latter, each of the two components maintains its core structure though an interaction occurs. Another possibility is that the neutral lipid molecules get incorporated into the micelles [148]. A third model is that the gemini molecules become distributed into the bilayers. The latter two models represent a form of phase incorporation to make one new phase. The formation of these models however require the breakdown of the gemini clusters. As discussed in section (6.3.1), the method used to prepare the complexes in this study does not involve using physical forces to induce full mixing, and hence the incorporation of the two molecules into one phase is not expected. The phenomenon of phase separation (lipid polymorphism) has been commonly reported in literature between both the similar or different molecules [129,140,149,150]. In addition to global phase separation, the so called lipid rafts, is had been also reported numerously [151,152]. In the latter, the lateral symmetry of lipid membranes are perturbed by another phase/cluster (i.e. a phase separation on a micro-scale). This was demonstrated both experimentally [151] and theoretically [153].

On the molecular level, it is not yet clear however how exactly this interaction occurs. One possibility is that it occurs due to the long range attraction force between the divalent negatively charged oxygen on the phosphate group on one neutral lipid molecule and the two positively charged nitrogen atoms of the gemini heads, and at the same time, the positively charged amino groups on both molecules are partially neutralized or stabilized by having the bromide ions in between as a shield between the two positively charged heads, and thus reducing the repulsion forces between them. Future investigations may suggest a role played by ions in shielding the repulsion forces between the two similarly charged groups. In fact, it has been shown that cations can mediate the complexation of the negatively charged DNA with anionic lipids [154].

6.3.5 Overall lamellar versus hexagonal lattice

It is apparent that lamellar systems tends to retain its structure more that the hexagonal system while still shows strong interaction with the gemini surfactants or their DNA complexes. This is evident by the fact that only small differences are observed between the DPPC peaks profiles in the formulations scattering patterns compared to their corresponding pure DPPC (Figure 6.2), whereas larger changes are observed in the peaks profiles of DOPE in the formulations scattering patterns compared their corresponding pure DOPE (Figure 6.7). This is expected as lamellar systems can act as a container for other components. The flexibility of the bilayer which is manifested in the increase in the bending of the membranes as a response to mechanical stress as well as the fluctuation in the distances between subsequent bilayers makes lamellar systems a suitable molecular container. On the other hand, DOPE which takes a hexagonal lattice is known to induce fusion. However it seems to exhibits much less flexibility as its crystallinity declines much more than DPPC. Thus, a hybrid system may be a convenient choice to enable to benefit from the properties of both lipids.

6.3.6 The overall scattering model

6.3.6.1 Sucrose and water exclusion (solvent exclusion)

Since the formulations are prepared in a sucrose solution, then the total background is the scattering from the sucrose solution alone with sample holder (glass capillary). One problem however is that the scattering from the sucrose solution is sometimes higher than the scattering patterns leading to negative intensities, even though the features of the curves, sometimes including parts of the Bragg's peaks, can be still seen in the subtracted intensity. For example, for some samples even though lobes from the scattering of the gemini or from the dilute neutral lipids are seen, the intensity of the pattern is lower than that of the total background. The latter is due to the fact that lipid molecules replace a significant portion of the water and sucrose. Thus, the 'effective background' in the sample is less than the one measured from the pure sucrose solution. This excluded volume from the background has been always a difficulty in protein SAXS. In order to correctly calculate the scattering pattern from the atomic coordinates of a protein in solution, the excluded electron density volume of the solvent (which is approximately equivalent to the volume of the protein in the solution) is usually taken into account by one way or another. A number of methods have been successfully used and implemented in several software [105,106,155,156]. The need for the scaling of the background has also been discussed in previous work on lipids [19]. Furthermore, sugars was shown to have a mild effect on the structure and the scattering pattern of lipids, and the possibility of its exclusion by the bilayers was shown to be not unlikely [157–160]. Adding to the complexity, when the components of formulations are mixed together, sucrose solution is diluted in a different degree from one sample to another.

Assuming that the remaining effective background (sucrose and water) still retains the same scattering pattern as the bulk measured background, but just less in volume, then one could consider the difference between the effective background and the measured background as a deference in the concentration only. In other words, they differ in the irradiated volume or the number density of the molecules. Therefore, one could simply scale the background down to reach a correct level. Alternatively, one would subtract the excluded volume of the background by the lipid bilayers and the formed complexes as it is usually done in the calculation of the solution scattering profiles of proteins. With a mixture of this complexity however, the exact excluded volume is very difficult to be exactly determined. Thus, scaling the background may be a more convenient choice in this particular case, and therefore the background scaling factor was made a fitting parameter.

In principle, the scattering from the sucrose solution is equal to the sum of the scattering from water, holder and sucrose and thus can be described by

$$I_{bk} = v_{sucrose} I_{sucrose} + v_{water} I_{water} + I_{glass\ capillary}$$

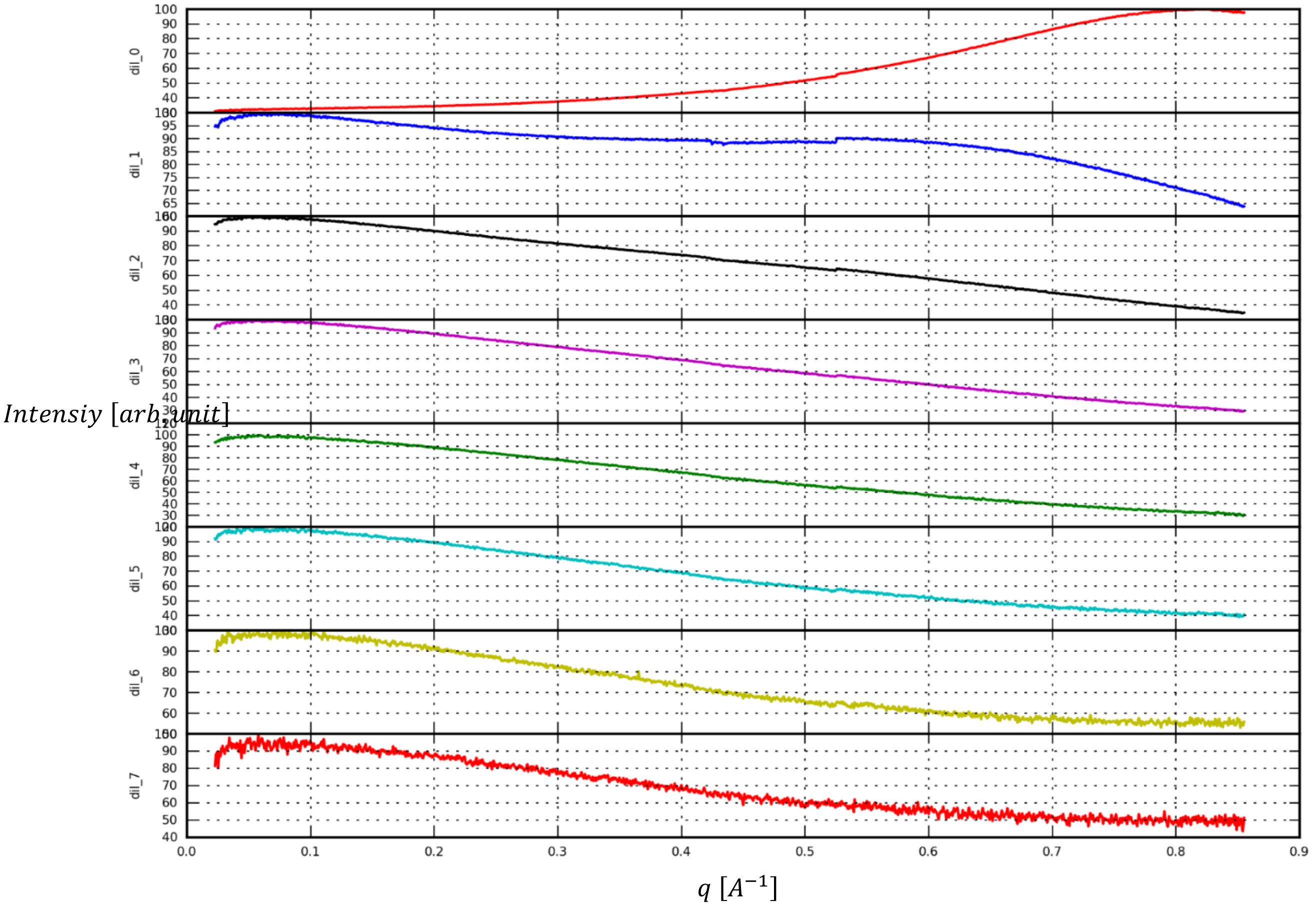

Figure 6.9. Scattering from the sucrose background.

The figure show a series of sucrose solution starting from a saturated solution and diluted gradually with 10 fold serial dilution. The scattering patterns show that sucrose exhibits same structure until very high concentrations where evidence of a structure factor begin to appear. Interestingly, it is evident that samples in dilute sucrose are influenced at the low angle part of the scattering pattern. On the other hand, at sufficiently high sucrose concentrations, the high resolution data is likely to be immersed by the sucrose background, while the low resolution data is likely to show much improved contrast.

The first two components (the water and sucrose) are excluded by the lipid and DNA molecules, but generally the sucrose is much more effective. Thus, one could try to subtract pure water and then scale the sucrose only and its scaling factor as a fitting parameter. However, it was found that in the very dilute samples this still may lead to negatives and generally lead to lower quality fits. Consequently, it was most convenient to scale both pure water and pure sucrose if possible, although this has the danger of increasing the degrees of freedom and thus over fitting. For the preliminary exploration analysis and as a first crude approximation, the scattering from the total background was scaled.

In addition to the solvent exclusion, various experimental errors may rise and lead to the background to be higher than the sample (even though the effective true background is actually less). Examples of such errors include small evaporation in the sample or the background, uncertainty/errors in the concentration measurement, etc. The accumulation of these errors may eventually increase the fluctuations seen in the measurements. In general, it was found that high resolution data play an important role in adjusting the background as the signal at the high resolution is mainly from the background. Thus, this might be a method to overcome this problem in the future; simply by recording high resolution data and putting a large weight on that portion of the curve for background adjustment.

6.3.6.2 The origins of the observed multiple phases

The scattering intensity from a mixture of uncorrelated (non-interacting) molecules or a mixture of uncorrelated (non-interacting) multiple domains/crystals, which may or may not be embedded in one another can be approximated as the sum of the scattering patterns of these molecules/domains weighted by their partial contributions to the total scattering. In other word, the experimentally measured scattering pattern from multiple crystalline phases can be described by a linear combination of individual phases present in the irradiated sample. Thus, the total scattering for *N* phases can be given by:

$$I = I_{bk} + v_1 I_1 + v_2 I_2 + v_3 I_3 + \cdots + v_n I_n = I_{bk} + \sum_{i}^{N} v_i I_i$$

Where,

I_{bk} is the total background.

v_i is the weighting coefficient of the i^{th} phase.

I_i is the scattering intensity of the i^{th} phase.

Such method has been used in many studies including mixtures of molecules, emulsions, protein ensembles (in the case of co-existence of multiple structures), intrinsically disordered proteins and in oligomeric mixture of proteins [18,161,162]. It is the bases used in the programs MIXTURE and OLIGOMER in the ATSAS package [98–100]. Further, it is routinely used in the case of physical mixtures of powders such as in soil samples. If the individual patters are on the same relative scale then the coefficients obtained can represent the molar fraction of each corresponding phase/molecule. In the case of a mixture of non-interacting components, then the coefficients which represents the molar fraction of the phases can be obtained by a non-negative linear least squares fitting algorithm [163] and the structure factor is equal to unity. In the case of the presence of interactions however, the structure factor that rises due to the interactions of the components is need to be accounted for and the fitting parameters are usually obtained by a non-linear fitting algorithm [18,161].

As a first approximation, the scattering patterns of the main phases have been measured independently and are utilized directly in the fit. These include pure components which are the background water/sucrose solution, the pure DNA, gemini (12-3-12 and 16-3-16), DPPC and DOPE. In addition, the scattering from principal interacting phases were also recorded. This includes the DNA-gemini complexes and the gemini-DOPE mixture. However, while this study was being conducted, and as described in the results above, other interaction phases that were not measured independently were also found. These new phases or complexes were not seen in gemini-DNA alone indicating that the neutral lipids are involved.

Whereas, considering these newly formed phases is important for quantitative evaluation of the partial contributions of the different phases, the fittings made here using the recorded phases only are initial approximations aimed to qualitatively explore and understand the nature of the interactions. Hence, the latter should provide clues on which phases dominate the scattering patterns. It is noteworthy that the effect of interference between the domains on the scattering pattern, however, would be at a much lower angle than the measurements presented here, due to their large sizes. Further, since the system is composed of gemini-DNA domains that are randomly distributed or embedded in a matrix of the neutral lipids then the effect of inter-domain interference could be considered negligible.

Thus, the measured scattering can be approximated by the sum of intensities of the components. Therefore, after considering the solvent exclusion (as described in section 6.3.6.1) by introducing a scaling factor V_{bk} account for the irradiated volume of the background solvent, the different formulations studied can be described as follows.

For gemini-DNA-DPPC system, the measured scattering intensity can be approximated by:

$$I = V_{bk}I_{bk} + v_{DPPC}I_{DPPC} + v_{DNA-gemini}I_{DNA-gemini} \tag{6.1}$$

For gemini-DNA-DPPC-DOPE system, the measured scattering intensity can be approximated by:

$$I = V_{bk}I_{bk} + v_{DPPC}I_{DPPC} + v_{DOPE}I_{DOPE} + v_{DNA-gemini}I_{DNA-gemini} \tag{6.2}$$

For gemini-DNA-DOPE system, the measured scattering intensity can be approximated by (*model 1*):

$$I = V_{bk}I_{bk} + v_{DOPE}I_{DOPE} + v_{DNA-gemini}I_{DNA-gemini} \tag{6.3}$$

In the case of excess gemini, we have seen evidence of interaction between excess free gemini micelles and DOPE. The newly formed phase can be accounted for by using the recorded DOPE-gemini mixtures and the free DNA scattering patterns as one of the components (*model 2*):

$$I = V_{bk}I_{bk} + v_{DOPE}I_{DOPE} + v_{DNA-gemini}I_{DNA-gemini} + v_{DOPE-gemini}I_{DOPE-gemini} + I_{DNA} \tag{6.4}$$

To reduce the number of fitting parameters in equation (*6.4*), the dilute DNA solution (I_{DNA}) scattering curve was used as a component for the fittings in the 5:1 charge ratio (excess DNA), thus equation (*6.4*) is modifies to:

$$I = V_{bk}I_{bk} + v_{DOPE}I_{DOPE} + v_{DNA-gemini}I_{DNA-gemini} + v_{DNA}I_{DNA} \tag{6.5}$$

Whereas, the gemini-Dope mixture scattering pattern ($I_{DOPE-gemini}$) was used in the other charge ratios that are prepared with excess gemini and in which evidence of this interaction is seen.

$$I = V_{bk}I_{bk} + v_{DOPE}I_{DOPE} + v_{DNA-gemini}I_{DNA-gemini} + v_{DOPE-gemini}I_{DOPE-gemini} \tag{6.6}$$

Both intensity curves were used in the 1:1 charge ratio of the DOPE formulations (i.e. equation (*6.4*)).

In principle, each phase is a partially ordered system and after Lorentz correction can be given by:

$$I_i = n_i |F_i(q)|^2 S_i(q) \tag{6.7}$$

Where,

n_i is related to the concentration (particle number density) of the phase i.

$F_i(q)$ is the form factor of the phase i.

$S_i(q)$ is the structure factor of the phase i, and it is equivalent to unity in the absence of intermolecular correlations (in the absence of a lattice).

The fitting parameters (which are the coefficients of the phases) were obtained by a non-negative linear fit using equations *(6.1)* to *(6.6)* that minimizes the Chi squared criterion χ^2 as calculated from the equation:

$$\chi^2 = \frac{1}{N} \sum_{i=1}^{N} \left(\frac{I(q_i)_{calc} - I(q_i)_{exp}}{\sigma_i} \right)^2 \tag{6.8}$$

Where,

$I(q_i)_{calc}$ is the calculated intensity form the model.

$I(q_i)_{exp}$ is the experimentally measured intensity.

σ_i is the experimental uncertainty in the intensity at point i (calculated from the standard deviations of the radially averaged pixels).

N is the number of points.

6.3.6.3 Selected examples of the fittings using the global scattering model

In this section, selected examples of the fittings using the scattering model described in the previous section are discussed.

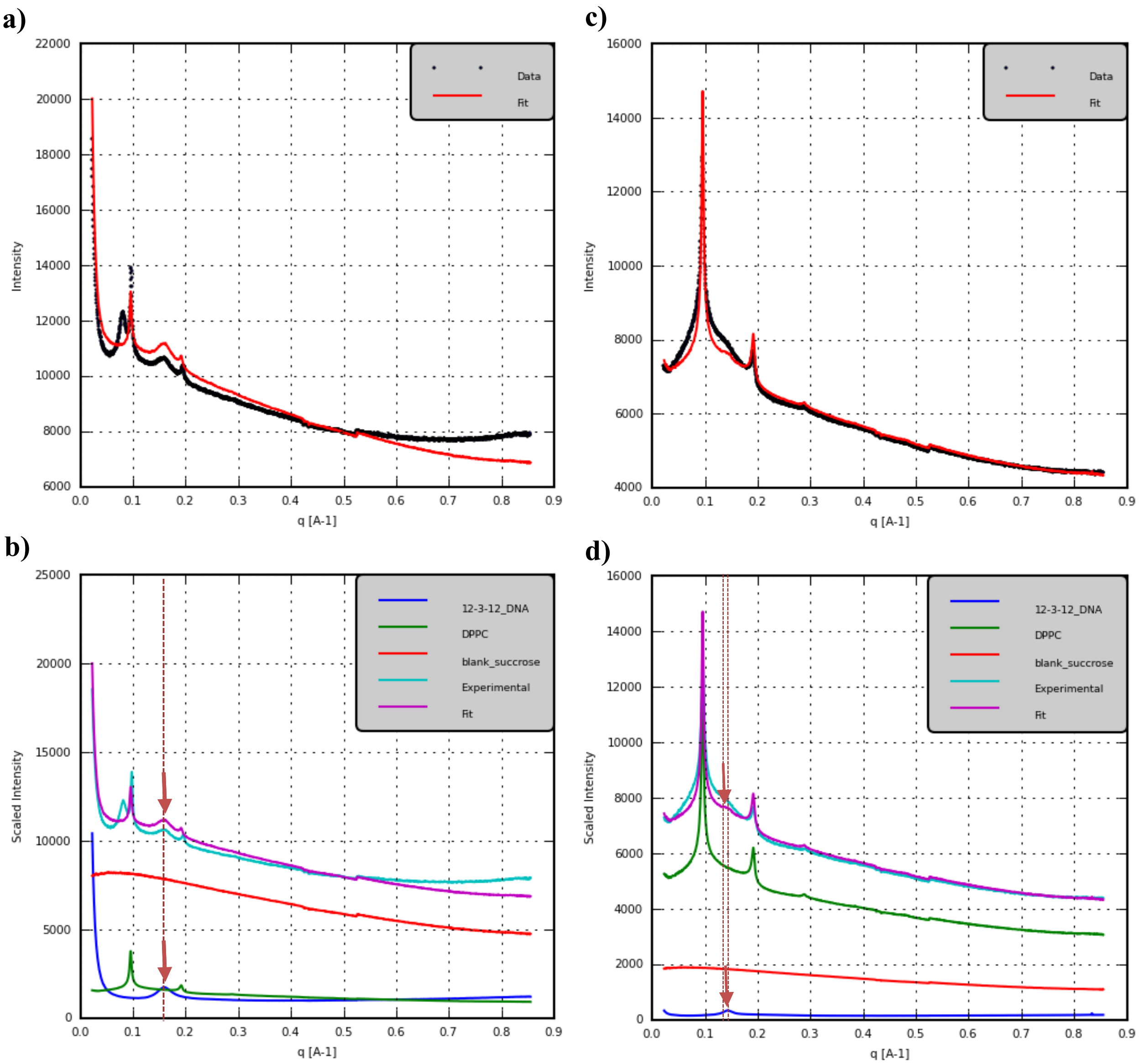

Figure 6.10. A comparison between the fittings of high and low DNA: gemini charge ratios of the 12-3-12 DNA DPPC formulations.

Panels a and b: *show the fit and the scaled scattering curves of the components of the 12-3-12 DNA DPPC formulation with a 5:1 DNA: gemini charge ratio of the 25X concentration.* ***Panels c and d:*** *show the fit and the scaled scattering curves of the components of 12-3-12 DNA DPPC formulation with a 1:5 DNA: gemini charge ratio of the 25X concentration.*

Phase \ Charge Ratio	*5:1* **DNA: gemini charge ratio (*model 1*)**		*1:5* **DNA: gemini charge ratio (*model 1*)**	
	fraction	***%***	***Fraction***	***%***
12-3-12 DNA	0.1965	25.02	0.0240	4.771
DPPC	0.1096	13.95	0.3684	73.30
blank_succrose	0.4795	61.03	0.1102	21.93
Chi Squared	0.3690		0.0255	

Table 6.3. Fitting parameters of the 12-3-12 DNA DPPC formulations with 5:1 and 1:5 DNA: gemini charge ratios at a concentration of 25X.

Figure 6.10 and Table 6.3 show the fitting results of two of the DPPC formulations with two different charge ratios. The fitting coefficient of the 12-3-12 DNA phase is lower in the formulation prepared with 1:5 DNA: gemini charge ratio than that of the 5:1 charge ratio (0.0240 and 0.1965, respectively) relative to contribution of the DPPC (0.1096 and 0.3684, respectively). This could be explained by two reasons. The first is that, there is a shift in the position of the 12-3-12 DNA complexes peak upon the addition of the neutral lipids due to the interaction of the complex with these neutral lipids (arrows and dotted lines on Figure 6.10). This however, occurs only in the case of excess gemini and not in excess DNA. Hence, the 12-3-12 DNA scattering pattern would fit better (and thus appears to contribute more) in the case of the pattern that showed no changes in the peak position (i.e. the 5:1 charge ratio). The second reason is that the Gaussian lobes rising from the scattering from the free gemini had shifted to a higher q (larger size) after the addition of the DPPC. This would lead to an apparent reduction in the contribution of the 12-3-12 DNA complexes phases to the fitting (due to disappearance of the signature of the free gemini and the formation of a new gemini-DPPC phase). From the fittings of other studied charge ratios, it can be noticed that the appearance of the gemini-DPPC phase becomes more distinct as the DNA: gemini ratio decreases (Figure 6.2). This can be explained by the presence of excess free gemini that are unbound to the DNA and hence available for the interaction with DPPC.

Despite the above observation that the scattering pattern of the 12-3-12 DNA complexes remain unchanged in the case of excess DNA (5:1 charge ratio), it can be seen that Chi squared in the fitting of the 5:1 charge ratio is still high compared to the 1:5 charge ratio (0.3690 and 0.0255, respectively). It is evident from the graphs that this is due to the presence of the new DNA-DPPC phase (L$_c$ phase) that was not accounted for. Therefore, one could conclude that at a high DNA: gemini charge ratio, and in the case of formation of large MLV, the free DNA makes complexes with DPPC vesicles which is, as discussed earlier, usually mediated by divalent ions to form a lamellar L$_c$ phase.

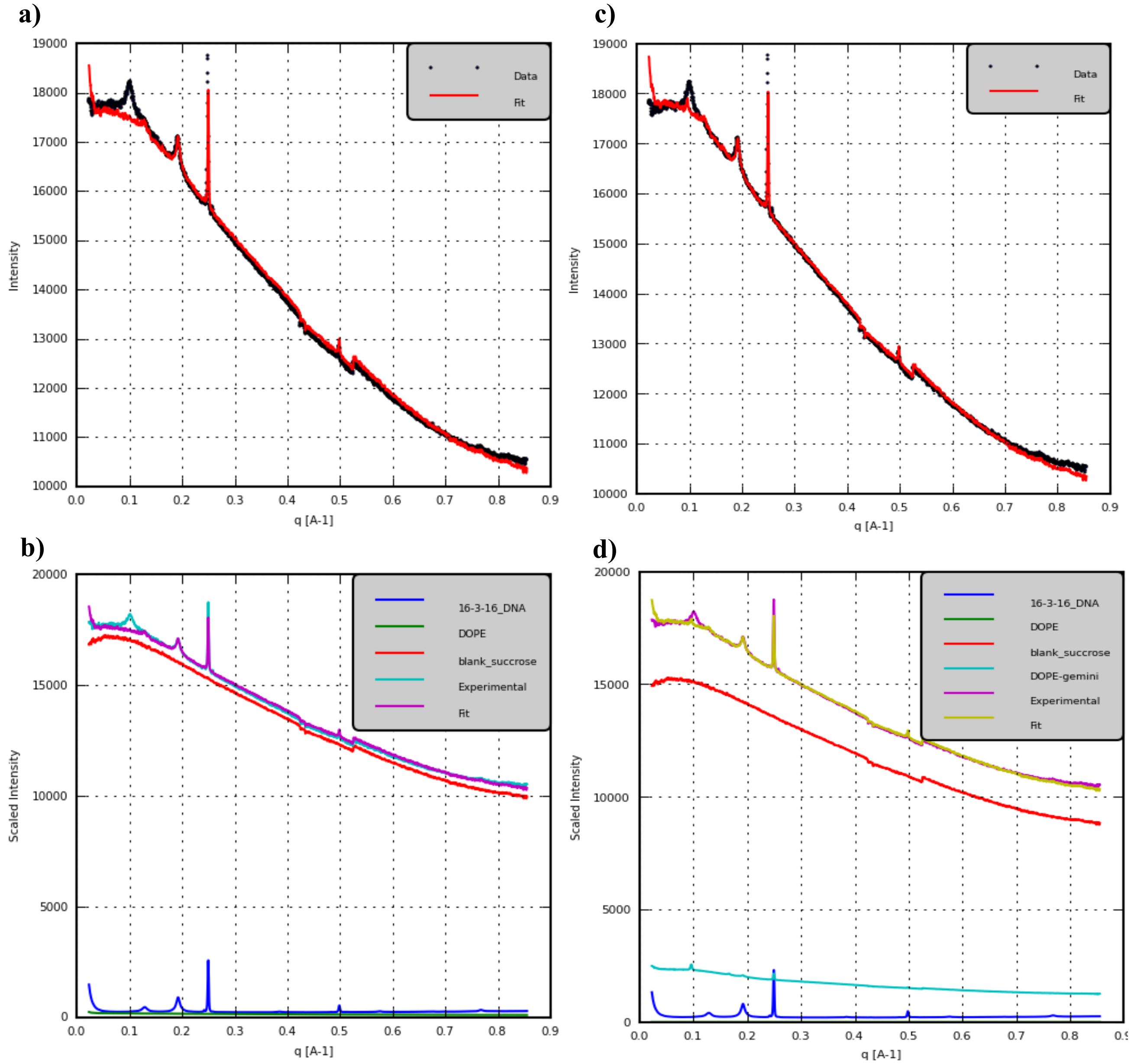

Figure 6.11. Fittings of the 16-3-16 DNA DOPE formulations with 1:10 DNA: gemini charge ratio at a concentration of 25X, obtained by using two different models.

*Panels **a** and **b** show the fit and the scaled scattering curves after the fit using the first model (model 1), respectively.*

*Similarly, panels **c** and **d** show the fit and the scaled scattering curves after the fit using the second model (model 2), respectively.*

Model / **Phase**	***model 1***		***model 2***	
	fraction	***%***	***fraction***	***%***
16-3-16 DNA	0.0395	3.758	0.0355	3.401
DOPE	0.0116	1.099	0.0000	0.000
blank_succrose	1.001	95.14	0.8906	85.33
DOPE-gemini	-	-	0.1176	11.27
Chi Squared	0.0065		0.0046	

Table 6.4. Fitting parameters of the 16-3-16 DNA DOPE formulations with 1:10 DNA: gemini charge ratio at a concentration of 25X, obtained by using two different models (models 1 & 2).

The second example that will be discussed here is the fittings of 16-3-16 DNA DOPE (at 1:10 DNA: gemini charge ratio, at a concentration of *25X*) using two different models (

Figure **6.11**). Table 6.4 shows the fitting results of the same sample by both models. Indeed, the second model which considers the gemini-DOPE mixture as one of the components shows a lower Chi squared (0.0046) than the first model (0.0065), indicating its superiority in describing the data compared to the first. It therefore can be concluded that a gemini-DOPE phase is formed in the case of excess gemini. The fitting that gave a lower Chi squared (the second model), had resulted in that the coefficient of the pure DOPE is equal to zero (0%), indicating that it is not well suited to describe the components of the formulation, while the contribution of DOPE-gemini is equal to 0.1176 (11.27%).

Generally speaking, all the 16-3-16 gemini surfactants formulations fittings were significantly improved by using the corresponding gemini-DOPE as one of the components. This confirms that a new phase was formed as a result of the interaction between DOPE and the gemini micelles. The improvement in the fits is mainly due to that the gemini-DOPE phase can account for the observed change of the lattice parameter, and for the diffuse scattering at the low angles. Similarly, a significant improvement of the fits of the 12-3-12 gemini-DOPE formulations that contains excess gemini were also obtained upon using the gemini-DOPE scattering curves as one of components. In most cases, especially in the dilute regimen, the linear fitting lead to coefficients for the free DNA that are equal to zero (data not shown). In the few cases where fitting showed lower Chi squared, the difference was at the fourth decimal place indicating that the improvement is not significant. This confirms that in the case of excess gemini surfactants the scattering patterns from the formulations are dominated by a newly formed gemini-DOPE phase.

6.3.6.4 Limitations in initial model and factors that decrease the goodness of fit

Obtained fitting parameters can be useful and represents the molar fraction of each phase if accurate fits are achieved. One may consider the fits to be accurate if all Bragg's peaks are fitted and Chi squared (or the goodness of fit) is statistically significant. Although this has been achieved in some samples, this has not been the case in many others. Nonetheless, at this stage, the general trends have been qualitatively determined, and this simple linear fit could be used to determine initial parameters for a more detailed model. For better quantitation, the model should be able to quantitatively account for factors as: lattice parameter changes, L_c phase, exact models of DPPC- and DOPE-gemini interactions, separate of sucrose from neutral lipids and disorder parameters for neutral lipids.

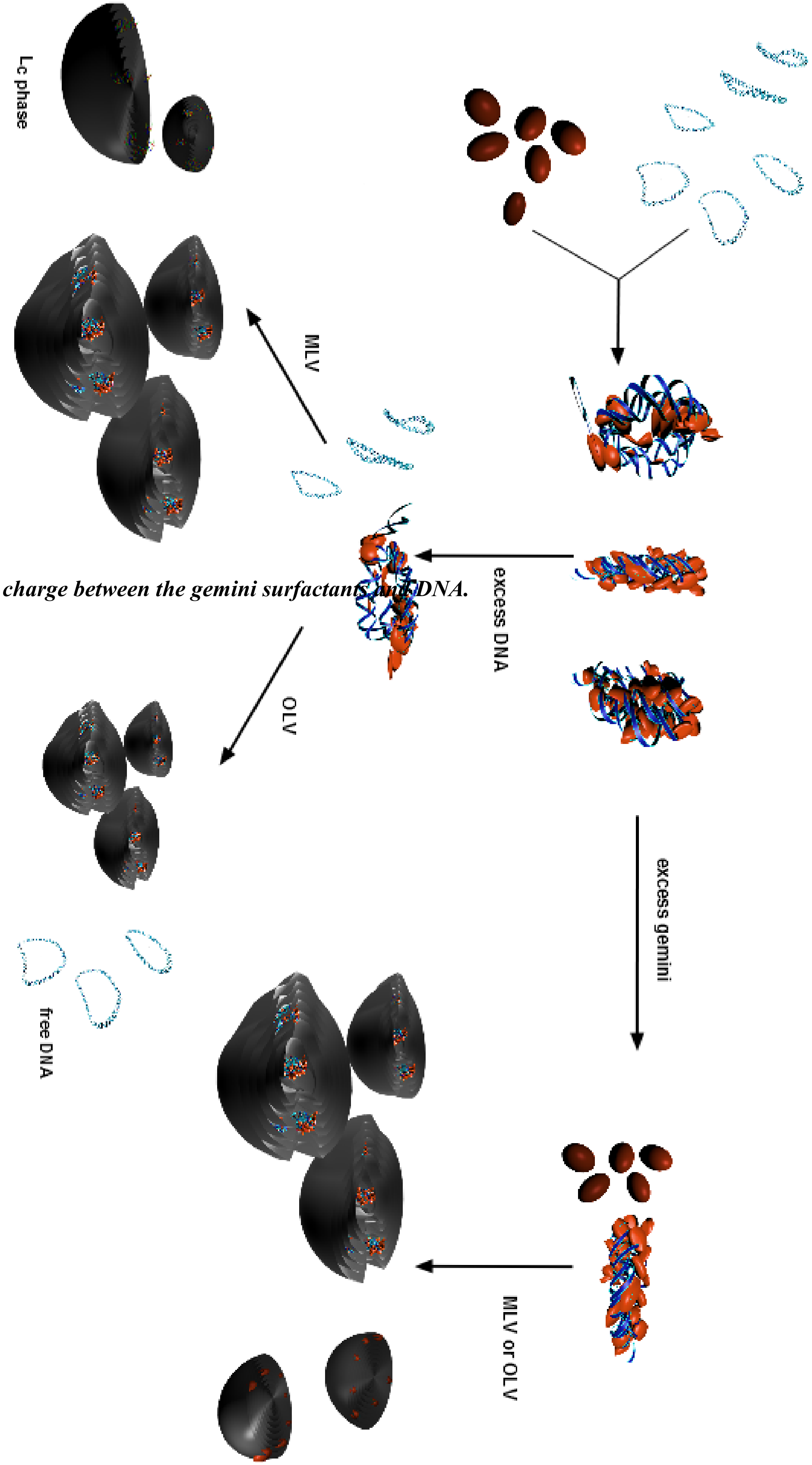

wing a summary of the effect of varying the charge between the gemini surfactants and DNA.

6.4 Conclusions and future prospective

In this chapter, the structure of gemini-based DNA delivery systems and the effect of varying the DNA: gemini charge ratios was systematically studied using small angle scattering. A summary of the findings is shown in Figure 6.12. A pictorial comparative summary of the diffraction patterns used in this study for different gemini, neutral lipids and DNA: gemini charge ratios can be found in Appendix B.

Upon the addition of neutral lipid liposomes, gemini-DNA-neutral lipids complexes are formed. The scattering patterns of the latter have shown evidence of the strong interaction of the neutral lipids with the free gemini surfactants, as well as, with the overcharged DNA-gemini complexes. Interestingly, the interaction between the DNA-gemini complexes and the neutral lipids was shown to be favoured in the case of excess gemini. Thus, overcharging the DNA-gemini complexes seem to aid in its incorporation into the neutral lipid matrix. Indeed, the interaction increases the degree of disorder within the neutral lipids stacks. An initial, semi-quantitative, estimates of the molar fractions of the phases constituting the formulations were obtained.

Though only a few selected types of gemini surfactants were used in the formulations, the general trends seen are likely to be observed for many other gemini-based formulations prepared using the same methodology. Most likely, the expected difference between one gemini and another would only be in the degree by which the reported interactions occurs.

Future studies will attempt to develop methodologies that would enable more accurate fittings using the initial parameters obtained in this study. The latter, may aid in the development of a quantitative measure for the interaction of the gemini surfactants with the neutral lipids. This would allow the comparison between the ability of the different gemini surfactants to become incorporated into the neutral lipid matrix in various conditions.

7 OVERALL CONCLUSION

Small angle scattering is a technique used to determine the structure of biomolecules including those that are in liquid crystalline in nature such as lipids. This thesis can be divided into three main sections. The first is related to the SAXS instrumentation. In this section, helium and vacuum chambers were developed to enable testing the feasibility of the technique on the CMCF beamlines at the Canadian Light Source.

In the second section, a pipeline for automated SAXS/WAXS data processing and analysis was developed. The latter demonstrated the feasibility of automating of the data reduction and the basic analysis. The third section of the thesis demonstrated an application of the technique on the gemini surfactant drug delivery system. All of the pure surfactants, their DNA-complexes and the DNA-gemini-neutral lipids complexes were examined. Further, the effect of varying the charge ratios via changing the DNA and the gemini relative concentrations has been demonstrated. While the 12-3-12 gemini formed ellipsoid and thread micellar shapes, the 16-3-16 gemini surfactants has shown a hexagonally close packed arrangement of micelles. When DNA was added to the pure gemini, a sharp peak was observed indicating the formation of a crystalline lattice.

In the case of low DNA: gemini charge ratios, evidence of the presence of excess free surfactants in solution was seen. When the neutral lipids are added, they tend to interact with these free surfactants. On the other hand, in high DNA: gemini charge ratios, and only at large enough concentrations, evidence of an Lc phase was observed after the neutral lipids were added. Moreover, the neutral lipids generally had shown evidence of interaction with DNA: gemini complexes at charge ratios 1:1 and above, and did not show this same interaction with complexes at 5:1 charge ratio. These interactions demonstrate the important role of overcharging in the incorporation of the DNA-gemini complexes into the neutral lipids vesicles.

BIBLIOGRAPHY

1. Watson, J. D. & Crick, F. H. Molecular structure of nucleic acids; a structure for deoxyribose nucleic acid. *Nature* **171,** 737–8 (1953).
2. Franklin, R. E. & Gosling, R. G. The structure of sodium thymonucleate fibres. I. The influence of water content. *Acta Crystallogr.* **6,** 673–677 (1953).
3. Luzzati, V., Mustacchi, H., Skoulios, a. & Husson, F. La structure des colloïdes d'association. I. Les phases liquide–cristallines des systèmes amphiphile–eau. *Acta Crystallogr.* **13,** 660–667 (1960).
4. Nelson, D. L. & Cox, M. M. *Lehninger Principles of Biochemistry, Fourth Edition*. 1100–1101 (W. H. Freeman, 2004).
5. Sinden, R. R. *DNA Structure and Function*. (Academic Press, 1994).
6. Ulrich, A. S. Biophysical Aspects of Using Liposomes as Delivery Vehicles. *Bioscience* **22,** 129–150 (2002).
7. Xiang, T.-X. & Anderson, B. D. Liposomal drug transport: a molecular perspective from molecular dynamics simulations in lipid bilayers. *Adv. Drug Deliv. Rev.* **58,** 1357–78 (2006).
8. Luger, K. & Collins, F. Nucleosomes : Structure and Function. *Encycl. Life Sci.* 1–8 (2001).
9. Xiong, Y. Protein – Nucleic Acid Interaction : Major Groove Recognition Determinants. *Encycl. Life Sci.* 1–8 (2001).
10. Koltover, I., Salditt, T. & Safinya, C. R. Phase diagram, stability, and overcharging of lamellar cationic lipid-DNA self-assembled complexes. *Biophys. J.* **77,** 915–24 (1999).
11. Katsaras, J. & Gutberlet, T. *Lipid Bilayers: Structure and Interactions*. 1–22 (Springer-Verlag Berlin Heidelberg, 2001).
12. Kirian, R. A. *et al.* Femtosecond protein nanocrystallography — data analysis methods. *Opt. Express* **18,** 5713–5723 (2010).
13. Chapman, H. N. *et al.* Femtosecond X-ray protein nanocrystallography. *Methods* 3–8 (2011).
14. Caille, A. Physique cristalline - Remarques sur la diffusion des rayons X dans les smectiques A. *A. C. R. Acad. Sc.* **Serie B 27,** 891–893 (1972).
15. Hosemann, R. & Bagchi, S. N. *Direct Analysis of Diffraction by Matter*. (North-Holland Publishing, 1962).
16. Pabst, G., Rappolt, M., Amenitsch, H. & Laggner, P. Structural information from multilamellar liposomes at full hydration: full q-range fitting with high quality x-ray data. *Phys. Rev. E. Stat. Phys. Plasmas. Fluids. Relat. Interdiscip. Topics* **62,** 4000–9 (2000).
17. Weyerich, B. & Glatter, O. Small-angle scattering of interacting particles . II. Generalized indirect Fourier transformation under consideration of the effective structure factor for polydisperse systems. (1999).
18. Brunner-Popela, J. *et al.* Small-angle scattering of interacting particles. III. D2O-C12E5 mixtures and microemulsions with n-octane. *J. Chem. Phys.* **110,** 10623 (1999).
19. Fruhwirth, T., Fritz, G., Freiberger, N. & Glatter, O. Structure and order in lamellar phases determined by small-angle scattering. *J. Appl. Crystallogr.* **37,** 703–710 (2004).

20. Fritz, G. & Glatter, O. Structure and interaction in dense colloidal systems : evaluation of scattering data by the generalized indirect Fourier transformation method. **2403,** (2006).
21. Schmahl, G. & Rudolph, D. *X-Ray Microscopy*. **43,** (Springer Berlin Heidelberg, 1984).
22. Ade, H. *et al.* Chemical contrast in X-ray microscopy and spatially resolved XANES spectroscopy of organic specimens. *Science* **258,** 972–5 (1992).
23. Sayre, D. Some implications of a theorem due to Shannon. *Acta Crystallogr.* **5,** 843–843 (1952).
24. Miao, J., Charalambous, P., Kirz, J. & Sayre, D. Extending the methodology of X-ray crystallography to allow imaging of micrometre-sized non-crystalline specimens. **400,** 342–344 (1999).
25. Gaffney, K. J. & Chapman, H. N. Imaging atomic structure and dynamics with ultrafast x-ray scattering. *Science* **316,** 1444–8 (2007).
26. Saldin, D. K. *et al.* Beyond small-angle x-ray scattering: Exploiting angular correlations. *Phys. Rev. B* **81,** 174105 (2010).
27. Giewekemeyer, K. *et al.* Quantitative biological imaging by ptychographic x-ray diffraction microscopy. *Proc. Natl. Acad. Sci. U. S. A.* **107,** 529–34 (2010).
28. Dierolf, M. *et al.* Ptychographic X-ray computed tomography at the nanoscale. *Nature* **467,** 436–9 (2010).
29. Chapman, H. N. *et al.* Femtosecond time-delay X-ray holography. *Nature* **448,** 676–9 (2007).
30. Solids, N. Structural modelling using the reverse Monte Carlo technique : Application to amorphous semiconductors. 88–95 (1998).
31. Mellergård, a. & McGreevy, R. L. Reverse Monte Carlo modelling of neutron powder diffraction data. *Acta Crystallogr. Sect. A Found. Crystallogr.* **55,** 783–789 (1999).
32. Farrow, C. L. *et al.* PDFfit2 and PDFgui: computer programs for studying nanostructure in crystals. *J. Phys. Condens. Matter* **19,** 335219 (2007).
33. Schaub, P., Weber, T. & Steurer, W. Analysis and modelling of structural disorder by the use of the three-dimensional pair distribution function method exemplified by the disordered twofold superstructure of decagonal Al–Cu–Co. *J. Appl. Crystallogr.* **44,** 134–149 (2010).
34. Luzzati, V. & Tardieu, A. Lipid phases: structure and structural transitions. *Annu. Rev. Phys. Chem.* **25,** 79–94 (1974).
35. Dong, Y.-D. & Boyd, B. J. Applications of X-ray scattering in pharmaceutical science. *Int. J. Pharm.* **417,** 101–11 (2011).
36. Guinier, A. *X-Ray Diffraction: In Crystals, Imperfect Crystals, and Amorphous Bodies*. (W. H. Freeman and Company, 1963).
37. Warren, B. E. *X-ray Diffraction*. (Addison-Wesley Publishing Company, Inc., 1969).
38. Pecharsky, V. K. & Zavalij, P. Y. *Fundamentals of Powder Diffraction and Structural Characterization of Materials*. *Powder Diffr.* (Springer US, 2009).
39. Giacovazzo, C. *et al. Fundamentals of Crystallography*. (Oxford University Press, 2002).
40. Feigin, L. A. & Svergun, D. I. *Structure Analysis by Small-Angle X-Ray and Neutron Scattering*. (Plenum, 1987).
41. Glatter, O. & Kratky, O. *Small Angle X-ray Scattering*. (Academic Press, 1982).
42. Pabst, G., Koschuch, R., Pozo-navas, B., Rappolt, M. & Laggner, P. Structural analysis of weakly ordered membrane stacks. 1378–1388 (2003).

43. Pabst, G. Global properties of biomimetic membranes: prespectives on molecular features. *Biophys. Rev. Lett.* **1,** 57–84 (2006).
44. Rappolt, M., Laggner, P. & Pabst, G. *Structure and elasticity of phospholipid bilayers in the L-alpha phase: A comparison of phophatidylcholine and phosphatidylethanolamine membranes*. *Recent Res. Devel. Biophys.* **3,** 363–392 (2004).
45. Gruner, S. A. L. Lipid Polymorphism: The Molecular Bask of Nonbilayer Phases. *Annu. Rev. Biophys. Chem.* **14,** 211–238 (1985).
46. Tristram-Nagle, S., Wiener, M. C., Yang, C. P. & Nagle, J. F. Kinetics of the subtransition in dipalmitoylphosphatidylcholine. *Biochemistry* **26,** 4288–94 (1987).
47. Nagle, J. F. & Wilkinson, D. A. Dilatometric studies of the subtransition in dipalmitoylphosphatidylcholine. *Biochemistry* **21,** 3817–3821 (1982).
48. Tristram-Nagle, S. & Nagle, J. F. Lipid bilayers: thermodynamics, structure, fluctuations, and interactions. *Chem. Phys. Lipids* **127,** 3–14 (2004).
49. Hyde, S. T. Identification of Lyotropic Liquid Crystalline Mesophases. *Handb. Appl. Surf. Colloid Chem. John Wiley Sons* (2001).
50. Zhang, R., Suter, R. M. & Nagle, J. F. Theory of the structure factor of lipid bilayers. *Phys. Rev. E* **50,** 5047–5060 (1994).
51. Zhang, R. *et al.* Small-angle x-ray scattering from lipid bilayers is well described by modified Caillé theory but not by paracrystalline theory. *Biophys. J.* **70,** 349–57 (1996).
52. Perroni, D. V. & Mahanthappa, M. K. Inverse Pm$\bar{3}$n cubic micellar lyotropic phases from zwitterionic triazolium gemini surfactants. *Soft Matter* **9,** 7919 (2013).
53. Venugopal, E., Bhat, S. K., Vallooran, J. J. & Mezzenga, R. Phase behavior of lipid-based lyotropic liquid crystals in presence of colloidal nanoparticles. *Langmuir* **27,** 9792–800 (2011).
54. Harper, P. E., Mannock, D. a, Lewis, R. N., McElhaney, R. N. & Gruner, S. M. X-ray diffraction structures of some phosphatidylethanolamine lamellar and inverted hexagonal phases. *Biophys. J.* **81,** 2693–706 (2001).
55. Turner, D. C. & Gruner, S. M. X-ray diffraction reconstruction of the inverted hexagonal (HII) phase in lipid-water systems. *Biochemistry* **31,** 1340–55 (1992).
56. Yang, L. & Huang, H. W. A rhombohedral phase of lipid containing a membrane fusion intermediate structure. *Biophys. J.* **84,** 1808–17 (2003).
57. Ungar, G., Liu, Y., Zeng, X., Percec, V. & Cho, W.-D. Giant supramolecular liquid crystal lattice. *Science* **299,** 1208–11 (2003).
58. Lee, M., Cho, B., Jang, Y. & Zin, W. Spontaneous Organization of Supramolecular Rod-Bundles into a Body-Centered Tetragonal Assembly in Coil-Rod-Coil Molecules. *J. Am. Chem. Soc.* **122,** 7449–7455 (2000).
59. Gramsbergen, E. F., Hoving, H. J. & Jeu, W. H. De. X-ray investigation of discotic mesophases of alkylthio substituted triphenylenes. *Liq. Cryst.* **1,** 397–400 (1986).
60. Prasad, S. K. & Rao, D. S. S. X-RAY Studies on the Columnar Structures of Discotic Liquid Crystals. *Mol. Cryst. Liq. Cryst.* **396,** 121–139 (2003).
61. Zeng, X., Liu, Y. & Impéror-Clerc, M. Hexagonal close packing of nonionic surfactant micelles in water. *J. Phys. Chem. B* **111,** 5174–9 (2007).
62. Israelachvili, J. N. *Intermolecular and surface forces*. (Academic Press, 1992).
63. Kaasgaard, T. & Drummond, C. J. Ordered 2-D and 3-D nanostructured amphiphile self-assembly materials stable in excess solvent. *Phys. Chem. Chem. Phys.* **8,** 4957–75 (2006).

64. Koltover, I., Salditt, T., Rädler, J. O. & Safinya, C. R. An inverted hexagonal phase of cationic liposome-DNA complexes related to DNA release and delivery. *Science* **281,** 78–81 (1998).
65. Richard E. Dickerson *et al.* Definitions and nomenclature of nucleic acid structure components. *Nucleic Acids Res.* **17,** 1797–1803 (1989).
66. Saenger, W. *Principles of Nucleic Acid Structure*. (Springer, 1984).
67. Yevdokimov, Y. M., Salyanov, V. I., Semenov, S. V. & Skuridin, S. G. *DNA Liquid-Crystalline Dispersions and Nanoconstructions*. (CRC Press, 2011).
68. Langridge, R. *et al.* The molecular configuration of deoxyribonucleic acid. *J. Mol. Biol.* **2,** 38–IN12 (1960).
69. Langridge, R., Wilson, H. R., Hooper, C. W., Wilkins, M. H. F. & Hamilton, L. D. The molecular configuration of deoxyribonucleic acid. *J. Mol. Biol.* **2,** 19–IN11 (1960).
70. Rädler, J. O., Koltover, I., Salditt, T. & Safinya, C. R. Structure of DNA-cationic liposome complexes: DNA intercalation in multilamellar membranes in distinct interhelical packing regimes. *Science* **275,** 810–4 (1997).
71. Felgner, P. L. *et al.* Lipofection: a highly efficient, lipid-mediated DNA-transfection procedure. *Proc. Natl. Acad. Sci. U. S. A.* **84,** 7413–7 (1987).
72. Ewert, K. K. *et al.* A columnar phase of dendritic lipid-based cationic liposome-DNA complexes for gene delivery: hexagonally ordered cylindrical micelles embedded in a DNA honeycomb lattice. *J. Am. Chem. Soc.* **128,** 3998–4006 (2006).
73. Bouxsein, N. F., McAllister, C. S., Ewert, K. K., Samuel, C. E. & Safinya, C. R. Structure and gene silencing activities of monovalent and pentavalent cationic lipid vectors complexed with siRNA. *Biochemistry* **46,** 4785–92 (2007).
74. Leal, C., Bouxsein, N. F., Ewert, K. K. & Safinya, C. R. Highly efficient gene silencing activity of siRNA embedded in a nanostructured gyroid cubic lipid matrix. *J. Am. Chem. Soc.* **132,** 16841–7 (2010).
75. Koltover, I., Salditt, T. & Safinya, C. R. Phase diagram, stability, and overcharging of lamellar cationic lipid-DNA self-assembled complexes. *Biophys. J.* **77,** 915–24 (1999).
76. Ahmad, A. *et al.* New multivalent cationic lipids reveal bell curve for transfection efficiency versus membrane charge density: lipid-DNA complexes for gene delivery. *J. Gene Med.* **7,** 739–48 (2005).
77. Lin, A. J. *et al.* Three-Dimensional Imaging of Lipid Gene-Carriers : Membrane Charge Density Controls Universal Transfection Behavior in Lamellar Cationic Liposome-DNA Complexes. *Biophys. J.* **84,** (2003).
78. Fischetti, R. *et al.* The BioCAT undulator beamline 18ID: a facility for biological non-crystalline diffraction and X-ray absorption spectroscopy at the Advanced Photon Source. *J. Synchrotron Radiat.* **11,** 399–405 (2004).
79. Chu, B. & Hsiao, B. S. Small-angle X-ray scattering of polymers. *Chem. Rev.* **101,** 1727–61 (2001).
80. Timmann, A. *et al.* Small angle x-ray scattering with a beryllium compound refractive lens as focusing optic. *Rev. Sci. Instrum.* **80,** 046103 (2009).
81. Krywka, C. A. *et al.* The Nanofocus Endstation of the MINAXS Beamline of PETRA III. in *SRI 2009, 10TH Int. Conf. Radiat. Instrum.* **1234,** 879–882 (AIP Publishing, 2010).
82. Schroer, C. G. *et al.* Mapping the local nanostructure inside a specimen by tomographic small-angle x-ray scattering. *Appl. Phys. Lett.* **88,** 164102 (2006).

83. Evans, H. M., Dootz, R., Köster, S., Struth, B. & Pfohl, T. X-ray microdiffraction on flow-controlled biomolecular assemblies. *Bull. Polish Acad. Sci. Tech. Sci.* **55,** 217–227 (2007).
84. Barrett, R. *et al.* X-ray microfocussing combined with microfluidics for on-chip X-ray scattering measurements. *Lab Chip* **6,** 494–9 (2006).
85. Amenitsch, H. Microfluidic Devices For SAXS. *Proc. Natl. Acad. Sci. U. S. A.* 1–7 (2007).
86. Hura, G. L. *et al.* Robust, high-throughput solution structural analyses by small angle X-ray scattering (SAXS). *Nat. Methods* **6,** 606–12 (2009).
87. Blanchet, C. E. *et al.* Instrumental setup for high-throughput small- and wide-angle solution scattering at the X33 beamline of EMBL Hamburg. *J. Appl. Crystallogr.* **45,** 489–495 (2012).
88. Toft, K. N. *et al.* High-Throughput Small Angle X-ray Scattering from Proteins in Solution Using a Microfluidic Front-End. *Mach. Learn.* **80,** 3648–3654 (2008).
89. Grochulski, P., Blomqvist, I. & Delbaere, L. Status of the Canadian Macromolecular Crystallography Facility: Design and Commissioning of the 08ID-1 Beamline at the Canadian Light Source. *LA Phys. AU CANADA* 301–304 (2006).
90. Duffy, A., Fodje, M., Berg, R. & Grochulski, P. Canadian Macromolecular Crystallography Facility (CMCF) 08ID-1 status update. *Nucl. Instruments Methods Phys. Res. Sect. A Accel. Spectrometers, Detect. Assoc. Equip.* **582,** 82–83 (2007).
91. Grochulski, P., Fodje, M. N., Gorin, J., Labiuk, S. L. & Berg, R. Beamline 08ID-1, the prime beamline of the Canadian Macromolecular Crystallography Facility. *J. Synchrotron Radiat.* **18,** 681–4 (2011).
92. Grochulski, P. *et al.* Canadian macromolecular crystallography facility: a suite of fully automated beamlines. *J. Struct. Funct. Genomics* (2012).
93. Svergun, D. I. & Koch, M. H. J. Small-angle scattering studies of biological macromolecules in solution. **66,** 1735–1782 (2003).
94. Fritz, G. & Glatter, O. Structure and interaction in dense colloidal systems: evaluation of scattering data by the generalized indirect Fourier transformation method. *J. Phys. Condens. Matter* **18,** S2403–S2419 (2006).
95. Bonneté, F., Ferté, N., Astier, J. P. & Veesler, S. Protein crystallization: Contribution of small angle X-ray scattering (SAXS). *J. Phys. IV* **118,** 3–13 (2004).
96. Nagle, J. F. & Tristram-nagle, S. Structure of lipid bilayers. *Pace Pacing Clin. Electrophysiol.* **1469,** (2000).
97. Glatter, O. Evaluation of small-angle scattering data from lamellar and cylindrical particles by the indirect transformation method. *J. Appl. Crystallogr.* **13,** 577–584 (1980).
98. Konarev, P. V, Petoukhov, M. V, Volkov, V. V, Svergun, D. I. & Dmitri, I. ATSAS 2 . 1 , a program package for small-angle scattering data analysis scattering data analysis. 277–286 (2006).
99. Petoukhov, M. V. *et al.* New developments in the ATSAS program package for small-angle scattering data analysis. *J. Appl. Crystallogr.* **45,** 342–350 (2012).
100. Konarev, P. V *et al.* PRIMUS : a Windows PC-based system for small-angle scattering data analysis PRIMUS : a Windows PC-based system for small- angle scattering data analysis. *Primus* 1277–1282 (2003).
101. Kucerka, N., Katsaras, J. & Nagle, J. F. Comparing membrane simulations to scattering experiments: introducing the SIMtoEXP software. *J. Membr. Biol.* **235,** 43–50 (2010).

102. Allaire, M. & Yang, L. Biomolecular solution X-ray scattering at the National Synchrotron Light Source. *J. Synchrotron Radiat.* **18,** 41–4 (2011).
103. Nielsen, S. S., Toft, K. N., Snakenborg, D. & Jeppesen, M. G. BioXTAS RAW , a software program for high- throughput automated small-angle X-ray scattering data reduction and preliminary analysis. *J. Appl. Crystallogr.* **42,** 959–964 (2009).
104. Hammersley, A. P., Svensson, S. O., Hanfland, M., Fitch, A. N. & Hausermann, D. Two-dimensional detector software: From real detector to idealised image or two-theta scan. *High Press. Res.* **14,** 235–248 (1996).
105. Poitevin, F., Orland, H., Doniach, S., Koehl, P. & Delarue, M. AquaSAXS: a web server for computation and fitting of SAXS profiles with non-uniformally hydrated atomic models. *Nucleic Acids Res.* **39,** W184–9 (2011).
106. Schneidman-Duhovny, D., Hammel, M. & Sali, A. FoXS: a web server for rapid computation and fitting of SAXS profiles. *Nucleic Acids Res.* **38,** W540–4 (2010).
107. Road, H., Jose, S., Division, A. T., Company, E. K. & Park, K. X-ray Powder Diffraction Analysis of Silver Behenate , a Possible Low-Angle Diffraction Standard. *Powder Diffr.* **3,** 180–184 (1993).
108. Lee, B., Lo, C. & Winans, R. E. short communications Silver behenate as a calibration standard of grazing- incidence small-angle X-ray scattering. *Contract* **1,** 749–751 (2006).
109. Foldvari, M., Badea, I., Wettig, S., Verrall, R. & Bagonluri, M. Structural characterization of novel gemini non-viral DNA delivery systems for cutaneous gene therapy. *J. Exp. Nanosci.* **1,** 165–176 (2006).
110. Bernheim-Groswasser, A., Zana, R. & Talmon, Y. Sphere-to-Cylinder Transition in Aqueous Micellar Solution of a Dimeric (Gemini) Surfactant. *J. Phys. Chem. B* **104,** 4005–4009 (2000).
111. Foldvari, M., Badea, I., Wettig, S., Verrall, R. & Bagonluri, M. Structural characterization of novel gemini non-viral DNA delivery systems for cutaneous gene therapy. *J. Exp. Nanosci.* **1,** 165–176 (2006).
112. Bergström, L. M. & Garamus, V. M. Geometrical shape of micelles formed by cationic dimeric surfactants determined with small-angle neutron scattering. *Langmuir* **28,** 9311–21 (2012).
113. Wettig, S. D., Verrall, R. E. & Foldvari, M. Gemini Surfactants : A New Family of Building Blocks for Non-Viral Gene Delivery Systems. *Gene* 9–23 (2008).
114. Badea, I., Wettig, S., Verrall, R. & Foldvari, M. Topical non-invasive gene delivery using gemini nanoparticles in interferon-c-deficient mice. *Eur. J. Pharm. Biopharm.* **65,** 414–422 (2007).
115. Badea, I., Verrall, R. & Baca-estrada, M. In vivo cutaneous interferon-γ gene delivery using novel dicationic (gemini) surfactant – plasmid complexes. *J. Gene Med.* 1200–1214 (2005).
116. Aswal, V. K., Goyal, P. S., De, S., Bhattacharya, S. & Amenitsch, H. Small-angle X-ray scattering from micellar solutions of gemini surfactants. *Chem. Phys. Lett.* **329,** 336–340 (2000).
117. Bernheim-Groswasser, A., Zana, R. & Talmon, Y. Sphere-to-Cylinder Transition in Aqueous Micellar Solution of a Dimeric (Gemini) Surfactant. *J. Phys. Chem. B* **104,** 4005–4009 (2000).
118. In, A. Analysis of small-angle scattering data from colloids and polymer solutions : modeling and least-squares fitting I J a n Skov Pedersen. **70,** 171–210 (1997).

119. Castelletto, V. & Hamley, I. W. Modelling small-angle scattering data from micelles. *Curr. Opin. Colloid Interface Sci.* **7,** 167–172 (2002).
120. Ewert, K., Ahmad, A., Evans, H. M., Schmidt, H.-W. & Safinya, C. R. Efficient synthesis and cell-transfection properties of a new multivalent cationic lipid for nonviral gene delivery. *J. Med. Chem.* **45,** 5023–9 (2002).
121. Pisani, M., Mobbili, G., Placentino, I. F., Smorlesi, A. & Bruni, P. Biophysical Characterization of Complexes of DNA with Mixtures of the Neutral Lipids 1 , 2-Dioleoyl-sn-glycero-3-phosphoethanolamine- N-hexanoylamine or 1,2-Dioleoyl-sn-glycero-3-phosphoethanolamine- N-dodecanoylamine and 1,2-Dioleoyl-sn-glycero-3-phospho. *J. Phys. Chem. B* **115,** 10198–10206 (2011).
122. Radhakrishnan, A. V., Ghosh, S. K., Pabst, G., Raghunathan, V. A. & Sood, A. K. Tuning DNA-amphiphile condensate architecture with strongly binding counterions. *Proc. Natl. Acad. Sci.* **109,** 6394–6398 (2012).
123. Aswal, V., De, S., Goyal, P., Bhattacharya, S. & Heenan, R. Small-angle neutron scattering study of micellar structures of dimeric surfactants. *Phys. Rev. E* **57,** 776–783 (1998).
124. Lee, H. I., Kim, J. M. & Stucky, G. D. Periodic mesoporous organosilica with a hexagonally pillared lamellar structure. *J. Am. Chem. Soc.* **131,** 14249–51 (2009).
125. Hatton, B., Landskron, K. A. I., Whitnall, W., Perovic, D. & Ozin, G. A. Past , Present , and Future of Periodic Mesoporous OrganosilicassThe PMOs Periodic Mesoporous Organosilicas with. **38,** 305–312 (2005).
126. Wang, C. *et al.* Investigation of complexes formed by interaction of cationic gemini surfactants with deoxyribonucleic acid. *Phys. Chem. Chem. Phys.* **9,** 1616–28 (2007).
127. Nieh, M.-P., Kučerka, N. & Katsaras, J. Formation mechanism of self-assembled unilamellar vesiclesSpecial issue on Neutron Scattering in Canada. *Can. J. Phys.* **88,** 735–740 (2010).
128. Marrink, S. J. & Mark, A. E. Molecular dynamics simulation of the formation, structure, and dynamics of small phospholipid vesicles. *J. Am. Chem. Soc.* **125,** 15233–42 (2003).
129. Pullmannová, P. *et al.* The ionic strength effect on the DNA complexation by DOPC - gemini surfactants liposomes. *Biophys. Chem.* **160,** 35–45 (2012).
130. Pullmannová, P., Funari, S. S., Devínsky, F. & Uhríková, D. The DNA-DNA spacing in gemini surfactants-DOPE-DNA complexes. *Biochim. Biophys. Acta* **1818,** 2725–31 (2012).
131. Nagle, J. F. *et al.* X-ray structure determination of fully hydrated L alpha phase dipalmitoylphosphatidylcholine bilayers. *Biophys. J.* **70,** 1419–31 (1996).
132. Kucerka, N., Tristram-Nagle, S. & Nagle, J. F. Closer look at structure of fully hydrated fluid phase DPPC bilayers. *Biophys. J.* **90,** L83–5 (2006).
133. Pisani, M., Bruni, P., Caracciolo, G., Caminiti, R. & Francescangeli, O. Structure and phase behavior of self-assembled DPPC-DNA-metal cation complexes. *J. Phys. Chem. B* **110,** 13203–11 (2006).
134. Rappolt, M. *et al.* New evidence for gel-liquid crystalline phase coexistence in the ripple phase of phosphatidylcholines. *Eur. Biophys. J.* **29,** 125–133 (2000).
135. Pisani, M., Mobbili, G. & Bruni, P. in *Non-Viral Gene Ther.* (Yuan, X.) 319–348 (2011).
136. Torbet, J. & Dicapua, E. Supercoiled DNA is interwound in liquid crystalline solutions. *EMBO J.* **8,** 4351–4356 (1989).

137. Safinya, C. R. Structures of lipid – DNA complexes : supramolecular assembly and gene delivery The lamellar L C. *Curr. Opin. Struct. Biol.* **11,** 440–448 (2001).
138. Tsuchida, E., Seki, N. & Ohno, H. Phase separation in mixed liposomes of dipalmitoyl phosphatidylcholine and di- 2,4- octadecadiene phosphatidylcholine. *Die Makromol. Chemie* **187,** 1351–1358 (1986).
139. Munro, S. Lipid Rafts : Elusive or Illusive ? *Cell* **115,** 377–388 (2003).
140. Quinn, P. J. Lipid-lipid interactions in bilayer membranes: married couples and casual liaisons. *Prog. Lipid Res.* **51,** 179–98 (2012).
141. Simons, K. & Vaz, W. L. C. Model systems, lipid rafts, and cell membranes. *Annu. Rev. Biophys. Biomol. Struct.* **33,** 269–95 (2004).
142. Wong, G. C. L. *et al.* Lamellar Phase of Stacked Two-Dimensional Rafts of Actin Filaments. *Phys. Rev. Lett.* **91,** 1–4 (2003).
143. Quinn, P. J. & Wolf, C. An X-ray diffraction study of model membrane raft structures. *FEBS J.* **277,** 4685–98 (2010).
144. Hirai, M., Iwase, H., Hayakawa, T., Koizumi, M. & Takahashi, H. Determination of asymmetric structure of ganglioside-DPPC mixed vesicle using SANS, SAXS, and DLS. *Biophys. J.* **85,** 1600–10 (2003).
145. Van Meer, G., Voelker, D. R. & Feigenson, G. W. Membrane lipids: where they are and how they behave. *Nat. Rev. Mol. Cell Biol.* **9,** 112–24 (2008).
146. Pan, J., Tristram-Nagle, S. & Nagle, J. Effect of cholesterol on structural and mechanical properties of membranes depends on lipid chain saturation. *Phys. Rev. E* **80,** 1–12 (2009).
147. Francescangeli, O., Pisani, M., Stanic, V., Bruni, P. & Weiss, T. M. Evidence of an inverted hexagonal phase in self-assembled phospholipid-DNA-metal complexes. *Europhys. Lett.* **67,** 669–675 (2004).
148. Weiss, T. M. *et al.* Dynamics of the Self-Assembly of Unilamellar Vesicles. *Langmuir* **038303,** 1–4 (2005).
149. Tristram-Nagle, S. *et al.* Polymorphism in myristoylpalmitoylphosphatidylcholine. *Chem. Phys. Lipids* **100,** 101–13 (1999).
150. Danner, S., Pabst, G., Lohner, K. & Hickel, A. Structure and Thermotropic Behavior of the Staphylococcus aureus Lipid Lysyl-Dipalmitoylphosphatidylglycerol. *Biophys. J.* **94,** 2150–2159 (2008).
151. Heberle, F. a *et al.* Bilayer thickness mismatch controls domain size in model membranes. *J. Am. Chem. Soc.* **135,** 6853–9 (2013).
152. Pencer, J. *et al.* Detection of submicron-sized raft-like domains in membranes by small-angle neutron scattering. *Eur. Phys. J. E. Soft Matter* **18,** 447–58 (2005).
153. Davis, R. S., Sunil Kumar, P. B., Sperotto, M. M. & Laradji, M. Predictions of phase separation in three-component lipid membranes by the MARTINI force field. *J. Phys. Chem. B* **117,** 4072–80 (2013).
154. Liang, H., Harries, D. & Wong, G. C. L. Polymorphism of DNA-anionic liposome complexes reveals hierarchy of ion-mediated interactions. *Proc. Natl. Acad. Sci. U. S. A.* **102,** 11173–8 (2005).
155. Fraser, R. D. B., MacRae, T. P. & Suzuki, E. An improved method for calculating the contribution of solvent to the X-ray diffraction pattern of biological molecules. *J. Appl. Crystallogr.* **11,** 693–694 (1978).

156. Svergun, D., Barberato, C. & Koch, M. H. J. CRYSOL – a Program to Evaluate X-ray Solution Scattering of Biological Macromolecules from Atomic Coordinates. *J. Appl. Crystallogr.* **28,** 768–773 (1995).
157. Di Gregorio, G. M. & Mariani, P. Rigidity and spontaneous curvature of lipidic monolayers in the presence of trehalose: a measurement in the DOPE inverted hexagonal phase. *Eur. Biophys. J.* **34,** 67–81 (2005).
158. Garvey, C. J., Lenné, T., Koster, K. L., Kent, B. & Bryant, G. Phospholipid Membrane Protection by Sugar Molecules during Dehydration-Insights into Molecular Mechanisms Using Scattering Techniques. *Int. J. Mol. Sci.* **14,** 8148–63 (2013).
159. Lenné, T., Garvey, C. J., Koster, K. L. & Bryant, G. Effects of sugars on lipid bilayers during dehydration--SAXS/WAXS measurements and quantitative model. *J. Phys. Chem. B* **113,** 2486–91 (2009).
160. Demé, B. & Zemb, T. Hydration forces between bilayers in the presence of dissolved or surface-linked sugars. *Curr. Opin. Colloid Interface Sci.* **16,** 584–591 (2011).
161. Svergun, D. I. *et al.* A small angle x-ray scattering study of the droplet–cylinder transition in oil-rich sodium bis(2-ethylhexyl) sulfosuccinate microemulsions. *J. Chem. Phys.* **113,** 1651 (2000).
162. Bernadó, P. & Svergun, D. I. Structural analysis of intrinsically disordered proteins by small-angle X-ray scattering. *Mol. Biosyst.* **8,** 151–67 (2012).
163. Lawson, C. L. & Hanson, R. J. *Solving least squares problems*. *SIAM Class. Appl. Math.* **15,** 337 (1995).

APPENDICES

APPENDIX A: A SHORT MANUAL FOR XPODS SOFTWARE

Version: *UDV.1. (Under Development Version 1) (2013).*

An Overview

XPODS (X-ray analysis software for Partially Ordered and Disordered Systems) is a software written to provide a tool for the analysis of x-ray scattering data of partially ordered and disordered systems. In particular, those of biological origin. Currently works only for Mar detectors.

For decades single crystal diffraction has been (and still) the major tool for understanding the structure of biological molecules. NMR and cryo-electron microscopy have also played significant roles in understanding the structure of biological molecules in disordered forms. Each of those techniques has its strengths and weaknesses. More recently, Small and wide angle scattering (SAXS and WAXS) has been widely used in extracting structural information about biological molecules such as lipids and proteins at low resolution. SAXS and WAXS experiments tend to be simple experiments with minimal sample preparation requirement. This flexibility in the sample conditions allows one to be able to probe biological molecules in a more biologically relevant environment. By biologically relevant, we mean closer to its natural cellular environment. This opens the door to opportunities to examine simple complexes of biological molecules simulating cellular systems and machineries. Possible examples of such systems are lipid-DNA, lipid-protein and protein-protein assemblies. Such complexes can represent very simplified versions of some organelles (e.g. nucleus, membrane proteins in the cell, etc.). Further, understanding the average structure of these partially ordered systems such as liquid crystalline materials and completely disordered systems such as proteins in solution can have an important role in the understanding of the dynamics of such molecules in different environments.

The difficulty however in such systems is the loss of the signal, partially due to the cancellation of scattered waves and due to the weakness of the scattering contrast of biomolecules, especially at higher resolution. On the other hand, these techniques generally provide a ‘signature’ containing the structural information represented in a 1D curve. One possible way to maximize our interpretation of the information obtained from the scattering patterns is to utilize extensive computational techniques, predictions, simulations and theoretical methods (thermodynamics and statistical mechanics). This can be very powerful when combined with measurements of the same specimen in multiple conditions. The assembly of information from one or more of these methods with the scattering data can indeed boost the interpretation of the data and provide a more in-depth interpretation for the 'experimental hints' encoded in the scattering pattern.

Automation

One of the main targets of this pipeline/software is to provide a fully automated tool for SAXS/WAXS analysis. Automation was achieved by attempting to make input parameters to be highly flexible as well as setting defaults that can be generally used for every command. As the software develops, we will attempt to utilize concepts and techniques applied in crystallography and powder diffraction when needed. Unless mentioned otherwise, the program by default will process all images in a folder considering them as a series, i.e. multiple scans or measurements of the same sample.

Installation

The pipeline depends on some basic python libraries: *Numpy*, *SciPy*, *Matplotlib* and *PIL* (*Python Image Library*). Once those are installed, an alias to the main module (e.g. python /path/XPODS.py) can be set to a shell/bash command. We chose and will refer to this command as **xpods**.

General Usage

The general use of the software is by typing in the terminal:

xpods ***command*** [*option*] *filename*

- ***command*** is one of the commands : *lipidwaxs (or waxslipid)*, *powder* or *qcalc*. Each command initiates a workflow for processing a specific type of data (see pipelines/workflow description section for more details).
- *options* are either *-single* or *-series*. If neither is given, then all tiff images in the folder will be processed as multiple scan or run of the same sample (i.e. Assuming they contain the same information).
- *filename* is either the single image file or one images of the series to be processed. If no option is given *(-single* or *-series*), this will be ignored. This parameter is a must in case of a series. If not given in case of single, then all files in the folder will be processed independently.

Getting started

In principle, no parameter file is needed if the image header is set correctly and if no specific processing features are of interest. Further, ssrl *prp* files can be also used as an alternative. If neither is available, then a parameter file having the experimental setup parameters (*param.in*) is needed to be in the same folder. A template parameter file is distributed with the source code and available in */template/param.in*.

- An examples of processing SAXS/WAXS data from a liquid crystalline sample (e.g. lipids) would be:

  xpods *lipidwaxs*
- An examples of processing powder diffraction data from a crystalline sample would be:

  xpods *powder*

Unless otherwise specified, the program by default will process all images in a folder considering them as a series, i.e. multiple runs/measurements of the same sample.

- An examples of processing a single image (and ignoring other images in the folder) SAXS/WAXS data from a liquid crystalline sample would be:

xpods ***lipidwaxs*** *-single image_name.tiff.*

Options

Current options are:

- *-single*: If option ’single’ is given followed by an image file name, this single image will be processed independently, other images in the folder will be ignored.
- *-series*: If option ’series’ is given followed by any image file name, all images holding this similar base name will be processed as multiple images from the same sample.

Input parameters

The input parameter file param.in can take the following parameters:

Parameter (= value)	**Description**
memory_size = x, y	Memory size for *fit2d* (minimum values should be equivalent to the x, y dimensions of detector that will be processed). Defaults values are 6000, 6000.
energy = value	Energy of incident beam.
beam_size = x, y	Beam size in microns.
beam_divergence = x, y	Beam divergence in horizontal and vertical direction.
deterctor_size = x, y	Detector size (no. of pixels in horizontal and vertical directions).
pixel_size = x, y	Pixel size in microns.
detector-sample_distance = value	Sample to Detector distance.
beamstop-sample_distance = value	Sample to beamstop distance.
beamstop_size = x, y	Size of beamstop in microns.
I0 = value	Initial intensity of beam (upstream the sample).
I1 = value	Intensity of beam after going through sample

	(downstream the sample).
beam_centre = x, y	Beamcentre pixel.
detector_dimentions= x, y	Detector dimensions in mm.
mask_type = Type *Type* of mask to be applied at beamstop position, where 'type' is one of:	
- 'regular'	Will attempt to mask a regular area around beamcentre (square or rectangular).
Or - 'regular_circular'	Will attempt to mask a circular shaped area around beamcentre.
Or - 'search'	Irregular mask depending on pixel intensity. Will search for pixels that are below the threshold value or that are below 'maskIsig' times more than the beam center pixel intensity. In other word, pixels that are around the beamcenter with a signal/noise below the value of ‘maskIsig’ will be masked. The signal/noise is considered to be $= \frac{\mathit{current\ pixel\ intensity}}{\text{beamcentre pixel intensity}}$.
Or - 'DIL'	Will attempt to use the auto-masking function provided by Diffraction Image Library if CCP4 is installed. This works OK for proper MAR images only and tends to be suitable for images from systems of high periodicity such as such as those obtained from crystallography or powder diffraction. If fails the program will stop.

	Beamstop holder search will then be performed using a general algorithm (despite the mask type) and will be masked.
mask_threshold = value	Pixels below this threshold value will be masked.
integrate = type	Integrate either using the integrate module 'integrate', or using *fit2d* program 'fit2d'. Default is currently 'fit2d'.
plot_format = format	Format of plots by extension. Default is encapsulated postscript '.eps'.
protein_concentrations= list1: list2	*list1: list2* is: List of folders (separated by commas): List of concentrations (separated by commas). If blank is given, then it has to be the first in order named 'blank' and its corresponding concentration must be set to '0.0'.
powder_conditions = list1: list2 Or *powder_projects = list1: list2*	*list1: list2* is: List of folders (separated by commas): List of numbers (separated by commas). List of projects numbers/conditions (separated by commas): list of numbers (separated by commas).
background_file = file_name Or *blank_file = file_name*	Name of blank image (e.g. buffer in holder). If found in the folder, will be subtracted.

Input files

1. Image files

Only files with *img*, *tiff* or *tif* extensions will be processed. Image files must be in the working directory or in one of the given directories in the *param.in* file in case of multiple concentrations or multiple projects.

2. The Parameters file *param.in*

A simple text input parameter file named *param.in*. If found in the working main directory, will be read automatically. The following is an example *param.in* file.

Parameters file

All parameters must start after '[Input parameters]' and end before 'end'. Any line starts with '#' or '!' is a comment. Any lines before '[Input parameters]' are comments. Any parameter that have multiple attributes are separated by commas and comes in the order stated (for example: x, y). Parameters before the hash line are mandatory for qcalc. Beamstop size is either given as an input or put as None, None. 'beamstop_size' is the diameter.

```
[Input parameters]

#       detector_dimentions = 300, 300
#       energy (keV)= 8
#       beam_size (microns) = 50, 50
#       beam_divergence (mrad) = 0.9, 0.2
#       detector-sample_distance(mm) = 1000
#       beamstop-sample_distance (mm) = 950
#       protein_concentrations = conc1, conc2, conc2.5, conc3, conc4, conc5, conc7.5, conc8 : 0.96,  1.92,  2.4 ,  2.88,  3.84,  4.8 ,  7.2 ,  7.68
#       memory_size = 6000, 6000
#       beamstop_size(microns) = None, None
#       deterctor_size(pixels) = 4096,  4096
#       beam_centre = 2000,  2047
#       pixel_size(microns) = 0.0732, 0.0732
#       chemical_formula = Cx ,Ox ,Hx ,Znx
#       I0 = 0
#       I1 = 0
#       twoTheta (degree) = 0   #  (Range:  1.000000E-03  to  10000.00)  defaults  are  8.000000E-03  for  powder diffraction and 2.000000E-03 for protein SAXS.
#       twoTheta_steps = 8.000000E-03
#       some_comments
;       some_comments
end
Any line added after 'end' is a comment.
```

3. The SSRL parameter file SSRL *.prp*

An input parameter file in the format used by the BL2-4 beamline at SSRL (see parameters below). The file is used to record the image parameters instead of the image header. The parameters definitions are as follows:

Parameter = example value	Definition
Image file name: sample.tif	Image file name
I_Signal (i.e. I1 in header file) is from: i_apd	Not used in our case
I_signal=2953827.0 (corrected for dark counts)	Signal from the apd, i.e. proportional to integrated incoming intensity
I_0(1.0)=-0.2229	Seemingly not used, usually upstream ion chamber
I_1(1.1)=-0.0216	Not used in our case
I_2(1.2)=213095.0 (corrected for dark counts)	Photodiode in beamstop, i.e. proportional to integrated transmitted intensity
I_diff(1.3)=0.5345	Not used
t_sample(1.4)=0.0002	Not used
I_apd(2.0)=2953827.0	apd intensity, in our case the same as I_signal
I_upstream(2.4)=0.0001	Upstream vacuum reading
I_downstream(2.5)=-0.0008	Downstream vacuum reading
Detector mode=0; 0 for normal and 1 for dezingered	Detector using normal data colection mode
Exposure time=3	Nominal exposure time (not exact!)
Counting time=4.0	Time scalars are counted (should be longer than exposure time)
Beam energy=10000.003089 eV	Beam energy
Pipe length=1700 mm	Nominal detector distance (not exact, will need calibration.)
Scan motor=NULL	Not used in our case
Scan range=0 mm	Not used in our case
Phi position=0.300000	Not used in our case
Horizontal position=74.533333 mm	Sample stage position horizontal
Vertical position=4.516544 mm	Sample stage vertical
dispx position=57.300143 mm	Not used in our case
dispy position=30.502576 mm	Not used in our case

Output files

The program will create a directory containing all results and output files. The output files for each pipeline is as follows:

1. **The *lipidwaxs* and *powder* pipeline**

all_parameters.log	A log file containing all parameters read from every image, including image header, SSRL *.prp* file and final parameters used in processing.
fit2d.log	A log file containing all *fit2d* printed info.
image_name.chi	Are raw processed *ascii* files produced by *fit2d*.
I_versus_TwoTheta_ave_and_sum.eps	A plot of raw data having both the summed and averaged curves plotted.

Directories (folders):

- **averaged** : Contains all results from averaged curve.
- **summed** : Contains all results from summed curve.
- **mask** : Contains all files related to masking of images.
- **comparisons** :Contains all comparison plots, if multiple projects/samples/concentrations are processed simultaneously. This folder will be found in the *last* sample processed. Samples are processed in the same order that is found in the parameter file.

/averaged (and /**summed)**

Files names	**Description**
summed_data_twoTheta.dat ***(averaged_data_twoTheta.dat)*** ***summed_data_d.dat*** ***(averaged_data_d.dat)*** ***summed_data_q.dat*** ***(averaged_data_q.dat)***	Ascii data file having radially averaged intensities versus 2θ, q and d for summed and averaged images.
I_versus_TwoTheta_summed.eps ***(I_versus_TwoTheta_averaged.eps)*** ***I_versus_q_summed.eps*** ***(I_versus_q_averaged.eps)*** ***I_versus_d_summed.eps*** ***(I_versus_d_averaged.eps)***	Plots of radially averaged intensities versus 2θ, q, d for summed and averaged images. These plots are generated from the above data files.
summed_data_twoTheta_fitted_bk.eps ***(averaged_data_twoTheta_fitted_bk.eps)***	Plots of intensities versus 2θ along with fitted background.
summed_data_subtracted.dat ***(averaged_data_subtracted.dat)***	Ascii data file of intensities and 2θ after fitted background is subtracted.

summed_data_twoTheta_subtracted.eps ***(averaged_data_twoTheta_subtracted.eps)***	Plots of intensities versus 2θ after fitted background is subtracted.
summed_data_subtracted_fitted_peaks.eps ***(averaged_data_subtracted_fitted_peaks.eps)***	Plots of intensities versus 2θ of fitted peaks after background is subtracted.
summed_peaks.dat ***(averaged_peaks.dat)*** ***summed_peaks.eps*** ***(averaged_peaks.eps)*** ***summed_peaks_relInts.eps*** ***(averaged_peaks_relInts.eps)***	Peak data (.*dat* files) and bar plots of peak positions and intensities. The intensities are either raw intensities or relative intensities (*_relInts.eps).
summed_subtracted_peaks.dat ***(averaged_subtracted_peaks.dat)*** ***summed_subtracted_peaks.eps*** ***(averaged_subtracted_peaks.eps)*** ***summed_subtracted_peaks_relInts.eps*** ***(averaged_subtracted_peaks_relInts.eps)***	Similar to the above, but after the diffuse background fitting and removal. Used in *powder* command.
summed_final_peaks.dat ***(averaged_ final_peaks.dat)*** ***summed_final_peaks.eps*** ***(averaged_final_peaks.eps)***	Peak data (.*dat* files) and bar plots of peak *after fitting to profiles* positions and intensities. The intensities are either raw intensities or relative intensities (*_relInts.eps).

/mask (beamstop masks)

fit2dmask.tiff	A mask file suitable for use for in *fit2d*.
mask.tiff	A regular mask file.
imageXname_m.tiff	A Mask used for a specific file.
mask_for_display.tiff	A mask file used for easy visualization.

XPODS Modules

The software is composed of:

1- A main module: that will read parameters, options and files, and will then redirect the pipeline to the specific processing module pending on the given command.

2- A set of higher level modules that will attempt to use the basic modules to fully automate a specific workflow (a series of analysis steps).

3- A set of basic modules that will perform basic processing tasks

The roles/functions of the individual modules are as follows:

Module Name	Module Type	Function
XPODS	Main module	Controls all other modules. According to the input command, this module will call one of *autofit2d* and/or *integrate* module to process the images, and then will call one of *powder or waxslipid* modules for commands '**powder**' or '**waxslipid**' respectively, to do further analysis on the 1D curves.

pwd_waxs	Higher level module	Performs automated processing of 1D curves for powder data (i.e. curves containing Bragg's peaks).
qcalc	Higher level module	Contains functions that calculates expected minimum and maximum *q* and *d* at different sample-detector distances, energies and beam-sizes.
autofit	Basic module	Performs all fitting procedures.
autofit2d	Basic module	Performs data reduction using *fit2d* program, produces normalized intensities (i.e. radially averaged; equivalent to CONSERVE INT= NO option in *fit2d*).
autopeaks	Basic module	Performs all peaks search and analysis.
config	Configuration script	Sets paths for external dependencies.
diffImgLib	Basic module	An interface to Diffraction Image Library (part of CCP4 library DIL), was used to read the image headers and now replaced by a Fortran program. Future implementations will completely replace this module by an alternative that will use CBFlib.
imgRead	Basic module	Reads and writes images. Future implementation will implement dealing with CBF and imgCIF files.
integrate	Basic module	Performs all masking and integration processes.
param_reader	Basic module	Reads, regulates and exports input parameters from image headers, SSRL prp files (*.prp*), parameter input file (*param.in*) and sets defaults parameters.
plot	Basic module	Creates all plots.
read_ascii	Basic module	Reads and writes data files.
slope	Basic module	Contains a variety of helper functions.
global_params	Basic module	Performs comparisons in case of multiple projects or concentrations processed simultaneously.
transform	Basic module	Performs all operations on 1D curves. This includes: • *s*, *d*, *q* and *2θ* scale transformations,

		where, $q = \frac{4\pi\sin(\theta)}{\lambda}$ and $d = {2\pi}/{q} = \frac{\lambda}{2\sin(\theta)} = {1}/{s}$ • Normalizations (flux, time, etc.) and corrections (polarization, Lorentz, absorption, etc.). • Simple mathematical operations and line extrapolation. Statistical measures such as smoothness, Chi Squared, etc.
validate	Basic module	• Performs various validation tests (currently not implemented in the pipelines).

Pipelines/workflow and command description

XPODS accepts the one of the commands below. Each command will initiate and go through a series of steps to process the data (a workflow):

A. *waxslipid or lipidwaxs*

Will process images assuming it is WAXS data for a partially oriented sample such as lipids (or liquid crystalline material in general). The expected pattern is from a generally partially ordered material i.e. containing both rings (Bragg's peaks) and diffuse scattering. The main features of the workflow is as flows:

- Analyses of 1D curves having Bragg’s peaks. By default both average and sum of curves will be calculated.

- If several images are processed as series, every curve will go through the following processes:
  - Normalization of the curve for flux (if given), time, and then scale by an arbitrary constant.
  - Correction for absorption, polarization and Lorentz.

- Then after obtaining the averaged and summed data (or single curve if only one image if processed), the module will:
  - Subtract background (if given).
  - Search for peaks and then estimate initial parameters for fitting to profiles.
  - Peaks are fitted into specified peak-profiles (e.g. Gaussians, etc.)
  - The final peaks are ones were successfully fitted to the profile function.
  - Integrate the found peaks, the formula used is as follows:

$$\boldsymbol{Integral} = \sum_{k=b1}^{k=b2} \boldsymbol{I_k(x)}.\Delta\boldsymbol{x}$$

Where,

$\boldsymbol{x} = \boldsymbol{2\theta}$ or $\boldsymbol{q}$ or $\boldsymbol{d}$

$\boldsymbol{k}$ is the number of points.

$\boldsymbol{b1}$ & $\boldsymbol{b2}$ are the beginning and end of the peak profile function.

- The relative intensity and relative peak position for every peak is found.
- The final peak profiles are written out in to a file.
- A plot will be generated at almost every step to allow visual confirmation if needed.

➢ It should be noted that:

- Non-essential steps such flux normalization and absorption correction will be skipped if flux upstream and downstream the sample are not available.
- If a background image is given, it will be subtracted from the curves after averaging and summing the curves.
- Data is written out in standard *ascii* format (see output files for details).

B. powder

Will process images assuming it is powder data, where the sample is considered to be ordered, producing linear anisotropic scattering (diffraction rings). Generally speaking, both *waxslipid* and *powder* commands utilize the same module for the analysis. In these initial versions of the software, both will go through similar analysis steps. The only difference is that in the case of *powder*, the background will be fitted into a function (e.g. polynomial) and will be subtracted (if a background is not given). Then it will make another round of peak determination, profile fitting, and integration, this time on the subtracted curve. The main reason for having both commands is for future development purposes. It is planned that future versions will enable further distinctions, for example options as automatic phase determination and indexing shall be added.

C. qcalc

A simple small tool intended for the preparation of the SAXS/WAXS synchrotron experiments. By using the same usual input parameter file of the program, one could calculate expected minimum and maximum q and d at different sample-detector distances, energies and beam-sizes.

APPENDIX B: SUMMARY GRAPHS OF SCATTERING PATTERNS

12-3-12 DNA complexes summary graphs

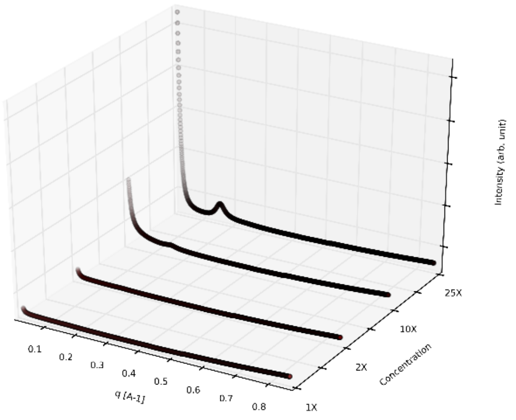

5:1

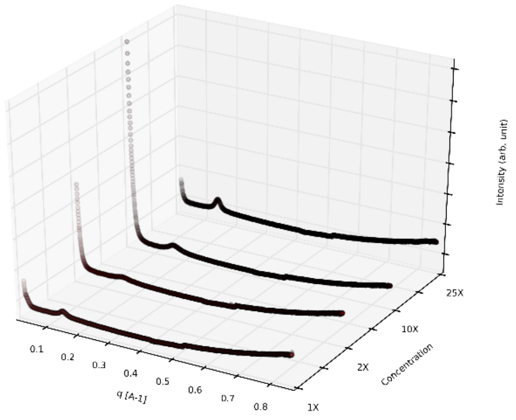

1:10

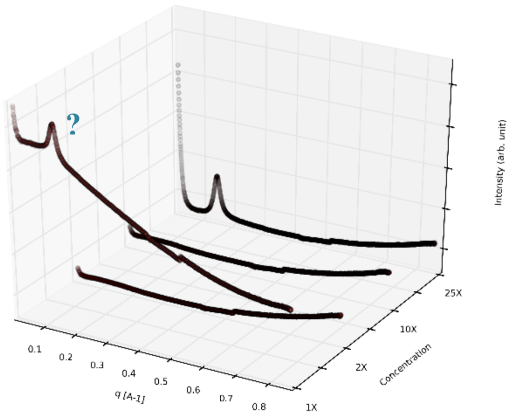

1:1

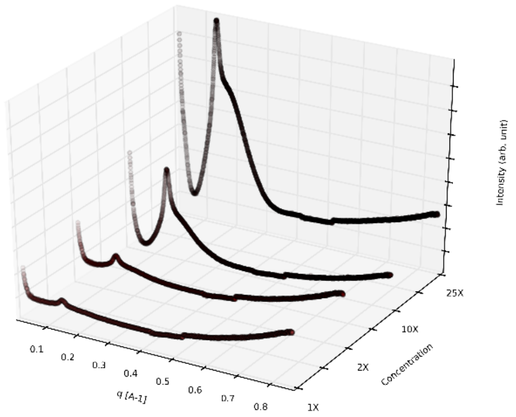

1:20

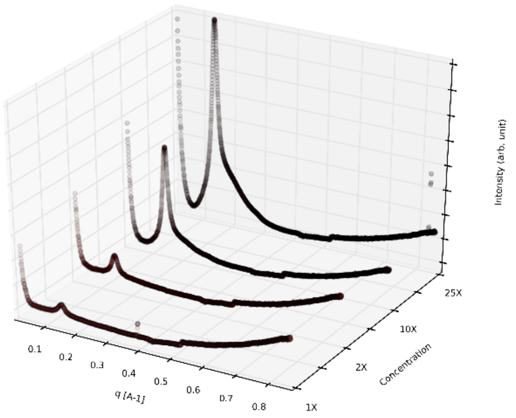

1:5

12-3-12 DNA summary graphs at different charge ratios.

12-3-12 DNA DPPC summary graphs

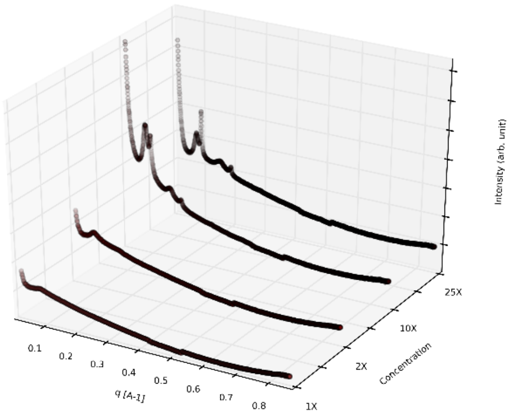

5:1

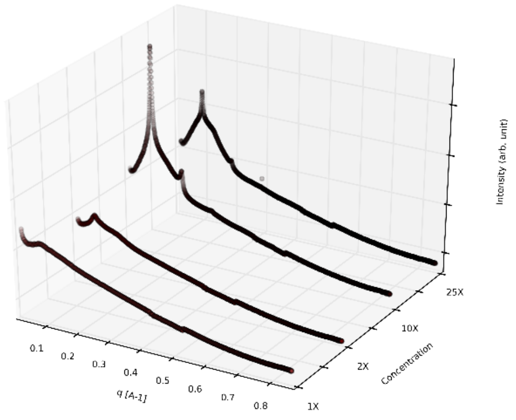

1:10

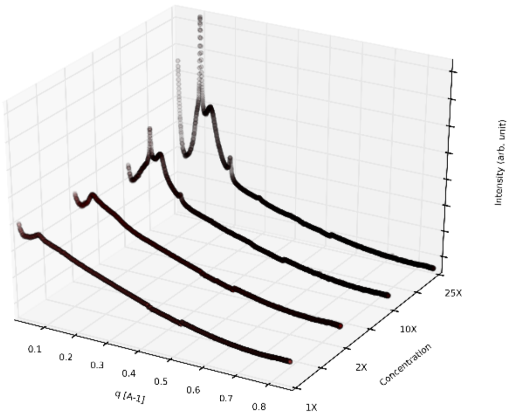

1:1

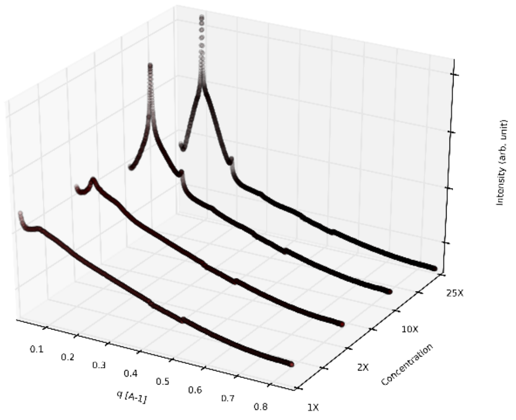

1:20

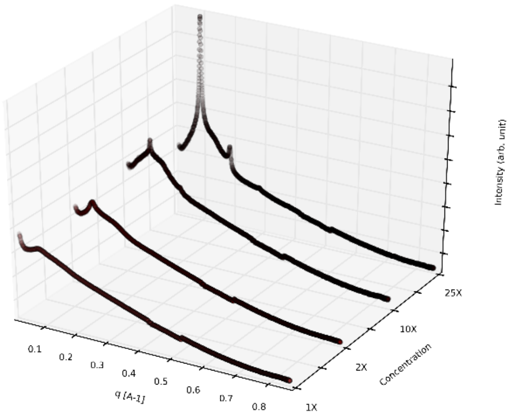

1:5

12-3-12 DNA DPPC summary graphs at different charge ratios.

12-3-12 DNA DPPC-DOPE summary graphs

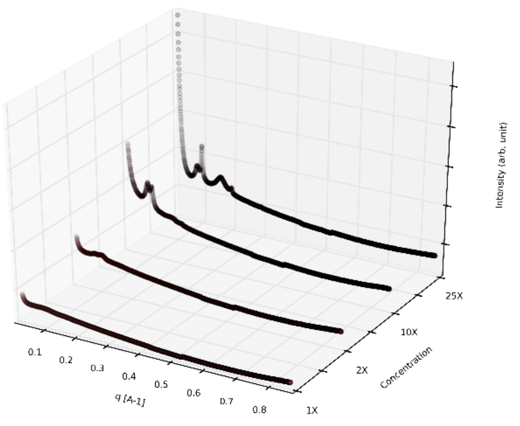

5:1

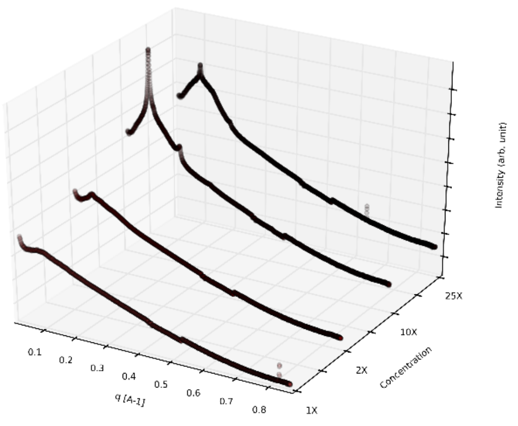

1:10

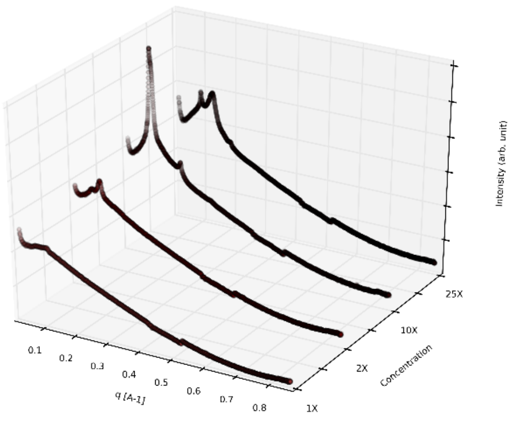

1:1

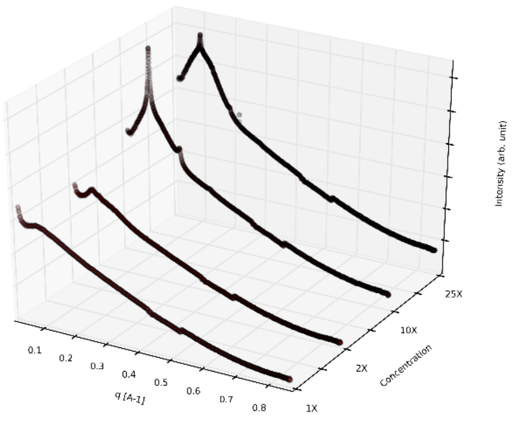

1:20

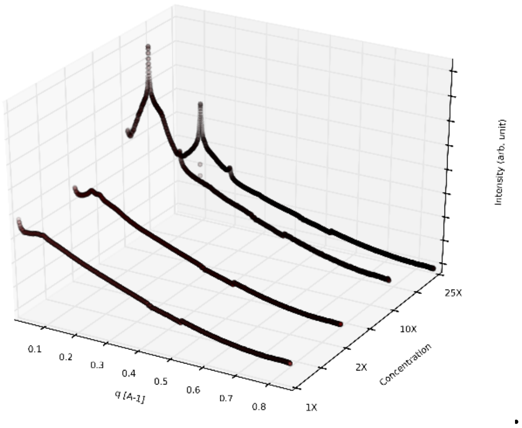

1:5

12-3-12 DNA DPPC-DOPE summary graphs at different charge ratios.

12-3-12 DNA DOPE summary graphs

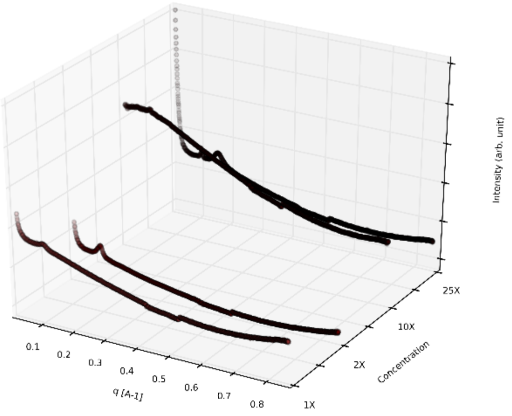

5:1

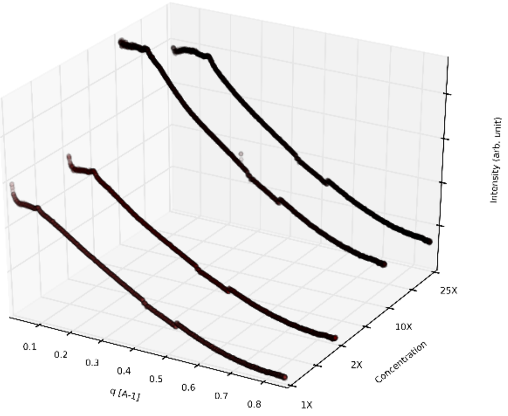

1:10

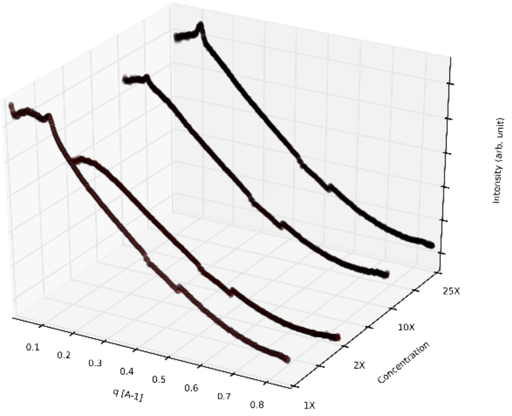

1:1

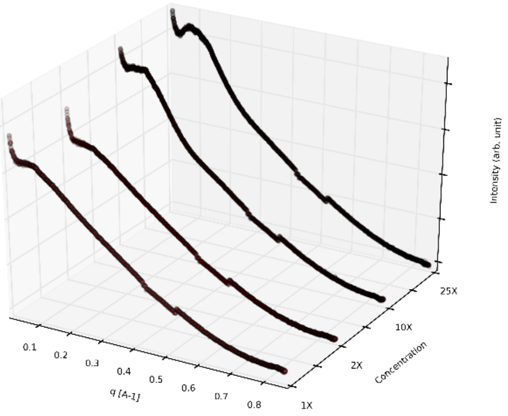

1:20

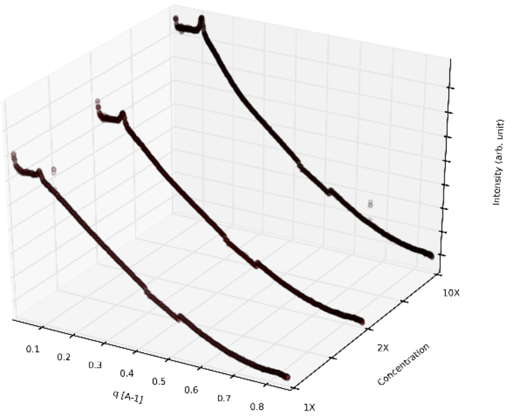

1:5

12-3-12 DNA DOPE summary graphs at different charge ratios.

16-3-16 DNA DOPE summary graphs

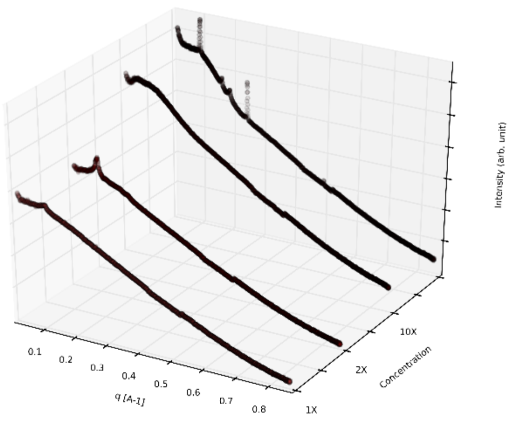

1:10

16-3-16 DNA DOPE summary graphs at different charge ratios.

Contributions Statement

This contributions statement is regarding the work presented in this thesis, and intended as a reference for future publication or scholarly use.

Instrumental section

The scattering chambers made is a property of CLS. If this section of the work is re-published elsewhere, authorship is determined Pawel Grochulski.

Contributions: Osama Alaidi, James Gorins and Pawel Grochulski* designed and made the chambers.

Software section

The software is a property of its author; Osama Alaidi. If re-published elsewhere, authorship is may include Osama Alaidi*, Pawel Grochulski, Ildiko Badea and Masoomeh Poorghorban. A copy for local use can be available upon request.

Contributions: Osama Alaidi has written the software.

X-ray section

Osama Alaidi can continue working on the raw x-ray data until completion.

Contributions: Osama Alaidi* designed and prepared samples for the scattering experiments and analysed the data. Pawel Grochulski, Ildiko Badea collected data at SSRL, McDonald Donkuru synthesized the gemini. All of Osama Alaidi, Ildiko Badea, Pawel Grochulski and Mariana Foldvari have contributed to the general design of the formulations.

*To whom correspondence will be addressed.